Development of High-Resolution Two-Dimensional Correlation Spectroscopy in Solid-State NMR: Applications to Nanocomposites and Fullerides

Daniel F. Lee, MSci.

Thesis submitted to the University of Nottingham for the degree of

Doctor of Philosophy

December 2010

Abstract

Two-dimensional correlation spectroscopy in solid-state NMR is an immensely important tool for the analysis of materials, such as technologically interesting nano-materials or bio-materials. After detailing one method that returns high-resolution one-dimensional solid-state proton NMR spectra, high-resolution proton-proton two-dimensional correlation experiments are described and demonstrated. Subsequently, a new two-dimensional NMR experiment is described which is suitable for obtaining a high-resolution proton dimension in heteronuclear dipolar correlation spectra of solids. This new experiment has been used to characterise the interface between the organic and inorganic components of "core-shell" colloidal nanocomposite particles. In addition, a new two-dimensional NMR experiment is described which is suitable for obtaining homonuclear scalar correlation spectra in solids. This new experiment has several advantages, including increased cross peak intensities coupled with good suppression of the diagonal. Its utility is demonstrated via carbon-13 spectra of natural abundance samples as well as the polymer phase of caesium fulleride.

Acknowledgements

"...we may face the future with confidence because we fill the gaps of our knowledge not with religious dreams or philosophical speculations but with scientific facts..."
Henry E. Sigerist (1943).

My first and foremost acknowledgement must go to Dr. Jeremy Titman, my supervisor and mentor. Many an hour was spent under his patience and equanimity during a multitude of questions. For that, amongst innumerable other factors, I would like to note my huge appreciation.

Dr. Andy Jurd must also receive a special mention. He was ever-present for almost the entirety of my postgraduate studies and my working knowledge of simulations, pulse programming and also the mechanical aspects of NMR equipment are attributable to his aid.

The members of the University of Nottingham solid-state NMR group, past and present, have been a source for debate and also entertainment and many thanks are owed with respect to my enjoyment of my postgraduate studies. These members are: Dr. Limin "Maggie" Shao, Dr. Andrew Powell, Dr. Yanqi Wu, David Bennett, Greg Martin and the undergraduates John Godfrey and Angelica Gopal.

I would also like to acknowledge the following for being pleasant prohibitors to the completion of this work: Chloe Hodgkinson, Andy Hughes, Lynn Kozak, Mark Wilson, Charlie Veal, all of the Thai Boxers from Master Lec's Singnakornchai and University Camps and all of the members of any (of the plenty) of the sports teams that I have played for during these past four years.

Finally, I would like to thank the EPSRC (grant no. EP/P502632/1) for the funding to make this thesis possible.

This thesis is dedicated to my parents; Lynn and Malcolm. Their love and support throughout my many, many years of education has certainly not gone unnoticed nor been undervalued.

Contents

List of Figures

List of Tables

Table of Abbreviations

COSY	COrrelation SpectroscopY
CP	Cross Polarization
CRAMPS	Combined Rotation and Multiple Pulse Spectroscopy
CTP	Coherence Transfer Pathway
CW	Continuous Wave
DCP	Disk Centrifuge Photosedimentometry
DLS	Dynamic Light Scattering
DSC	Differential Scanning Calorimetry
DQ	Double Quantum
DQF	Double Quantum Filter
DUMBO	Decoupling Using Mind-Boggling Optimisation
FID	Free Induction Decay
FT	Fourier Transform
LG-CP	Lee-Goldberg Cross Polarization
MAS	Magic Angle Spinning
PAS	Principle Axis System
P2VP	Poly(2-Vinyl Pyridine)
P4VP	Poly(4-Vinyl Pyridine)
PS	Polystyrene
pBuA	Poly(Butyl Acrylate)
RF	Radio Frequency
SAR-COSY	Sensitive Absorptive Refocused COSY
SQ	Single Quantum
TBS	Tert-ButyldimethylSiloxy
TDSE	Time-Dependent Schrödinger Equation
TEM	Transmission Electron Microscopy
TPPI	Time-Proportional Phase Incrementation
TPPM	Two Pulse Phase Modulated Decoupling
XPS	X-ray Photoelectron Spectroscopy
ZF	Z-Filter

1 Introduction

In a little over fifty years, the field of Nuclear Magnetic Resonance (NMR) has expanded rapidly. So far, thirteen scientists who have aided in the development of NMR have been presented with Nobel Prizes. Nine of these scientists were awarded in the category of Physics (1944, 1952, 1966, 1977, 1981, 1987, 1989), two were awarded in Chemistry (1991, 2002) and, most recently, two were awarded in Physiology or Medicine (2003).

From a physical phenomenon, through chemical and materials applications, NMR has now also become one of the most important clinical imaging devices. It has also become the most significant conformational analysis tool for biological macromolecules in solution. Kurt Wüthrich received the 2002 Nobel Prize in Chemistry for his development of this aspect of NMR spectroscopy. However, after the award of the 1991 Nobel Prize in Chemistry to Richard R. Ernst "for his contributions to the development of the methodology of high resolution nuclear magnetic resonance (NMR) spectroscopy" it was not obvious that Wüthrich would also receive the prize for his contributions some years later. This shows the impact of high resolution NMR spectroscopy in chemistry.

Although conformational analysis of molecules in solution by NMR is an essential

tool in biochemistry and biophysics, conformational analysis of molecules in the solid state is less frequently employed. This is because NMR spectroscopy of molecules in the solid state is complicated by the anisotropy of the nuclear spin interactions of solids. A range of techniques have been developed to reduce and also to utilise these complications.

This thesis describes advancements in the methodology of solid-state NMR. In particular, these advancements are concerned with the acquisition of high-resolution correlation spectra of powdered, crystalline solids. The first chapter mainly outlines the basic principles behind solid-state NMR spectroscopy using a quantum mechanical description. Although it is not my intention to fully describe all of the techniques associated with solid-state NMR, in the latter part of Chapter 1 the techniques that are relevant to this thesis will be outlined. Ending this chapter is a brief discussion of the basic principles for coherent averaging methods of dipolar interactions including the development of homonuclear decoupling radio-frequency (RF) pulse schemes.

Chapter 2 follows on from this latter discussion with the introduction of a state-of-the-art homonuclear decoupling pulse sequence that is used throughout the majority of this thesis. This homonuclear decoupling sequence is shown to be useful for the acquisition of high-resolution one-dimensional solid-state proton spectra before being utilized as a tool in the acquisition of high-resolution two-

dimensional proton-proton correlation experiments. These two-dimensional experiments allow greater proton resolution to be obtained which, in turn, allows for a more detailed analysis of simple amino acids and nucleotides.

Chapter 3 advances the study on simple amino acids and nucleotides with the application of multinuclear experiments; more specifically a through-bond proton-carbon-13 correlation experiment. Secondly, Chapter 3 illustrates the shortcomings of this technique when applied to organic-inorganic nanocomposite particles and details a new, more appropriate two-dimensional through-space correlation experiment. This experiment, along with ubiquitous solid-state NMR experiments, is then applied to the study of these nanocomposite particles. In particular, the functionality of the new experiment is shown with an investigation of the surface interface between the inorganic and organic phases.

Chapter 4 moves away from multinuclear experiments and back to homonuclear experiments. A new two-dimensional NMR experiment is presented that is of particular use for obtaining through-bond correlation spectra in solids. More precisely, the utility of this new experiment is shown via carbon-13-carbon-13 through-bond correlation experiments and simulations on simple solid-state amino acids. In addition, the applicability of this experiment to natural abundance samples is demonstrated on an organic compound of medium complexity. This experiment is used to determine the electronic structure of an alkali fulleride

where two contrasting models are currently debated. Finally, chemical shift conditional probability distributions are given for two of the correlations from the experiment on the alkali fulleride to demonstrate the disorder of this sample.

The final chapter presents an outlook detailing the possibilities for future studies and also further work on the samples analysed herein.

1.1 The NMR Experiment

In a NMR experiment a sample is placed within a coil of conducting wire. Both are inside an external magnetic field. The external magnetic field creates magnetization within the sample that is parallel to the field. An applied current through the coil generates an oscillating radio frequency field. If this field is at the right frequency then the magnetization can be rotated into the plane perpendicular to the external magnetic field. This transverse magnetization vector precesses in this plane about the external magnetic field. Once the applied current is discontinued, the precessing magnetization induces an oscillating current in the coil. This current is the signal that the NMR spectrometer detects and records. Since the nature of the precession is determined by the environments of the nuclei within the sample then the NMR signal can be used to infer these environments.

1.2 Quantum Mechanical Approach to NMR

In quantum mechanics a *state vector* can be used to represent the physical state of a system. Quantum mechanics can then be used to determine the value of any physical observable by using the *operator* corresponding to the observable to act on the state vector. In Dirac notation

$$\hat{Q}|\psi\rangle = q|\psi\rangle \tag{1.2.1}$$

where $\hat{Q}$ is the operator, $|\psi\rangle$ is the state vector and in this case the *eigenfunction* of $\hat{Q}$ and q is the corresponding *eigenvalue*. The quantum numbers I and m describe the eigenfunctions of *nuclear spin angular momentum*.

$$\hat{I}_z|m\rangle = m|m\rangle \tag{1.2.2}$$

'Spin' (I) is an intrinsic property of subatomic particles (except for the currently hypothetical Higgs boson which would have a spin of zero). The spin of a given nucleus is dependent on the number of protons and neutrons within the nucleus. There are $2I + 1$ possible energy levels - or *eigenstates* - of spin I corresponding to eigenvalues

$$m = -I, -I + 1, \ldots I - 1, I \tag{1.2.3}$$

For a spin $I = 1/2$ nucleus m can take values $+1/2$ and $-1/2$. The eigenstates of a spin-1/2 nucleus are labelled $|\alpha\rangle$ and $|\beta\rangle$ such that

$$\hat{I}_z|\alpha\rangle = \frac{1}{2}|\alpha\rangle \qquad \hat{I}_z|\beta\rangle = -\frac{1}{2}|\beta\rangle \tag{1.2.4}$$

1.2.1 The Nuclear Spin Hamiltonian

The *Hamiltonian* for a nuclear spin can be represented as

$$\hat{\mathcal{H}} = \hat{\mathcal{H}}_Z + \hat{\mathcal{H}}_{RF} + \hat{\mathcal{H}}_{CS} + \hat{\mathcal{H}}_D + \hat{\mathcal{H}}_J + \hat{\mathcal{H}}_Q \tag{1.2.5}$$

where $\hat{\mathcal{H}}_Z$ is the Zeeman Hamiltonian term, $\hat{\mathcal{H}}_{RF}$ is the radio frequency Hamiltonian, $\hat{\mathcal{H}}_{CS}$ is the chemical shift Hamiltonian, $\hat{\mathcal{H}}_D$ is the dipole-dipole coupling Hamiltonian, $\hat{\mathcal{H}}_J$ is the J-coupling Hamiltonian and $\hat{\mathcal{H}}_Q$ is the quadrupolar coupling Hamiltonian.

1.2.2 The Zeeman Hamiltonian

NMR is based on the fundamental property that, when placed in a magnetic field, the degenerate nuclear spin eigenstates (energy levels) become non-degenerate. This is known as the *Zeeman interaction*. The size of the Zeeman interaction depends on the gyromagnetic ratio of the nuclear spin, γ_I, and the magnitude of

the magnetic field, $\mathbf{B}$. In a magnetic field, $\mathbf{B_0}$,

$$\hat{\mathcal{H}}_Z = -\gamma_I \hat{\mathbf{I}} \cdot \mathbf{B_0} = -\gamma_I \hat{I}_z B_0 = \omega_0 \hat{I}_z \tag{1.2.6}$$

where $\omega_0 = -\gamma_I B_0$ and is known as the *Larmor frequency* and where the component $\hat{I}_z$ of $\hat{\mathbf{I}}$ is defined to be parallel to the applied magnetic field, $\mathbf{B_0}$. $\hat{I}_x$ and $\hat{I}_y$ are two other components of $\hat{\mathbf{I}}$ that are both orthogonal to $\hat{I}_z$ and to each other.

1.2.3 The Radio Frequency Hamiltonian

In a NMR experiment the sample is placed within a coil of conducting wire. This coil can be used to generate an oscillating radio frequency (RF) field, $\mathbf{B_1}(t)$, with frequency ω_{RF} and phase ϕ_{RF}.

$$\mathbf{B_1}(t) = \begin{pmatrix} B_1 \cos(\omega_{RF} t + \phi_{RF}) \\ B_1 \sin(\omega_{RF} t + \phi_{RF}) \\ 0 \end{pmatrix} \tag{1.2.7}$$

The RF Hamiltonian can be written as

$$\begin{aligned} \hat{\mathcal{H}}_{RF}(t) &= -\gamma_I \hat{\mathbf{I}} \cdot \mathbf{B_1}(t) \\ &= -\gamma_I B_1 \cos(\omega_{RF} t + \phi_{RF}) \hat{I}_x - \gamma_I B_1 \sin(\omega_{RF} t + \phi_{RF}) \hat{I}_y \\ &= \omega_1 \cos(\omega_{RF} t + \phi_{RF}) \hat{I}_x + \omega_1 \sin(\omega_{RF} t + \phi_{RF}) \hat{I}_y \end{aligned} \tag{1.2.8}$$

where $\omega_1 = -\gamma_I B_1$. Magnetic resonance occurs when $\omega_{RF} \approx \omega_0$.

This RF Hamiltonian is time-dependent. A time-independent Hamiltonian is desired in order to simplify the maths. To achieve this a transformation to a rotating frame, rotating at ω_{RF} about the z-axis, is performed and this gives

$$\hat{\mathcal{H}}_{RF} = \omega_1(\hat{I}_x \cos\phi_{RF} + \hat{I}_y \sin\phi_{RF}) \tag{1.2.9}$$

1.2.4 The Chemical Shift Hamiltonian

An external magnetic field will induce electronic currents within a sample which in turn produces a magnetic field. Consequently, a nuclear spin in an external magnetic field will experience a local magnetic field, $\mathbf{B_{loc}}$, which is a combination of the external magnetic field and the magnetic field induced by the local electronic environment, $\mathbf{B_{induced}}$

$$\mathbf{B_{loc}} = \mathbf{B_0} + \mathbf{B_{induced}} \tag{1.2.10}$$

Since the magnetic field experienced by the nuclear spin depends upon the local electronic environment, the Zeeman energy, and thus the frequency of Larmor precession, is a good probe of local environment. The alteration of the Larmor

frequency from a reference frequency is known as the *chemical shift*, δ.

$$\delta = \frac{\omega_0 - \omega_0^{ref}}{\omega_0^{spec}} \tag{1.2.11}$$

where ω_0^{ref} is the reference frequency and ω_0^{spec} is the operating frequency of the spectrometer. Note that δ is given in field-independent units. For the reason that $\mathbf{B_{induced}}$ is of the order of 1×10^6 smaller than $\mathbf{B_0}$, the chemical shift is usually measured in parts per million (ppm).

The chemical shift Hamiltonian in the laboratory frame is

$$\hat{\mathcal{H}}_{CS} = -\gamma_I \hat{\mathbf{I}} \cdot \mathbf{B_{induced}} \tag{1.2.12}$$

and the induced magnetic field depends on the external field such that

$$\mathbf{B_{induced}} = \delta^{\mathbf{L}} \cdot \mathbf{B_0} = \begin{pmatrix} \delta_{xx}^L & \delta_{xy}^L & \delta_{xz}^L \\ \delta_{yx}^L & \delta_{yy}^L & \delta_{yz}^L \\ \delta_{zx}^L & \delta_{zy}^L & \delta_{zz}^L \end{pmatrix} \begin{pmatrix} 0 \\ 0 \\ B_0 \end{pmatrix} = \begin{pmatrix} \delta_{xz}^L B_0 \\ \delta_{yz}^L B_0 \\ \delta_{zz}^L B_0 \end{pmatrix} \tag{1.2.13}$$

so that

$$\hat{\mathcal{H}}_{CS} = -\gamma_I B_0 (\delta_{xz}^L \hat{I}_x + \delta_{yz}^L \hat{I}_y + \delta_{zz}^L \hat{I}_z) \tag{1.2.14}$$

where $\delta^{\mathbf{L}}$ is the *chemical shift anisotropy* (CSA) tensor in the laboratory frame and the element δ_{ij}^L measures the component of the field induced along i by an

external field along j. Since modern-day NMR spectrometers consist of large external magnetic fields the *secular approximation*[1] can be used. This means that terms which are not parallel to the z-axis can be ignored and the chemical shift Hamiltonian becomes

$$\hat{\mathcal{H}}_{CS} = -\gamma_I B_0 \delta^L_{zz} \hat{I}_z = \omega_0 \delta^L_{zz} \hat{I}_z \tag{1.2.15}$$

It can be seen from equation (1.2.15) that the chemical shift interaction is dependent on the external magnetic field. The induced perturbation to the Larmor frequency as a result of local environment, ω_{CS}, is then given as

$$\omega_{CS} = \omega_0 \delta^L_{zz} \tag{1.2.16}$$

The CSA tensor is diagonal in its *Principal Axis System* (PAS):

$$\delta^{\mathbf{L}} \rightarrow \delta^{\mathbf{PAS}} = \begin{pmatrix} \delta^{PAS}_{xx} & 0 & 0 \\ 0 & \delta^{PAS}_{yy} & 0 \\ 0 & 0 & \delta^{PAS}_{zz} \end{pmatrix} \tag{1.2.17}$$

where

$$|\delta^{PAS}_{zz} - \delta_{iso}| \geq |\delta^{PAS}_{xx} - \delta_{iso}| \geq |\delta^{PAS}_{yy} - \delta_{iso}| \tag{1.2.18}$$

[1]The secular approximation arises because large interactions with the external magnetic field dominate components that are perpendicular to this field.

and the *isotropic chemical shift*, δ_{iso}, is defined as

$$\delta_{iso} = \frac{1}{3}(\delta_{xx}^{PAS} + \delta_{yy}^{PAS} + \delta_{zz}^{PAS}) \tag{1.2.19}$$

The isotropic chemical shift is one of three parameters that can be used to describe the three *principal components* of the CSA tensor (δ_{xx}^{PAS}, δ_{yy}^{PAS} and δ_{zz}^{PAS}). The other two parameters are the anisotropy, ζ, and the asymmetry, η:

$$\begin{aligned} \zeta &= \delta_{zz}^{PAS} - \delta_{iso} \\ \eta &= \frac{\delta_{yy}^{PAS} - \delta_{xx}^{PAS}}{\delta_{zz}^{PAS} - \delta_{iso}} \end{aligned} \tag{1.2.20}$$

In the PAS of the CSA tensor the direction of $\mathbf{B_0}$ is given by

$$\mathbf{B_0}^{PAS} = (\sin\theta\cos\phi, \sin\theta\sin\phi, \cos\theta) \tag{1.2.21}$$

where θ and ϕ are defined in Figure 1.2.1. Using the PAS of the CSA tensor, ω_{CS} can then be described as a function of θ and ϕ as follows:

$$\omega_{CS}(\theta,\phi) = -\omega_0\delta_{iso} - \frac{1}{2}\omega_0\zeta[3\cos^2\theta - 1 + \eta\sin^2\theta\cos 2\phi] \tag{1.2.22}$$

The term $-\omega_0\delta_{iso}$ is the frequency of the isotropic chemical shift relative to the Larmor frequency. The term $-\frac{1}{2}\omega_0\zeta[3\cos^2\theta - 1 + \eta\sin^2\theta\cos 2\phi]$ describes the orientation dependence of ω_{CS}.

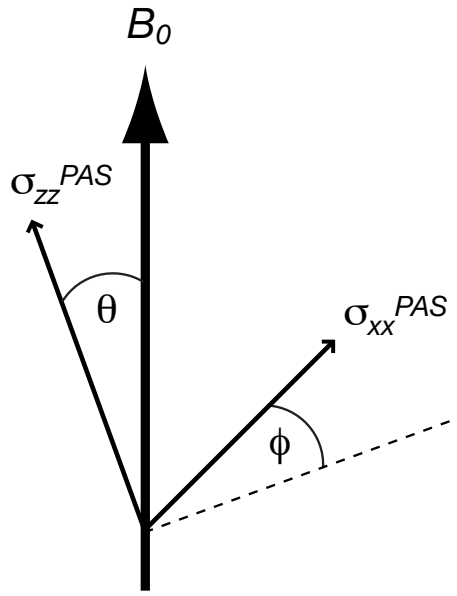

Figure 1.2.1: The definitions of the angles θ and ϕ, the polar angles defining the orientation of $\mathbf{B_0}$ in the PAS of the CSA tensor.

1.2.5 Dipole-Dipole Coupling

In high magnetic fields the non-secular part of the dipolar Hamiltonian may be discarded. The secular part of the dipolar Hamiltonian for two *homonuclear* spins ($\hat{I}_1$ and $\hat{I}_2$) is

$$\hat{\mathcal{H}}_D = \frac{1}{2}\frac{\mu_0\hbar\gamma_1\gamma_2}{4\pi r^3}(1 - 3cos^2\theta)(3\hat{I}_{1z}\hat{I}_{2z} - \hat{\mathbf{I}}_\mathbf{1}\cdot\hat{\mathbf{I}}_\mathbf{2}) \tag{1.2.23}$$

and the secular part of the dipolar Hamiltonian for two *heteronuclear* spins ($\hat{I}$ and $\hat{S}$) is

$$\hat{\mathcal{H}}_D = \frac{1}{2}\frac{\mu_0\hbar\gamma_I\gamma_S}{4\pi r^3}(1 - 3cos^2\theta)2\hat{I}_z\hat{S}_z \tag{1.2.24}$$

where r is the internuclear distance between the two spins and θ is the angle between the internuclear vector and the external magnetic field. The dependence on r and θ in both cases shows that dipolar couplings can provide information on molecular structure.

1.2.6 J-Coupling

An electron with non-zero probability of being at the nucleus (i.e. in a s-orbital) can interact with the nucleus by the Fermi contact hyperfine interaction. This provides an intermediary way through which nuclei can interact with one another; this interaction is usually referred to as spin-spin coupling or J-coupling. The form of the Hamiltonian for J-coupling is written

$$\hat{\mathcal{H}}_J = 2\pi \hat{\mathbf{I}}_\mathbf{1} \cdot \mathbf{J_{12}} \cdot \hat{\mathbf{I}}_\mathbf{2} \tag{1.2.25}$$

where $\mathbf{J_{12}}$ is the *J-coupling tensor* between spin one and spin two.

$$\mathbf{J_{12}} = \begin{pmatrix} J_{xx}^{12} & J_{xy}^{12} & J_{xz}^{12} \\ J_{yx}^{12} & J_{yy}^{12} & J_{yz}^{12} \\ J_{zx}^{12} & J_{zy}^{12} & J_{zz}^{12} \end{pmatrix} \tag{1.2.26}$$

In anisotropic liquids and solids the anisotropic part of the J-coupling is present.

However, this *J-anisotropy* has the same form as the dipole-dipole coupling but is much smaller in magnitude and is therefore usually ignored. The isotropic J-coupling (or *scalar coupling*) is equal to the average of the diagonal elements of the J-couling tensor

$$J_{12} = \frac{1}{3}(J_{xx}^{12} + J_{yy}^{12} + J_{zz}^{12}) \tag{1.2.27}$$

and so the scalar coupling Hamiltonian is given by

$$\hat{\mathcal{H}}_J^{iso} = 2\pi J_{12}\ \hat{\mathbf{I}}_\mathbf{1} \cdot \hat{\mathbf{I}}_\mathbf{2} \tag{1.2.28}$$

The work presented herein will assume a scalar coupling in solids; any J-anisotropy will be ignored.

1.2.7 Quadrupolar Coupling

Nuclei with spin $I > \frac{1}{2}$ exhibit quadrupolar coupling. This is an interaction between the nuclear quadrupole moment (which spin $I \leq \frac{1}{2}$ do not possess) and a surrounding electric field gradient. Since spin $I > \frac{1}{2}$ nuclei are not examined in this work a detailed description of the quadrupolar coupling was deemed unnecessary.

1.2.8 Knight Shift

A coupling between an unpaired electron and a nucleus, known as the *hyperfine coupling*, can produce a change in the δ value of the nucleus. Unlike nuclei which have a small Zeeman splitting in a magnetic field, electrons (spin-1/2) have a Zeeman splitting that is three orders of magnitude larger and thus there is usually a Boltzmann population differential. The hyperfine coupling results in the nuclear resonance being split into a doublet and the population difference results in this doublet being asymmetric. Over the timescale of an experimental acquisition, the very fast relaxation (c.f. Section 1.2.10) of the electron reduces this doublet to a singlet. Furthermore, the position of this singlet is determined by the asymmetric nature of the doublet and thus the population difference. This shift in position of the nuclear resonance due to a hyperfine coupling is known as the *Knight shift*.

1.2.9 The Density Operator

The *density operator* is defined as

$$\hat{\rho} = \overline{|\psi\rangle\langle\psi|} \tag{1.2.29}$$

The overbar indicates that an ensemble average is taken. This means that the density operator describes the spin system as a whole (the bulk magnetization) rather than describing individual spins. The state vector representing a spin-1/2 nucleus can be given by a superposition of the $|\alpha\rangle$ and $|\beta\rangle$ states

$$|\psi\rangle = c_\alpha|\alpha\rangle + c_\beta|\beta\rangle \qquad \langle\psi| = c_\alpha^*\langle\alpha| + c_\beta^*\langle\beta| \tag{1.2.30}$$

with c_α and c_β as time-dependent coefficients which define the superposition state and c_α^* and c_β^* as their complex conjugates. Since the elements of a matrix representation of an operator $\hat{Q}$ are given by

$$Q_{ij} = \langle i|\hat{Q}|j\rangle \tag{1.2.31}$$

then ρ, the matrix representation of the density operator is

$$\rho = \begin{pmatrix} \overline{c_\alpha c_\alpha^*} & \overline{c_\alpha c_\beta^*} \\ \overline{c_\beta c_\alpha^*} & \overline{c_\beta c_\beta^*} \end{pmatrix} \tag{1.2.32}$$

The diagonal elements represent the populations of the $|\alpha\rangle$ and $|\beta\rangle$ spin states. The off-diagonal elements represent *coherences* between the $|\alpha\rangle$ and $|\beta\rangle$ spin states. Taking the time-dependent Schrödinger equation (TDSE),

$$\frac{\mathrm{d}|\psi(t)\rangle}{\mathrm{d}t} = -i\hat{\mathcal{H}}|\psi(t)\rangle \tag{1.2.33}$$

it follows that

$$\frac{\mathrm{d}|\hat{\rho}(t)\rangle}{\mathrm{d}t} = -i\left(\hat{\mathcal{H}}\hat{\rho}(t) - \hat{\rho}(t)\hat{\mathcal{H}}\right) \tag{1.2.34}$$

which is known as the *Liouville-von Neumann* equation. If the Hamiltonian is time independent the solution of this equation is

$$\hat{\rho}(t) = \exp(-i\hat{\mathcal{H}}t)\hat{\rho}(0)\exp(i\hat{\mathcal{H}}t) \tag{1.2.35}$$

where $\hat{\rho}(t)$ and $\hat{\rho}(0)$ are the density operators at time t and time zero (the initial density operator), respectively.

The matrix representation of the density operator can be expressed as a linear combination of the matrices representing $\hat{I}_x$, $\hat{I}_y$, $\hat{I}_z$ and $\hat{E}$.

$$\hat{\rho} = a_x\hat{I}_x + a_y\hat{I}_y + a_z\hat{I}_z + a_E\hat{E} \tag{1.2.36}$$

where

$$\hat{I}_x = \begin{pmatrix} 0 & \frac{1}{2} \\ \frac{1}{2} & 0 \end{pmatrix} \quad \hat{I}_y = \begin{pmatrix} 0 & -\frac{1}{2}i \\ \frac{1}{2}i & 0 \end{pmatrix} \quad \hat{I}_z = \begin{pmatrix} \frac{1}{2} & 0 \\ 0 & -\frac{1}{2} \end{pmatrix} \quad \hat{E} = \begin{pmatrix} 1 & 0 \\ 0 & 1 \end{pmatrix} \tag{1.2.37}$$

The density operator can therefore be written as

$$\rho = a_x \begin{pmatrix} 0 & \frac{1}{2} \\ \frac{1}{2} & 0 \end{pmatrix} + a_y \begin{pmatrix} 0 & -\frac{1}{2}i \\ \frac{1}{2}i & 0 \end{pmatrix} + a_z \begin{pmatrix} \frac{1}{2} & 0 \\ 0 & -\frac{1}{2} \end{pmatrix} + a_E \begin{pmatrix} 1 & 0 \\ 0 & 1 \end{pmatrix} \tag{1.2.38}$$

and thus

$$\rho = \frac{1}{2} \begin{pmatrix} 2a_E + a_z & a_x - ia_y \\ a_x + ia_y & 2a_E - a_z \end{pmatrix} \tag{1.2.39}$$

The coefficients a_x, a_y and a_z are simply numbers that vary with time and are related to the bulk magnetization.

$$M_x(t) \propto a_x(t) \qquad M_y(t) \propto a_y(t) \qquad M_z(t) \propto a_z(t) \tag{1.2.40}$$

$M_i(t)$ is the bulk magnetization along the i-axis and is time dependent. The magnitude of the signal cannot be measured absolutely by NMR and the size is irrelevant for our purposes so the constant of proportionality can be ignored:

$$M_x(t) = a_x(t) \qquad M_y(t) = a_y(t) \qquad M_z(t) = a_z(t) \tag{1.2.41}$$

It can be seen that the coefficient a_E is not of consequence to the evolution of the magnetization and so the *reduced* density operator can be written as

$$\hat{\rho}(t) = a_x(t)\hat{I}_x + a_y(t)\hat{I}_y + a_z(t)\hat{I}_z \tag{1.2.42}$$

The reduced density operator will simply be referred to as the density operator henceforth.

1.2.10 Relaxation

Any non-equilibrium magnetization will eventually *relax* to an equilibrium state. In NMR the equilibrium state is M_z, caused by the application of the large external magnetic field along the z-axis. If we induce a magnetization along the x-axis so that at time zero $a_x = 1$ and $a_z = 0$ then the density operator can be written

$$\hat{\rho}(0) = 1\hat{I}_x + 0\hat{I}_y + 0\hat{I}_z \tag{1.2.43}$$

After a long time (t_{long}) allowing the magnetization to have completely relaxed to equilibrium the density operator will be

$$\hat{\rho}(t_{long}) = 0\hat{I}_x + 0\hat{I}_y + 1\hat{I}_z \tag{1.2.44}$$

There are two major relaxation processes: longitudinal (or spin-lattice) relaxation with time constant T_1 and transverse (or spin-spin) relaxation with time constant T_2.

T_1 relaxation is the process by which M_z is recovered:

$$M_z(t) = M_{z,eq} - (M_{z,eq} - M_z(0))e^{-t/T_1} \tag{1.2.45}$$

$M_{z,eq}$ is the equilibrium value of M_z. T_1 relaxation occurs due to interactions with the lattice in which the nuclear spin undergoing relaxation resides. Hence, this relaxation is sometimes known as spin-lattice relaxation. These interactions with the lattice cause small fluctuations in the magnitude and direction of the magnetic field experienced by a nuclear spin. Over time these random fluctuations result in the magnetic moment of the spin being oriented in various directions. However, there is a slight bias to having the magnetic moment of a nuclear spin aligned parallel to the magnetic field since this is more energetically favourable. Eventually *thermal equilibrium* will be reached where there is a net magnetization aligned with the magnetic field.

T_2 relaxation is a process whereby magnetization in the xy-plane loses its coherence. Eventually, a loss of coherence will result in no net xy magnetization:

$$M_{xy}(t) = M_{xy}(0)e^{-t/T_2} \tag{1.2.46}$$

Motion of the magnetic moments of nuclear spins causes random variations in the local fields experienced by other nuclear spins. This causes these nuclear spins to precess at slightly different frequencies and hence causes a loss of co-

herence between the spins. This relaxation is sometimes referred to as spin-spin relaxation.

T_2 relaxation can be obscured by inhomogeneity in the static magnetic field. Magnetic field inhomogeneity results in different precession frequencies for equivalent spins that have different locations in the magnetic field. This causes a dephasing of these spins. The relationship between T_2 relaxation time and the experimentally observed *effective transverse relaxation time* (T_2^*) is

$$\frac{1}{T_2^*} = \frac{1}{T_2} + \frac{1}{T_{\text{inhom}}} \tag{1.2.47}$$

where T_{inhom} is the dephasing time due to the inhomogeneity of the static magnetic field. It can be seen that the combination of T_2 relaxation and magnetic field inhomogeneity leads to a shorter dephasing time of the transverse magnetization. The practical implication of T_2^* relaxation is the decay time of the free induction in the coil as a result of the evolving magnetization within the sample. Hence, the observable NMR signal is referred to as the FID (*free induction decay*). If a system contains only one spin that precesses with a given offset, then it would be expected that the corresponding NMR spectrum would consist of a single sharp line at that offset. However, signal decay due to T_2^* relaxation results in a line (or peak) with a Voigt lineshape[2] and an inherent linewidth. In solid-state NMR

[2]A Voigt lineshape is a convolution of a Gaussian lineshape with a Lorentzian lineshape.

a Voigt profile is created by a Gaussian lineshape due to dipolar couplings and a Lorentzian lineshape due to various dynamical effects [1, 2]. The linewidth is measured by the *FWHM* (full width at half-maximum) of the line where

$$\text{FWHM} = w_{\frac{1}{2}} = 1/\pi T_2^* \tag{1.2.48}$$

The contribution to the total dephasing from the inhomogeneity of the static magnetic field can be removed experimentally. The inhomogeneity is not random and is location dependent. This means that, in a solid sample, the effect is consistent over time. If transverse magnetization is allowed to dephase due to magnetic field inhomogeneity for a certain time, τ, and then the magnetization vectors are reflected about one axis in the transverse plane by a pulse of RF radiation and subsequently left to evolve for τ again, then the magnetization will "re-phase". This re-phasing of the magnetization is also known as *refocusing*. Refocusing is the basis behind the spin echo experiment which will be described in more detail later.

For solids T_1 is typically larger than T_2 with T_1 times of the order of seconds and T_2 times of the order of milliseconds.

1.2.11 Product Operators

A *product operator* analysis [3] is a quantum mechanical treatment used to describe spin systems. It is particularly useful for detailing steps in a NMR experiment with more than one RF pulse - a multiple-pulse experiment.

At equilibrium the bulk magnetization is M_z so that

$$\hat{\rho}_{\text{eq}} = \hat{I}_z \tag{1.2.49}$$

Consider a period of free precession of one spin, where the magnetic field is only along the z-direction. In the rotating frame, the Hamiltonian for free precession is

$$\hat{\mathcal{H}}_{\text{free}} = \Omega \hat{I}_z \tag{1.2.50}$$

which is analogous to the Zeeman Hamiltonian in equation (1.2.6) except where Ω is the *offset* of the spin; the difference between its Larmor frequency and the frequency of the rotating frame. Now consider the application of a RF pulse along the x-direction. From equations (1.2.50) and (1.2.9) it can be seen that

$$\hat{\mathcal{H}}_{x\text{-pulse}} = \Omega \hat{I}_z + \omega_1 \hat{I}_x \tag{1.2.51}$$

This is a combination of the Hamiltonian for free precession and the Hamiltonian

for a RF pulse along the x-axis. If we take the RF pulse to be a *hard* pulse (where $\omega_1 >> \Omega$) then the evolution of the spin is governed by the pulse.

$$\hat{\mathcal{H}}_{x\text{-hardpulse}} = \omega_1 \hat{I}_x \tag{1.2.52}$$

If we start with equilibrium magnetization

$$\hat{\rho}_{\text{eq}} = \hat{\rho}(0) = \hat{I}_z$$

and apply a hard x-pulse (equation (1.2.52)), the state of the density operator after this pulse can be worked out using the solution to the Liouville-von Neumann equation (1.2.35)

$$\begin{aligned} \hat{\rho}(t) &= \exp(-i\hat{\mathcal{H}}t)\hat{\rho}(0)\exp(i\hat{\mathcal{H}}t) \\ &= \exp(-i\omega_1\hat{I}_x t)\hat{I}_z \exp(i\omega_1\hat{I}_x t) \end{aligned} \tag{1.2.53}$$

Since $\hat{I}_x$, $\hat{I}_y$ and $\hat{I}_z$ cyclically commute then the *sandwich formula*[3] applies:

$$\exp(-i\theta\hat{I}_x)\hat{I}_z\exp(i\theta\hat{I}_x) \equiv \cos\theta\hat{I}_z - \sin\theta\hat{I}_y \tag{1.2.54}$$

and so

$$\hat{\rho}(t) = \cos\omega_1 t\hat{I}_z - \sin\omega_1 t\hat{I}_y \tag{1.2.55}$$

[3]A proof of the sandwich formula can be found in Appendix 17.1 of 'Spin Dynamics' by Levitt [4].

$\omega_1 t$ is known as the *flip angle* of the pulse. If we apply a 90° pulse (flip angle $\pi/2$) then

$$\hat{\rho}(t) = -\hat{I}_y \tag{1.2.56}$$

These product operator calculations are usually written in the form

$$\hat{\rho}(0) \xrightarrow{\hat{\mathcal{H}}t} \hat{\rho}(t) \tag{1.2.57}$$

therefore

$$\begin{aligned} \hat{I}_z &\xrightarrow{\omega_1 t \hat{I}_x} \cos\omega_1 t \hat{I}_z - \sin\omega_1 t \hat{I}_y \\ \hat{I}_z &\xrightarrow{(\pi/2)(\hat{I}_x)} -\hat{I}_y \end{aligned} \tag{1.2.58}$$

In words, a hard x-pulse with flip angle $\pi/2$ has *rotated* equilibrium z-magnetization about the x-axis by $\pi/2$. This rotation results in y-magnetization.

Table 1.2.1 shows the resulting identities for operator rotations. This is the basis for product operator calculations. So far only one spin has been considered and spin relaxation has been ignored. In the cases described it is not necessary to include relaxation processes although it is worth noting that they are present and are just excluded for simplicity. When considering systems of more than one spin, coupling between spins has to be taken into account. The density operator for a system of two spins can be represented by a linear combination of fifteen

Table 1.2.1: Identities of angular momentum operators.

rotation about	operator	identity
x	$\hat{I}_x$	$\exp(-i\theta\hat{I}_x)\hat{I}_x\exp(i\theta\hat{I}_x) \equiv \hat{I}_x$
x	$\hat{I}_y$	$\exp(-i\theta\hat{I}_x)\hat{I}_y\exp(i\theta\hat{I}_x) \equiv \cos\theta\hat{I}_y + \sin\theta\hat{I}_z$
x	$\hat{I}_z$	$\exp(-i\theta\hat{I}_x)\hat{I}_z\exp(i\theta\hat{I}_x) \equiv \cos\theta\hat{I}_z - \sin\theta\hat{I}_y$
y	$\hat{I}_x$	$\exp(-i\theta\hat{I}_y)\hat{I}_x\exp(i\theta\hat{I}_y) \equiv \cos\theta\hat{I}_x - \sin\theta\hat{I}_z$
y	$\hat{I}_y$	$\exp(-i\theta\hat{I}_y)\hat{I}_y\exp(i\theta\hat{I}_y) \equiv \hat{I}_y$
y	$\hat{I}_z$	$\exp(-i\theta\hat{I}_y)\hat{I}_z\exp(i\theta\hat{I}_y) \equiv \cos\theta\hat{I}_z + \sin\theta\hat{I}_x$
z	$\hat{I}_x$	$\exp(-i\theta\hat{I}_z)\hat{I}_x\exp(i\theta\hat{I}_z) \equiv \cos\theta\hat{I}_x + \sin\theta\hat{I}_y$
z	$\hat{I}_y$	$\exp(-i\theta\hat{I}_z)\hat{I}_y\exp(i\theta\hat{I}_z) \equiv \cos\theta\hat{I}_y - \sin\theta\hat{I}_x$
z	$\hat{I}_z$	$\exp(-i\theta\hat{I}_z)\hat{I}_z\exp(i\theta\hat{I}_z) \equiv \hat{I}_z$

operators, whereas for one spin the density operator could be represented by only $\hat{I}_x$, $\hat{I}_y$ and $\hat{I}_z$. Table 1.2.2 gives a summary of these fifteen operators, along with their description.

The Hamiltonian for free precession of two spins varies from that of equation (1.2.50) via an adaption to account for the coupling between the two spins. These spins also now evolve under the weak scalar coupling Hamiltonian (equation (1.2.28)) during periods of free precession.

$$\hat{\mathcal{H}}_{\text{free-two spins}} = \Omega_1\hat{I}_{1z} + \Omega_2\hat{I}_{2z} + 2\pi J_{12}\hat{I}_{1z}\hat{I}_{2z} \tag{1.2.59}$$

Ω_1 and Ω_2 are the offsets of spin one and spin two, respectively. The scalar coupling constant between spin one and spin two, J_{12}, is given in Hz. Since the

Table 1.2.2: Descriptions of operators for a two-spin system.

operator	description
$\hat{I}_{1z}$	z-magnetization on spin one
$\hat{I}_{1x}, \hat{I}_{1y}$	in-phase x- and y-magnetization on spin one
$2\hat{I}_{1x}\hat{I}_{2z}, 2\hat{I}_{1y}\hat{I}_{2z}$	anti-phase x- and y-magnetization on spin one
$\hat{I}_{2z}$	z-magnetization on spin two
$\hat{I}_{2x}, \hat{I}_{2y}$	in-phase x- and y-magnetization on spin two
$2\hat{I}_{1z}\hat{I}_{2x}, 2\hat{I}_{1z}\hat{I}_{2y}$	anti-phase x- and y-magnetization on spin two
$2\hat{I}_{1x}\hat{I}_{2x}, 2\hat{I}_{1x}\hat{I}_{2y}, 2\hat{I}_{1y}\hat{I}_{2x}, 2\hat{I}_{1y}\hat{I}_{2y}$	multiple-quantum coherence
$2\hat{I}_{1z}\hat{I}_{2z}$	non-equilibrium population

Table 1.2.3: Further identities of angular momentum operators.

operator	identity
$\hat{I}_{1x}$	$\exp(-i\theta\hat{I}_{1z}\hat{I}_{2z})\hat{I}_{1x}\exp(i\theta\hat{I}_{1z}\hat{I}_{2z}) \equiv \cos\left(\frac{1}{2}\theta\right)\hat{I}_{1x} + \sin\left(\frac{1}{2}\theta\right)2\hat{I}_{1y}\hat{I}_{2z}$
$\hat{I}_{1y}$	$\exp(-i\theta\hat{I}_{1z}\hat{I}_{2z})\hat{I}_{1y}\exp(i\theta\hat{I}_{1z}\hat{I}_{2z}) \equiv \cos\left(\frac{1}{2}\theta\right)\hat{I}_{1y} - \sin\left(\frac{1}{2}\theta\right)2\hat{I}_{1x}\hat{I}_{2z}$
$2\hat{I}_{1x}\hat{I}_{2z}$	$\exp(-i\theta\hat{I}_{1z}\hat{I}_{2z})2\hat{I}_{1x}\hat{I}_{2z}\exp(i\theta\hat{I}_{1z}\hat{I}_{2z}) \equiv \cos\left(\frac{1}{2}\theta\right)2\hat{I}_{1x}\hat{I}_{2z} + \sin\left(\frac{1}{2}\theta\right)\hat{I}_{1y}$
$2\hat{I}_{1y}\hat{I}_{2z}$	$\exp(-i\theta\hat{I}_{1z}\hat{I}_{2z})2\hat{I}_{1y}\hat{I}_{2z}\exp(i\theta\hat{I}_{1z}\hat{I}_{2z}) \equiv \cos\left(\frac{1}{2}\theta\right)2\hat{I}_{1y}\hat{I}_{2z} - \sin\left(\frac{1}{2}\theta\right)\hat{I}_{1x}$

operators in equation (1.2.59) commute then the product operator analysis under this Hamiltonian can be performed separately and in any order.

$$
\begin{aligned}
& \hat{\rho}(0) \xrightarrow{\hat{\mathcal{H}}_{\text{free-two spins}}t} \hat{\rho}(t) \\
\equiv \quad & \hat{\rho}(0) \xrightarrow{\Omega_1\hat{I}_{1z}t} \xrightarrow{\Omega_2\hat{I}_{2z}t} \xrightarrow{2\pi J_{12}\hat{I}_{1z}\hat{I}_{2z}t} \hat{\rho}(t) \\
\equiv \quad & \hat{\rho}(0) \xrightarrow{\Omega_1\hat{I}_{1z}t} \xrightarrow{2\pi J_{12}\hat{I}_{1z}\hat{I}_{2z}t} \xrightarrow{\Omega_2\hat{I}_{2z}t} \hat{\rho}(t)
\end{aligned}
\tag{1.2.60}
$$

The identities that are needed to understand the effect of the weak scalar coupling

Hamiltonian are given in Table 1.2.3. From Table 1.2.2 and Table 1.2.3 it can be seen that the scalar coupling has no effect on z-magnetization but has the effect of evolving in-phase x- (or y-) magnetization into anti-phase magnetization:

$$\begin{aligned}
&\hat{I}_{1z} \xrightarrow{2\pi J_{12}\hat{I}_{1z}\hat{I}_{2z}t} \hat{I}_{1z} \\
&\hat{I}_{1x} \xrightarrow{2\pi J_{12}\hat{I}_{1z}\hat{I}_{2z}t} \cos(\pi J_{12}t)\,\hat{I}_{1x} + \sin(\pi J_{12}t)\,2\hat{I}_{1y}\hat{I}_{2z}
\end{aligned} \tag{1.2.61}$$

As with the commutation of the operators involved in free precession, the operators involved in RF pulses also commute so that

$$\begin{aligned}
&\hat{\rho}(0) \xrightarrow{\hat{\mathcal{H}}_{x\text{-hardpulse for two spins}}t} \hat{\rho}(t) \\
\equiv\ &\hat{\rho}(0) \xrightarrow{\omega_1\hat{I}_{1x}t}\xrightarrow{\omega_2\hat{I}_{2x}t} \hat{\rho}(t) \\
\equiv\ &\hat{\rho}(0) \xrightarrow{\omega_2\hat{I}_{2x}t}\xrightarrow{\omega_1\hat{I}_{1x}t} \hat{\rho}(t)
\end{aligned} \tag{1.2.62}$$

A spin echo is a period of delay followed by a RF pulse applied to both spins with a flip angle of π, followed by the same period of delay. This is a special sequence that must be mentioned. Due to the commutation of the operators

$$\begin{aligned}
&\hat{\rho}(0) \xrightarrow{\text{spin echo}} \hat{\rho}(t) \\
\equiv\ &\hat{\rho}(0) \xrightarrow{\Omega_1\hat{I}_{1z}t}\xrightarrow{\Omega_2\hat{I}_{2z}t}\xrightarrow{2\pi J_{12}\hat{I}_{1z}\hat{I}_{2z}t}\xrightarrow{\pi(\hat{I}_{1x}+\hat{I}_{2x})}\xrightarrow{\Omega_1\hat{I}_{1z}t}\xrightarrow{\Omega_2\hat{I}_{2z}t}\xrightarrow{2\pi J_{12}\hat{I}_{1z}\hat{I}_{2z}t} \hat{\rho}(t) \\
\equiv\ &\hat{\rho}(0) \xrightarrow{4\pi J_{12}\hat{I}_{1z}\hat{I}_{2z}t}\xrightarrow{\Omega_1\hat{I}_{1z}t}\xrightarrow{\Omega_2\hat{I}_{2z}t}\xrightarrow{\pi(\hat{I}_{1x}+\hat{I}_{2x})}\xrightarrow{\Omega_1\hat{I}_{1z}t}\xrightarrow{\Omega_2\hat{I}_{2z}t} \hat{\rho}(t)
\end{aligned} \tag{1.2.63}$$

Starting with x-magnetization on spin one and spin two and applying a spin echo sequence

$$\begin{aligned}
&\hat{I}_{1x} + \hat{I}_{2x} \xrightarrow{4\pi J_{12}\hat{I}_{1z}\hat{I}_{2z}t} \xrightarrow{\Omega_1\hat{I}_{1z}t} \xrightarrow{\Omega_2\hat{I}_{2z}t} \xrightarrow{\pi(\hat{I}_{1x}+\hat{I}_{2x})} \xrightarrow{\Omega_1\hat{I}_{1z}t} \xrightarrow{\Omega_2\hat{I}_{2z}t} \\
&\quad \cos(2\pi J_{12}t)\left[\cos(\Omega_1 t)\left\{\cos(\Omega_1 t)\,\hat{I}_{1x} + \sin(\Omega_1 t)\,\hat{I}_{1y}\right\} - \right. \\
&\quad \left. \sin(\Omega_1 t)\left\{\cos(\Omega_1 t)\,\hat{I}_{1y} - \sin(\Omega_1 t)\,\hat{I}_{1x}\right\}\right] - \\
&\quad \sin(2\pi J_{12}t)\left[\cos(\Omega_1 t)\left\{\cos(\Omega_1 t)\,2\hat{I}_{1y}\hat{I}_{2z} - \sin(\Omega_1 t)\,2\hat{I}_{1x}\hat{I}_{2z}\right\} + \right. \\
&\quad \left. \sin(\Omega_1 t)\left\{\cos(\Omega_1 t)\,2\hat{I}_{1x}\hat{I}_{2z} + \sin(\Omega_1 t)\,2\hat{I}_{1y}\hat{I}_{2z}\right\}\right] + \\
&\quad \cos(2\pi J_{12}t)\left[\cos(\Omega_2 t)\left\{\cos(\Omega_2 t)\,\hat{I}_{2x} + \sin(\Omega_2 t)\,\hat{I}_{2y}\right\} - \right. \\
&\quad \left. \sin(\Omega_2 t)\left\{\cos(\Omega_2 t)\,\hat{I}_{2y} - \sin(\Omega_2 t)\,\hat{I}_{2x}\right\}\right] - \\
&\quad \sin(2\pi J_{12}t)\left[\cos(\Omega_2 t)\left\{\cos(\Omega_2 t)\,2\hat{I}_{1z}\hat{I}_{2y} - \sin(\Omega_2 t)\,2\hat{I}_{1z}\hat{I}_{2x}\right\} + \right. \\
&\quad \left. \sin(\Omega_2 t)\left\{\cos(\Omega_2 t)\,2\hat{I}_{1z}\hat{I}_{2x} + \sin(\Omega_2 t)\,2\hat{I}_{1z}\hat{I}_{2x}\right\}\right]
\end{aligned}$$

It can be seen that the terms in $\hat{I}_y$ and $2\hat{I}_x\hat{I}_z$ cancel each other out leaving

$$\begin{aligned}
&\cos(2\pi J_{12}t)\left[\cos(\Omega_1 t)\left\{\cos(\Omega_1 t)\,\hat{I}_{1x}\right\} + \sin(\Omega_1 t)\left\{\sin(\Omega_1 t)\,\hat{I}_{1x}\right\}\right] - \\
&\sin(2\pi J_{12}t)\left[\cos(\Omega_1 t)\left\{\cos(\Omega_1 t)\,2\hat{I}_{1y}\hat{I}_{2z}\right\} + \sin(\Omega_1 t)\left\{\sin(\Omega_1 t)\,2\hat{I}_{1y}\hat{I}_{2z}\right\}\right] + \\
&\cos(2\pi J_{12}t)\left[\cos(\Omega_2 t)\left\{\cos(\Omega_2 t)\,\hat{I}_{2x}\right\} + \sin(\Omega_2 t)\left\{\sin(\Omega_2 t)\,\hat{I}_{2x}\right\}\right] - \\
&\sin(2\pi J_{12}t)\left[\cos(\Omega_2 t)\left\{\cos(\Omega_2 t)\,2\hat{I}_{1z}\hat{I}_{2y}\right\} + \sin(\Omega_2 t)\left\{\sin(\Omega_2 t)\,2\hat{I}_{1z}\hat{I}_{2y}\right\}\right]
\end{aligned}$$

Using the identity

$$\cos^2\theta + \sin^2\theta \equiv 1 \tag{1.2.64}$$

the resulting density operator is

$$\cos\left(2\pi J_{12}t\right)\left[\hat{I}_{1x} + \hat{I}_{2x}\right] - \sin\left(2\pi J_{12}t\right)\left[2\hat{I}_{1y}\hat{I}_{2z} + 2\hat{I}_{1z}\hat{I}_{2y}\right] \tag{1.2.65}$$

The final state of the system does not depend upon the offsets of spin one and spin two. Along with dephasing of transverse magnetization due to an inhomogeneous static magnetic field, the spin echo also has a refocusing effect on the offsets; it appears that no offset evolution has taken place. However, the evolution of the scalar coupling has not been refocused and the density operator is now a combination of in-phase and anti-phase magnetization. When applying the product operator approach to a spin echo, evolution of the offsets can be ignored so that equation (1.2.63) becomes

$$\begin{aligned} & \hat{\rho}(0) \xrightarrow{\text{spin echo}} \hat{\rho}(t) \\ \equiv \quad & \hat{\rho}(0) \xrightarrow{4\pi J_{12}\hat{I}_{1z}\hat{I}_{2z}t} \xrightarrow{\pi(\hat{I}_{1x}+\hat{I}_{2x})} \hat{\rho}(t) \end{aligned} \tag{1.2.66}$$

Another point that merits mentioning is magnetization transfer. This is an important step in many multiple-pulse NMR experiments. Suppose a two spin system has been allowed to evolve under the scalar coupling so that anti-phase

magnetization along the y-axis on spin one is present. A RF pulse of flip angle $\pi/2$ applied to both spins along the x-axis will transfer magnetization between the two spins.

$$2\hat{I}_{1y}\hat{I}_{2z} \xrightarrow{\pi/2(\hat{I}_{2x}+\hat{I}_{2x})} -2\hat{I}_{1z}\hat{I}_{2y} \tag{1.2.67}$$

Transverse magnetization on spin one becomes transverse magnetization on spin two. It is only anti-phase magnetization that can undergo this transfer after the application of a suitable RF pulse and since anti-phase magnetization can generally only arise due to the presence of a coupling between spins then the presence of a coupling is necessary for magnetization transfer. This process of magnetization transfer can also be referred to as *coherence transfer* since it involves transfer between the off-diagonal elements (the coherences) of the density matrix.

$$\hat{\rho} = \begin{pmatrix} \alpha\alpha & SQ & SQ & DQ \\ SQ & \alpha\beta & ZQ & SQ \\ SQ & ZQ & \beta\alpha & SQ \\ DQ & SQ & SQ & \beta\beta \end{pmatrix} \tag{1.2.68}$$

ZQ = zero-quantum coherence, SQ = single-quantum coherence and DQ = double-quantum coherence.

1.2.12 Coherence Order

The *coherence order*, p, is defined by the result of the application of a rotation about the z-axis through an angle ϕ to an operator or product of operators [5]:

$$\hat{I}^{(p)} \xrightarrow{\phi\hat{I}_z} \hat{I}^{(p)} \exp(-ip\phi) \tag{1.2.69}$$

where $\hat{I}^{(p)}$ is an operator with coherence order p. $\hat{I}_z$ has a coherence order of zero since it is unaffected by a rotation about the z-axis. The operators $\hat{I}_+$ (the *raising operator*) and $\hat{I}_-$ (the *lowering operator*) are useful for expanding the density operator in a way which makes the coherence order clear. They are defined as

$$\hat{I}_+ \equiv \hat{I}_x + i\hat{I}_y \qquad \hat{I}_- \equiv \hat{I}_x - i\hat{I}_y \tag{1.2.70}$$

$\hat{I}_+$ has a coherence order of +1 and $\hat{I}_-$ has a coherence order of -1.

$$\begin{aligned}
\hat{I}_+ \equiv \hat{I}_x + i\hat{I}_y \xrightarrow{\phi\hat{I}_z} \quad & \cos\phi\hat{I}_x + \sin\phi\hat{I}_y + i(\cos\phi\hat{I}_y - \sin\phi\hat{I}_x) \\
= \quad & \cos\phi(\hat{I}_x + i\hat{I}_y) - i\sin\phi(\hat{I}_x + i\hat{I}_y) \\
= \quad & (\cos\phi - i\sin\phi)(\hat{I}_x + i\hat{I}_y) \\
= \quad & \exp(-i\phi)\hat{I}_+
\end{aligned} \tag{1.2.71}$$

$$\begin{aligned}\hat{I}_- \equiv \hat{I}_x - i\hat{I}_y \xrightarrow{\phi\hat{I}_z} \quad & \cos\phi\hat{I}_x + \sin\phi\hat{I}_y - i(\cos\phi\hat{I}_y - \sin\phi\hat{I}_x) \\ = \quad & \cos\phi(\hat{I}_x - i\hat{I}_y) + i\sin\phi(\hat{I}_x - i\hat{I}_y) \\ = \quad & (\cos\phi + i\sin\phi)(\hat{I}_x - i\hat{I}_y) \\ = \quad & \exp(+i\phi)\hat{I}_- \end{aligned} \tag{1.2.72}$$

Adding and subtracting the raising and lowering operators gives

$$\hat{I}_x \equiv \frac{1}{2}(\hat{I}_+ + \hat{I}_-) \qquad \hat{I}_y \equiv \frac{1}{2i}(\hat{I}_+ - \hat{I}_-) \tag{1.2.73}$$

respectively. It can be seen that $\hat{I}_x$ and $\hat{I}_y$ contain coherence orders +1 and -1 and thus these are *single-quantum coherence* operators. The product operator $2\hat{I}_x\hat{S}_x$ contains coherence orders ± 2 and 0 and is therefore a mixture of *double-quantum coherence* and *zero-quantum coherence* ($\hat{S}$ can be either homonuclear or heteronuclear to $\hat{I}$ in this case).

$$\begin{aligned}2\hat{I}_x\hat{S}_x \equiv \quad & 2 \times \frac{1}{2}(\hat{I}_+ + \hat{I}_-) \times \frac{1}{2}(\hat{S}_+ + \hat{S}_-) \\ & \frac{1}{2}(\underbrace{\hat{I}_+\hat{S}_+}_{p=+2} + \underbrace{\hat{I}_-\hat{S}_-}_{p=-2} + \underbrace{\hat{I}_+\hat{S}_-}_{p=0} + \underbrace{\hat{I}_-\hat{S}_+}_{p=0}) \end{aligned} \tag{1.2.74}$$

Table 1.2.4 lists the different types of coherence possible for a two spin system, along with the corresponding operator or product operators.

Table 1.2.4: Further descriptions of operators for a two-spin system.

operator	description
$\hat{I}_x$, $\hat{I}_y$, $2\hat{I}_x\hat{S}_z$, $2\hat{I}_y\hat{S}_z$	single-quantum coherence
$2\hat{I}_x\hat{S}_x - 2\hat{I}_y\hat{S}_y$	double-quantum x-coherence
$2\hat{I}_x\hat{S}_x + 2\hat{I}_y\hat{S}_y$	zero-quantum x-coherence
$2\hat{I}_x\hat{S}_y + 2\hat{I}_y\hat{S}_x$	double-quantum y-coherence
$2\hat{I}_y\hat{S}_x - 2\hat{I}_x\hat{S}_y$	zero-quantum y-coherence

1.3 Experimental Techniques for Solid-State NMR

1.3.1 Phase Cycling and the Coherence Transfer Pathway

For a NMR experiment, it is often required that certain coherence orders are selected and others ignored at various points. This is because, if the spin system is allowed to evolve through the application of RF pulses, coherence orders other than those that are desired in the experiment will also be created. The *coherence transfer pathway* (CTP) is a means of illustrating the desired coherences during a pulsed NMR experiment. Figure 1.3.1 shows a simple pulse sequence and corresponding CTP. This is the pulse sequence for a spin echo that is described in equation (1.2.66) in terms of product operators. However, unlike in equation (1.2.66) where one can assume that the experiment starts with x-magnetization on all spins, in a NMR experiment this transverse (x-) magnetization has to be created from equilibrium (z-) magnetization. This is achieved by the application

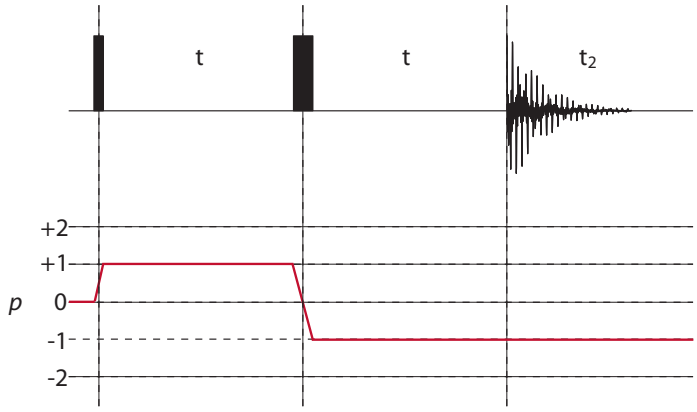

Figure 1.3.1: Pulse sequence used to record spin echo NMR spectra. Narrow and wide filled vertical bars represent $\pi/2$ and π pulses, respectively.

of a suitable RF pulse, as shown in Figure 1.3.1.

It can be seen from Figure 1.3.1 that the coherence order is zero at the beginning of the experiment, as would be expected for equilibrium ($\hat{I}_z$) magnetization. The coherence that is desired after the application of the first pulse is of order +1. A coherence order of -1 is then desired after the application of the second and final pulse in the sequence. A coherence order of -1 is required as the final coherence order because this is the coherence order that is detected in an experiment. The time-domain signal that a NMR experiment detects ($s(t)$) is

$$s(t) = Tr\left[\hat{I}_+ \, \hat{\rho}(t)\right] \tag{1.3.1}$$

where Tr is the Trace of the corresponding matrix (the sum of the diagonal elements). The multiplication of the raising operator and the final density matrix

means that the density matrix must contain a coherence order of -1.

Phase cycling [6] is one method that can be used to select only the desired coherences. For phase cycling, the NMR experiment is repeated and on each repetition the phase of one or more of the pulses and the phase of the receiver are varied in a predetermined manner. The repetitions are then combined and the desired CTP will be reinforced whereas the undesired pathways will be removed. The cycling of the pulse phases is predetermined using two rules [7]:

1. If the phase of a pulse (or group of pulses) is shifted by ϕ, then a coherence undergoing a change in coherence order Δp experiences a phase shift $-\phi\Delta p$ as detected by the receiver.

2. If a phase cycle uses steps of $360°/\mathrm{N}$ then, along with the desired pathway Δp, pathways $\Delta p \pm \mathrm{nN}$ where $\mathrm{n} = 1, 2, 3, \ldots$ will also be selected. All other pathways are suppressed.

Using the example of the CTP for a spin echo (Figure 1.3.1), a phase cycle can be constructed as follows. Starting on coherence order zero, a coherence change $\Delta p = +1$ is desired whilst all other coherence changes (+2, 0, -1, -2) are unwelcome. From rule 2 it can be seen that a four step phase cycle would suppress all coherences except +1 and $+1 \pm 4\mathrm{n}$, i.e. +1, +5, -3, ... Coherence

Table 1.3.1: Four step phase cycle and corresponding receiver phase used to select a +1 change in coherence order. All the phases are in degrees.

Step	ϕ	$-\phi$ = receiver phase
1	0	0 = 0
2	90	-90 = 270
3	180	-180 = 180
4	270	-270 = 90

orders $> \pm 2$ can be ignored. In this case these will contribute a negligible amount because they require the presence of three or more coupled spins. From rule 1 it can be seen that the phase of the receiver should be set to $-\phi\Delta p = -\phi$. Thus, the phase of the first pulse is stepped through 360° in four steps and the receiver is correspondingly cycled as shown in Table 1.3.1.

The phase of the second pulse does not need to be cycled. Since the start and end points of a CTP are fixed then the maximum number of pulses that may need to be cycled is the total number of pulses - 1. When there are two or more pulses that need to be phase cycled *nested* phase cycles are produced, i.e. phases are cycled within other phase cycles and the required receiver phases are co-added as illustrated in Table 1.3.2. The phase of the first pulse (ϕ_1) is a four step phase cycle which selects $\Delta p = +1$ and the phase of the second pulse (ϕ_2) is also a four step cycle but selects $\Delta p = -2$.

Pulsed field gradients can also be used to select the desired CTP but since this

Table 1.3.2: Nested phase cycle for a spin echo experiment. All the phases are in degrees.

Step	ϕ_1	ϕ_2	receiver phase
1	0	0	0
2	90	0	270
3	180	0	180
4	270	0	90
5	0	90	180
6	90	90	90
7	180	90	0
8	270	90	270
9	0	180	0
10	90	180	270
11	180	180	180
12	270	180	90
13	0	270	180
14	90	270	90
15	180	270	0
16	270	270	270

technique has not been used for any of the work in this thesis then it is simply worth mentioning without detail.

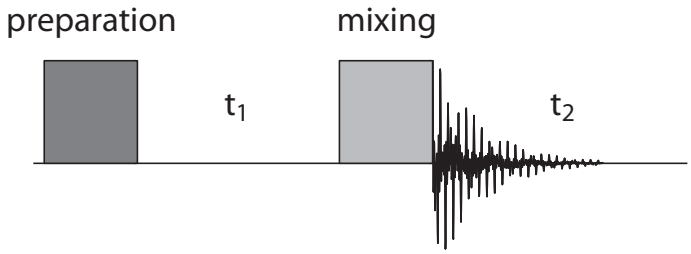

Figure 1.3.2: The general form of an experiment used to record two-dimensional NMR spectra.

1.3.2 Multi-dimensional NMR

Jeener (1971) and Ernst (1976) [8] are credited with the invention of multi-dimensional NMR spectroscopy. Consider the experiment that is illustrated in Figure 1.3.2. The experiment begins with a *preparation period*, which could be one pulse or a combination of pulses and delays, that creates a desired coherence using phase cycling. This desired coherence is then allowed to evolve during the *evolution period* (or *indirect detection period*), t_1. A *mixing period* is then employed that transforms the evolving coherence into observable magnetization that is detected during the *detection period* (or *direct detection period*), t_2. Selected coherences will evolve at a frequency of Ω_A during t_1 and Ω_B during t_2. By repeating the experiment whilst stepping the value of t_1 through a number of *increments*, the evolution of the magnetization during the t_1 period as a function of time can be determined from the modulation of the NMR signal detected during t_2. Since there is no direct observation of the magnetization during the

evolution period then any coherence order evolving during this time may be indirectly detected. The experiment described by incrementing t_1 will result in a two-dimensional data set. For higher-dimensional NMR, more evolution periods are required. Up to seven-dimensional NMR spectroscopy can be found in the literature to date [9]. Higher-dimensional NMR spectroscopy is useful for studying large molecules.

In modern day NMR experiments, the NMR signal ($s(t)$) is detected in *quadrature*.

$$s(t) = [C\cos(\Omega t) + iC\sin(\Omega t)]\exp(-t/T_2) \equiv C\exp(i\Omega t)\exp(-t/T_2) \quad (1.3.2)$$

Both the real and imaginary components must be measured so that a Fourier transform (FT) can be applied to the time-domain signal, $s(t)$, to obtain a frequency-domain signal, $s(\omega)$, (a spectrum) whilst retaining all the necessary information for *purely absorptive* frequency-domain lineshapes.

$$s(\omega) = \int_0^{+\infty} s(t)\exp(-i\omega t)\exp(-t/T_2) \quad (1.3.3)$$

This gives

$$\Re\{s(\omega)\} = \mathrm{A} = \frac{1/T_2}{(1/T_2)^2 + (\omega - \Omega)^2} \quad (1.3.4)$$

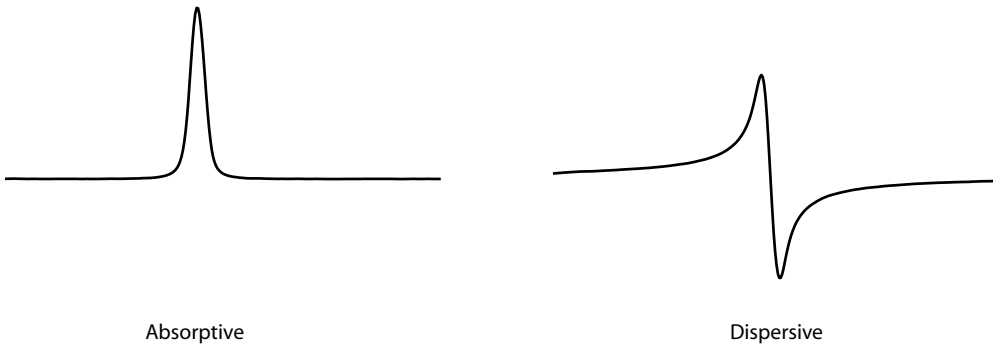

Figure 1.3.3: Illustration of absorptive and dispersive lineshapes.

and

$$\Im\{s(\omega)\} = i\mathrm{D} = \frac{\omega - \Omega}{(1/T_2)^2 + (\omega - \Omega)^2} \tag{1.3.5}$$

In a one-dimensional NMR experiment, *phasing* the frequency-domain signal can give the desired purely absorptive lineshapes. Absorptive (A) and dispersive (D) lineshapes are illustrated in Figure 1.3.3. For a purely absorptive one-dimensional spectrum, the real part of $s(\omega)$ (equation (1.3.4)) is fully absorptive and the imaginary part of $s(\omega)$ (equation (1.3.5)) is fully dispersive.

In two-dimensional NMR spectroscopy, the time-domain data set, $s(t_1, t_2)$, needs to undergo a double FT to give a frequency-domain data set, $s(\omega_1, \omega_2)$. A time-domain data set has the form

$$s(t_1, t_2) = \exp(i\Omega_A t_1) \exp(-t_1/T_2^{(1)}) \exp(i\Omega_B t_2) \exp(-t_2/T_2^{(2)}) \tag{1.3.6}$$

where Ω_A and Ω_B are the offsets of the spins during the time periods t_1 and t_2, respectively and $T_2^{(1)}$ and $T_2^{(2)}$ are the spin-spin relaxation constants during the time periods t_1 and t_2, respectively. Applying a Fourier transform with respect to t_2 gives

$$s(t_1, \omega_2) = \exp(i\Omega_A t_1) \exp(-t_1/T_2^{(1)})(\mathrm{A}_2 + i\mathrm{D}_2) \tag{1.3.7}$$

This resulting data set can be manipulated (phased) with respect to ω_2 so that an absorption mode lineshape is achieved in the real part with the corresponding dispersion mode lineshape in the imaginary part. Now applying a Fourier transform with respect to t_1 gives

$$\begin{aligned} s(\omega_1, \omega_2) &= (\mathrm{A}_1 + i\mathrm{D}_1)(\mathrm{A}_2 + i\mathrm{D}_2) \\ &= \mathrm{A}_1\mathrm{A}_2 + i\mathrm{A}_1\mathrm{D}_2 + i\mathrm{A}_2\mathrm{D}_1 - \mathrm{D}_1\mathrm{D}_2 \end{aligned} \tag{1.3.8}$$

This is a mixture of the different lineshapes. To obtain purely absorptive lineshapes and also *frequency discrimination*, $s(t_1, t_2)$ is *amplitude-modulated* with respect to t_1. Amplitude-modulation is achieved if $\pm p$ evolves during the t_1 period. Figure 1.3.4 shows the CTP required for an amplitude-modulated signal if double-quantum coherence is desired during t_1. With a time-domain signal that is amplitude-modulated with respect to t_1, one of two ubiquitous methods can be utilised to obtain the required two-dimensional spectrum with frequency discrimination and purely absorptive lineshapes: the States method [10] or TPPI

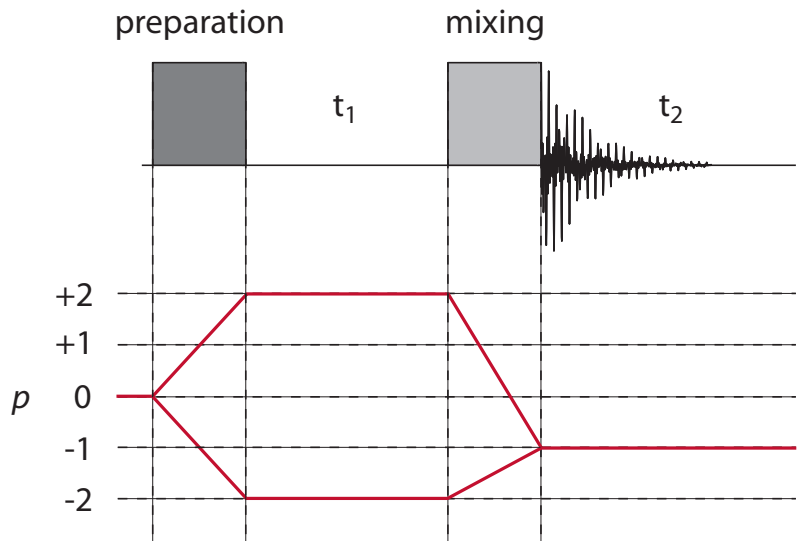

Figure 1.3.4: The general form of an experiment used to record two-dimensional NMR spectra with double-quantum coherence in the indirect dimension.

[11][4]. Time-proportional phase incrementation (TPPI) is the method that was preferred for the work herein. As the name suggests, this method involves incrementing pulse phases along with the incrementation of t_1. More precisely, all of the pulses before the t_1 evolution period that have an effect on the order of coherence have their phase incremented by $\pi/2p$ for each t_1 incrementation.

The time-domain signal obtained from a simple two-dimensional experiment has

[4]States-TPPI [12] is a third method but this is less commonly exploited.

the form

$$s(t_1, t_2) = [\exp(i\Omega_A t_1) + \exp(-i\Omega_A t_1)] \exp(-t_1/T_2^{(1)}) \exp(i\Omega_B t_2) \exp(-t_2/T_2^{(2)}) \tag{1.3.9}$$

The application of a Fourier transform with respect to t_2 gives

$$s(t_1, \omega_2) = [\exp(i\Omega_A t_1) + \exp(-i\Omega_A t_1)] \exp(-t_1/T_2^{(1)})[\mathrm{A}_2^+ + i\mathrm{D}_2^+] \tag{1.3.10}$$

The "+" on the A_2^+ and the $i\mathrm{D}_2^+$ denotes the sign of the offset. Discarding the imaginary part and applying a Fourier transform with respect to t_1 gives a frequency-domain signal of the form

$$\begin{aligned} s(\omega_1, \omega_2) &= [(\mathrm{A}_1^+ + i\mathrm{D}_1^+) + (\mathrm{A}_1^- + i\mathrm{D}_1^-)][\mathrm{A}_2^+] \\ &= (\mathrm{A}_1^+ + \mathrm{A}_1^-)\mathrm{A}_2^+ + i(\mathrm{D}_1^+ + \mathrm{D}_1^-)\mathrm{A}_2^+ \end{aligned} \tag{1.3.11}$$

The real part has a pure absorption mode lineshape. However, there is no frequency discrimination in the ω_1 dimension since both the positive and negative offsets will appear to be the same.

Since TPPI imposes a t_1 dependent phase modulation of $\exp(-i\pi t_1/2p\Delta t_1)$ (where

Δt_1 is the t_1 increment) then equation (1.3.9) becomes

$$s(t_1, t_2) = [\exp(i(\Omega_A + \pi/2p\Delta t_1)t_1) + \exp(-i(\Omega_A + \pi/2p\Delta t_1)t_1)] \exp(-t_1/T_2^{(1)}) \times \exp(i\Omega_B t_2) \exp(-t_2/T_2^{(2)}) \quad (1.3.12)$$

Δt_1 is related to the *spectral width*[5] (SW) in the ω_1 dimension by the relationship

$$\Delta t_1 = 1/\mathrm{SW} \quad (1.3.13)$$

However, in TPPI, Δt_1 is set to half of this value so that

$$s(t_1, t_2) = [\exp(i(\Omega_A + \pi \mathrm{SW}/p)t_1) + \exp(-i(\Omega_A + \pi \mathrm{SW}/p)t_1)] \exp(-t_1/T_2^{(1)}) \times \exp(i\Omega_B t_2) \exp(-t_2/T_2^{(2)}) \quad (1.3.14)$$

A Fourier transform of the time-domain signal with respect to t_2 gives

$$s(t_1, \omega_2) = [\exp(i(\Omega_A + \pi \mathrm{SW}/p)t_1) + \exp(-i(\Omega_A + \pi \mathrm{SW}/p)t_1)] \exp(-t_1/T_2^{(1)}) \times [\mathrm{A}_2^+ + i\mathrm{D}_2^+] \quad (1.3.15)$$

Using the relation

$$\cos\theta = \frac{1}{2}(e^{i\theta} + e^{-i\theta}) \quad (1.3.16)$$

[5]The spectral width is the maximum range of frequencies that can be accurately portrayed from the recorded signal. The spectral width is the inverse of the sampling interval (*dwell time*).

and discarding the imaginary part leaves

$$s(t_1, \omega_2) = 2[\cos((\Omega_A + \pi \mathrm{SW}/p)t_1)] \exp(-t_1/T_2^{(1)})[\mathrm{A}_2^+] \tag{1.3.17}$$

During an experiment, the desired spectral width is recorded over a frequency range from -SW/2 to SW/2. The result of adding πSW/p to Ω_A with TPPI, taking only the positive frequency half of the spectrum and performing a real Fourier transform with respect to t_1 is

$$\begin{aligned} s(\omega_1, \omega_2) &= (\mathrm{A}_1^+ + i\mathrm{D}_1^+)[\mathrm{A}_2^+] \\ &= \mathrm{A}_1^+\mathrm{A}_2^+ + i\mathrm{D}_1^+\mathrm{A}_2^+ \end{aligned} \tag{1.3.18}$$

The frequency-domain signal now has the desired frequency discrimination and pure absorption mode lineshapes in the real part of the spectrum.

$$\Re[s(\omega_1, \omega_2)] = \mathrm{A}_1^+\mathrm{A}_2^+ \tag{1.3.19}$$

In some cases the resulting peaks may not be purely absorptive. For example, the on-diagonal and off-diagonal peaks that result from the COSY (*COrrelation SpectroscopY*) experiment [8] have different lineshapes. However, this is not due to the method of data acquisition or data processing undertaken but is a fundamental property of the experiment.

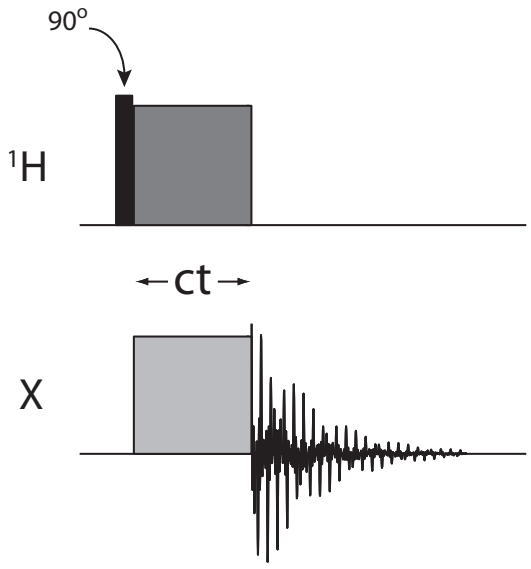

Figure 1.3.5: Pulse sequence used to record CP NMR spectra.

1.3.3 Cross-Polarization

Cross-polarization (CP) was introduced by Pines et al. [13] as a method of increasing the sensitivity of NMR experiments on spins with low isotopic abundance, such as carbon-13. Figure 1.3.5 illustrates the pulse sequence that generates cross-polarized magnetization. A pulse with flip angle $\pi/2$ is applied to an abundant spin-1/2 nucleus, in this case protons, to induce transverse magnetization. This transverse magnetization is transfered to the dilute nucleus (X) by the application of simultaneous long pulses to both the abundant and dilute spins and is mediated by the dipolar couplings between these spins. The simultaneous pulses

are applied according to the *Hartmann-Hahn* matching condition [14]:

$$\gamma_a B_1^a = \gamma_b B_1^b \tag{1.3.20}$$

so that the frequency of rotation about a transverse axis is the same for both nuclei (a and b). In this instance a redistribution of energy is facilitated and the magnetization of the dilute nucleus is enhanced by the magnetization of the abundant nucleus with a maximum enhancement determined by the ratio of the gyromagnetic ratios of the two spins. For protons transferring magnetization to carbon-13 nuclei the maximum enhancement is ~ 4.

The long pulses are applied for a certain *contact time* (ct). The ct is selected with competition between the signal build up due to transfer rate and the spin-lattice relaxation time of the abundant nucleus in the rotating frame determining the duration, usually a few milliseconds. Relaxation of abundant spins is often relatively fast as a result of the abundance of dipolar-couplings within the spin network. Thus, CP can also be used as a method of reducing experiment time since the delay time between experimental repetitions is governed by the relaxation of the abundant nucleus and not the dilute nucleus.

In practice, the amplitude of one of the simultaneous long pulses is *ramped* over a range of values that encompass the Hartmann-Hahn match. This increases the reliability of achieving the matching condition, especially under *magic angle*

spinning conditions [15].

1.3.4 Magic Angle Spinning

Both the CSA and dipolar couplings have an orientational dependence that effects the Zeeman energies of nuclei. For the CSA, the frequencies (energies) originating from different molecular orientations overlap to form a continuous lineshape, a *powder pattern*. For a pair of dipolar coupled spins the different molecular orientations result in another continuous lineshape, a *Pake pattern*. However, for a network of dipolar coupled spins the orientational variety leads to a range of local fields experienced by each spin and a Gaussian distribution of frequencies is observed, the size of which depends upon the strength of the coupling. The resultant *broadening* of the spectral lines causes the isotropic chemical shifts, which are desired in most NMR experiments, to be concealed. For an isotropic liquid the rapid and random molecular rotation has the effect of time averaging orientational dependences so the CSA and dipolar couplings tend to their isotropic values, δ_{iso} and zero, respectively.

Magic angle spinning (MAS) [16] has the effect of reducing the CSA and the dipolar couplings between spins so that the isotropic chemical shifts are more readily resolved. With MAS, the spin system under observation is rotated about an axis which is at an angle of 54.74° to the external magnetic field. This angle

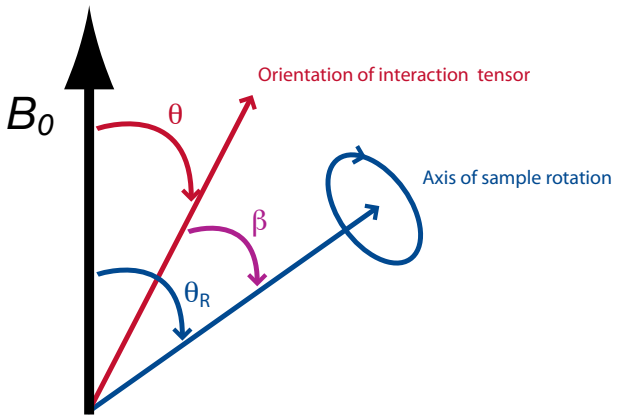

Figure 1.3.6: The axes of magic angle spinning.

is known as the *magic angle*. Figure 1.3.6 illustrates the important axes when considering MAS. In a powdered solid, the orientation of a spin interaction tensor, θ, can take any value. However, if the solid sample is rotated about an axis which is at an angle θ_R to the external magnetic field then θ varies with time. The average of the orientational dependence of the spin interaction tensor, $(3\cos^2\theta - 1)$, is then given by

$$\langle 3\cos^2\theta - 1\rangle = \frac{1}{2}(3\cos^2\theta_R - 1)(3\cos^2\beta - 1) \tag{1.3.21}$$

where β is the angle between the axis of sample rotation and the orientation of the spin interaction tensor. From equation (1.3.21) it can be seen that by setting $\theta_R = 54.74°$ so that $(3\cos^2\theta_R) = 1$, then $\langle 3\cos^2\theta - 1\rangle = 0$. For the inhomoge-

neous[6] CSA, sample rotation at the magic angle will reduce the Hamiltonian to its isotropic components. For an inhomogeneous interaction higher order terms in the *Magnus expansion* [18] of the average Hamiltonian[7] commute with themselves at all times and thus the higher order terms vanish as a consequence. On the other hand, homogeneous interactions, such as a network of dipolar couplings, have non-commuting operators in higher order terms. To first-order the dipolar interaction will be reduced to its isotropic components (i.e. to zero) with sample rotation at the magic angle. However, the presence of higher order terms means that the homogeneous interaction will not be averaged away. The higher order terms go as a power series of the reciprocal of the rotation rate and therefore the effect of the higher order terms can be reduced with increased spinning rate. Strong dipolar couplings (e.g. proton-proton dipolar couplings) may still partially exist even after utilising the fastest MAS rates attainable with modern technology [19]. Additionally, there may be situations where dipolar couplings are undesirable yet fast MAS rates may not be applicable. Therefore, other methods of reducing the effects of dipolar couplings are needed.

[6]For definitions of inhomogeneous and homogeneous interactions used here see Ref. [17].
[7]c.f. Section 1.3.6 for a description of the theory behind the average Hamiltonian.

1.3.5 Heteronuclear Dipolar Decoupling

When observing a system of dilute spins, heteronuclear dipolar couplings of the dilute spins to abundant spins can have a detrimental effect on the recorded signal, for example by broadening the spectral lines of the dilute spins. One method of reducing these heteronuclear couplings is to apply continuous wave (CW) RF irradiation [20] to the abundant nuclear spin at its Larmor frequency whilst observing the dilute spin. The CW RF irradiation induces transitions between the $|\alpha\rangle$ and $|\beta\rangle$ states of the abundant spin. The rate of these transitions is dependent on the amplitude of the RF irradiation. If the rate of these transitions is fast compared to the strength of the coupling then the time-averaged dipolar coupling will be zero to a first-order approximation. CW RF irradiation is usually applied at high power (100-250 kHz) to effectively reduce the heteronuclear dipolar couplings and this continuous high power can cause sample heating and also probe damage if applied for long durations. Other methods of heteronuclear dipolar *decoupling* are therefore needed that are designed using higher-order approximations of the dipolar interaction Hamiltonian and that also minimize the risk of probe damage by giving better results for lower decoupling powers; two-pulse phase-modulated (TPPM) decoupling [21] and X-inverse-X (XiX) decoupling [22] are two such decoupling methods.

M. Ernst published an extensive article that compared the use of different het-

eronuclear decoupling techniques in solid-state NMR under MAS [23]. The problem with combining decoupling techniques and MAS is that at certain ratios of the nutation frequency of the abundant spins due to the decoupling and the MAS frequency interference effects can occur and this can result in a recoupling of the heteronuclear dipolar interaction. This article addressed the issue in depth and made comparisons between no decoupling, CW decoupling, TPPM decoupling and XiX decoupling. The latter two resolution enhancing techniques can reduce spectral linewidths from the order of tens of kilohertz to hundreds of hertz whilst avoiding *rotational resonance conditions* (interference effects).

1.3.6 Proton Homonuclear Dipolar Decoupling

Protons exhibit high sensitivity in NMR studies because they have a large natural isotopic abundance (99.99 %) and a high gyromagnetic ratio. This allows them to be used as superior probe nuclei. Organic molecules contain many protons. Proton NMR is then used to obtain structural and dynamical information about these organic molecules. Quantitative, as well as qualitative, information may be obtained. In the liquid state, proton NMR experiments are commonly used to extract such information. However, solid-state proton NMR studies can be complicated due to large homonuclear dipolar couplings between the protons which cannot be removed by MAS alone. Similar to the situation with heteronu-

clear dipolar couplings, RF irradiation can be used to manipulate the spins in *spin-space* so as to reduce these couplings.

The Lee-Goldburg experiment [24] uses an off-resonance, continuous RF field to induce an effective magnetic field in the rotating frame that is tilted by the magic angle relative to B_0. This can be understood as "MAS in spin-space". As with MAS, the angular factor $(3\cos^2\theta - 1)$ is then equal to zero and the homonuclear dipolar interaction is nullified so long as the precession of the spins is fast relative to the coupling. The drawback with continuous irradiation is that it has to be switched off so that the FID can be acquired. This makes the acquisition of high-resolution one-dimensional spectra difficult. Thus, this technique is usually used to record high-resolution spectra indirectly, in the ω_1 dimension of a two-dimensional experiment. This means that the decoupling can be continuous although experiment times will be large due to the requirement of a two-dimensional dataset.

Waugh et al. introduced a multiple-pulse method for eliminating homonuclear dipolar interactions [25]. This multiple-pulse method uses short pulses and delays to induce rotation and evolution of the nuclear spin polarisations in such a manner that the spin parts of the homonuclear dipolar interaction Hamiltonian, and thus this Hamiltonian as a whole, are averaged to zero at the end of the sequence. In contrast to the Lee-Goldburg experiment, a pulsed method has the advantage

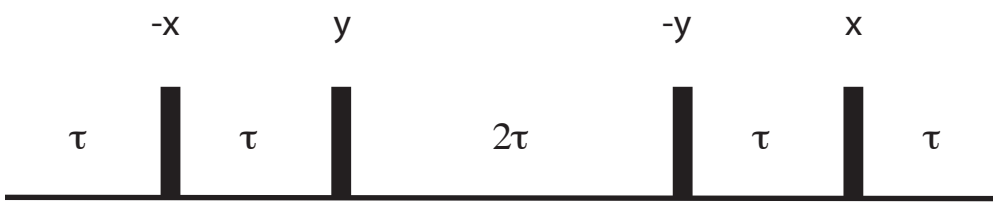

Figure 1.3.7: The WHH-4 pulse sequence. The filled vertical bars represent $\pi/2$ pulses and the letters above the bars indicate the phase of the pulse. τ is a period of delay.

that the FID can be "continuously" observed in the delays between the RF pulses. The earliest homonuclear dipolar decoupling multiple-pulse sequence was labelled WAHUHA (after Waugh, Huber and Haberlen [25]) and later abbreviated to WHH-4. This sequence consists of four $\pi/2$ pulses of different phases, separated by delays (windows) of either τ or 2τ. The WHH-4 pulse sequence is shown in Figure 1.3.7.

To fully understand the WHH-4 multiple-pulse method we need to apply *Average Hamiltonian Theory* (AHT). This theory is based on assuming that some average Hamiltonian ($\bar{\mathcal{H}}$) can be found which describes the overall effect of the multiple-pulse sequence on the spin system. When calculating the density operator from the solution of the Liouville-von Neumann equation for a system that does not have a constant Hamiltonian over time, t, the Hamiltonian has to be piecewise

constant over smaller periods, t_n. This means that

$$\hat{\rho}(t) = \hat{U}(t)\hat{\rho}(0)\hat{U}^{-1}(t) \tag{1.3.22}$$

where $\hat{U}(t) = \exp(-i\hat{\mathcal{H}}_n t_n)\ldots\exp(-i\hat{\mathcal{H}}_1 t_1)$. However, since this system can be described by an average Hamiltonian, then

$$\hat{U}(t) = \exp(-i\hat{\mathcal{H}}_n t_n)\ldots\exp(-i\hat{\mathcal{H}}_1 t_1) = \exp(-i\bar{\mathcal{H}}t) \tag{1.3.23}$$

If this average Hamiltonian is periodic with period (cycle time), t_c, then the Magnus expansion can be used to give

$$\bar{\mathcal{H}}(t_c) = \bar{\mathcal{H}}^{(0)} + \bar{\mathcal{H}}^{(1)} + \bar{\mathcal{H}}^{(2)} + \ldots \tag{1.3.24}$$

where

$$\begin{aligned}
\bar{\mathcal{H}}^{(0)} &= \frac{1}{t_c}\{\hat{\mathcal{H}}_1 t_1 + \hat{\mathcal{H}}_2 t_2 + \ldots \hat{\mathcal{H}}_n t_n\} \\
\bar{\mathcal{H}}^{(1)} &= -\frac{i}{2t_c}\{[\hat{\mathcal{H}}_2 t_2, \hat{\mathcal{H}}_1 t_1] + [\hat{\mathcal{H}}_3 t_3, \hat{\mathcal{H}}_1 t_1] + [\hat{\mathcal{H}}_2 t_2, \hat{\mathcal{H}}_3 t_3] + \ldots\} \\
\bar{\mathcal{H}}^{(2)} &= -\frac{1}{6t_c}\{[\hat{\mathcal{H}}_3 t_3, [\hat{\mathcal{H}}_2 t_2, \hat{\mathcal{H}}_1 t_1]] + [[\hat{\mathcal{H}}_3 t_3, \hat{\mathcal{H}}_2 t_2], \hat{\mathcal{H}}_1 t_1] \\
&\quad + \frac{1}{2}[\hat{\mathcal{H}}_2 t_2, [\hat{\mathcal{H}}_2 t_2, \hat{\mathcal{H}}_1 t_1]] + \frac{1}{2}[[\hat{\mathcal{H}}_2 t_2, \hat{\mathcal{H}}_1 t_1], \hat{\mathcal{H}}_1 t_1] + \ldots\}
\end{aligned} \tag{1.3.25}$$

It can be seen that if the piecewise Hamiltonians ($\hat{\mathcal{H}}_n$) commute then only the

first-order term ($\bar{\mathcal{H}}^{(0)}$) remains. However, if the piecewise Hamiltonians do not commute then it is necessary to transform them into a new frame of reference, called the *toggling frame*, where non-commuting terms disappear, so that the average Hamiltonian can be approximated to first-order.

For the time-dependent Schrödinger equation to be invariant to the frame transformation (c.f. Ref. [26] for the proof) then the Hamiltonian in the toggling frame, $\hat{\mathcal{H}}_{\text{tog}}$, has the form

$$\hat{\mathcal{H}}_{\text{tog}}(t) = \exp(+i\omega_1\hat{I}t)\hat{\mathcal{H}}\exp(-i\omega_1\hat{I}t) - \omega_1\hat{I} \tag{1.3.26}$$

So, for a hard pulse along the x-axis

$$\begin{aligned}\hat{\mathcal{H}}_{\text{tog}}(t) &= \exp(+i\omega_1\hat{I}_x t)\hat{\mathcal{H}}_{x\text{-hardpulse}}\exp(-i\omega_1\hat{I}_x t) - \omega_1\hat{I}_x \\ &= \exp(+i\omega_1\hat{I}_x t)\omega_1\hat{I}_x\exp(-i\omega_1\hat{I}_x t) - \omega_1\hat{I}_x \\ &= \omega_1\hat{I}_x - \omega_1\hat{I}_x = 0\end{aligned} \tag{1.3.27}$$

Therefore, in the toggling frame, it seems as if the RF pulse has no effect.

When using AHT to describe the WHH-4 pulse sequence, a few assumptions need to be made. It is assumed that the RF pulses, which are defined in the rotating frame, are on resonance, are of negligible length and are strong compared to the homonuclear dipolar coupling. This means that the effect of the homonuclear

dipolar coupling during the pulses and the effect of the $\mathbf{B_0}$ field throughout the sequence can be ignored. It will also be assumed that the Hamiltonian for free precession is the Hamiltonian for the homonuclear dipolar coupling

$$\hat{\mathcal{H}}_{\text{free}} = \hat{\mathcal{H}}_D = \frac{1}{2}\frac{\mu_0 \hbar \gamma_1 \gamma_2}{4\pi r^3}(1 - 3cos^2\theta)(3\hat{I}_{1z}\hat{I}_{2z} - \hat{\mathbf{I}}_\mathbf{1} \cdot \hat{\mathbf{I}}_\mathbf{2}) \tag{1.3.28}$$

The WHH-4 sequence begins with a period (τ) where the spin system is allowed to evolve under free procession

$$\hat{\mathcal{H}}_{\text{free}}(0 \rightarrow \tau) = C_{12}(3\hat{I}_{1z}\hat{I}_{2z} - \hat{\mathbf{I}}_\mathbf{1} \cdot \hat{\mathbf{I}}_\mathbf{2}) \equiv \hat{\mathcal{H}}_{zz} \tag{1.3.29}$$

where $C_{12} = \frac{1}{2}\frac{\mu_0 \hbar \gamma_1 \gamma_2}{4\pi r^3}(1 - 3cos^2\theta)$. This Hamiltonian for the first period of evolution will be labelled $\hat{\mathcal{H}}_{zz}$ due to the presence of the $\hat{I}_{1z}\hat{I}_{2z}$ terms. The justification for use of this notation will become apparent.

The next part of the WHH-4 sequence is a $\pi/2$ pulse along $-x$. A frame transformation to the appropriate toggling frame means that the pulse has no effect. There is then another period of free precession. It is required that the Hamiltonian for this period is transformed into the toggling frame. To achieve this, the previous Hamiltonian can be rotated in the rotating frame about $-x$ by $-\pi/2$. The rotation only has an effect on the $\hat{I}_{1z}\hat{I}_{2z}$ terms of the Hamiltonian and transforms them to $\hat{I}_{1y}\hat{I}_{2y}$ terms, with respect to the rotating frame axis. This means

that

$$\hat{\mathcal{H}}_{\text{free}}(\tau \rightarrow 2\tau) = C_{12}(3\hat{I}_{1y}\hat{I}_{2y} - \hat{\mathbf{I}}_{\mathbf{1}} \cdot \hat{\mathbf{I}}_{\mathbf{2}}) \equiv \hat{\mathcal{H}}_{yy} \tag{1.3.30}$$

where the free precession Hamiltonian for this period is viewed in the toggling frame but defined in the rotating frame. This permits ease of summation of operators which are viewed in different toggling frames.

The next pulse is a $\pi/2$ pulse along y. To evaluate the following free precession Hamiltonian, a transformation from the previous Hamiltonian ($\hat{\mathcal{H}}_{yy}$) by a rotation of $-\pi/2$ along the rotating frame y-axis is required. At this instant, the rotating frame y-axis is the toggling frame $-z$-axis, and this is the axis about which the rotation is performed.

$$\hat{\mathcal{H}}_{yy} \xrightarrow{-\pi/2 \text{ rotation along } -z} \hat{\mathcal{H}}_{xx} = \hat{\mathcal{H}}_{\text{free}}(2\tau \rightarrow 4\tau) \tag{1.3.31}$$

This Hamiltonian acts for two τ periods of free precession before an applied $\pi/2$ pulse along the rotating frame $-y$-axis. This corresponds to a rotation of the free precession Hamiltonian about the z-axis of the latest toggling frame:

$$\hat{\mathcal{H}}_{xx} \xrightarrow{-\pi/2 \text{ rotation along } z} \hat{\mathcal{H}}_{yy} = \hat{\mathcal{H}}_{\text{free}}(4\tau \rightarrow 5\tau) \tag{1.3.32}$$

The final pulse, a $\pi/2$ pulse along x, means that it is necessary to rotate the

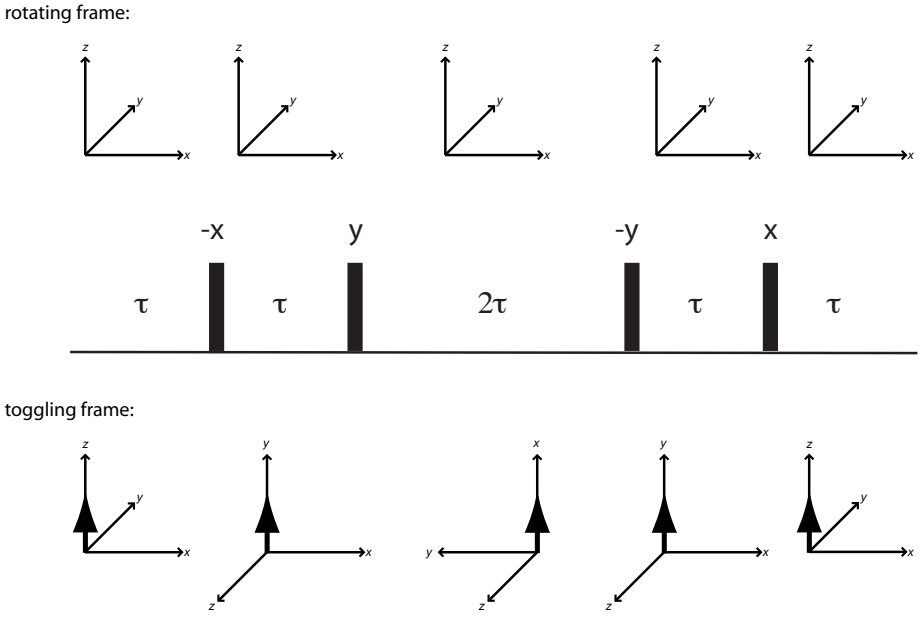

Figure 1.3.8: The WHH-4 pulse sequence and corresponding rotating and toggling frames. The phases of the pulses are indicated with respect to the rotating frame. The large arrow represents the free precession Hamiltonian, which remains untouched in the toggling frame.

Hamiltonian about the toggling frame x-axis by $-\pi/2$ to attain the final state of the free precession Hamiltonian.

$$\hat{\mathcal{H}}_{yy} \xrightarrow{-\pi/2 \text{ rotation along } x} \hat{\mathcal{H}}_{zz} = \hat{\mathcal{H}}_{\text{free}}(5\tau \to 6\tau) \tag{1.3.33}$$

A better understanding of the frame transformations involved is obtained when the transformations are viewed diagrammatically. Figure 1.3.8 illustrates the various toggling frames of the free precession Hamiltonian throughout the WHH-4 sequence.

Combining the free precession Hamiltonians from $t = 0$ to $t = 6\tau$ using equation (1.3.25), the average Hamiltonian can then be given, to first-order, as

$$\bar{\mathcal{H}} = \bar{\mathcal{H}}^{(0)} = \frac{\hat{\mathcal{H}}_{zz}\tau + \hat{\mathcal{H}}_{yy}\tau + \hat{\mathcal{H}}_{xx}2\tau + \hat{\mathcal{H}}_{yy}\tau + \hat{\mathcal{H}}_{zz}\tau}{6\tau} \tag{1.3.34}$$

And because

$$\begin{aligned} &\hat{\mathcal{H}}_{xx} + \hat{\mathcal{H}}_{yy} + \hat{\mathcal{H}}_{zz} \\ &= C_{12}[(3\hat{I}_{1x}\hat{I}_{2x} - \hat{\mathbf{I}}_{\mathbf{1}} \cdot \hat{\mathbf{I}}_{\mathbf{2}}) + (3\hat{I}_{1y}\hat{I}_{2y} - \hat{\mathbf{I}}_{\mathbf{1}} \cdot \hat{\mathbf{I}}_{\mathbf{2}}) + (3\hat{I}_{1z}\hat{I}_{2z} - \hat{\mathbf{I}}_{\mathbf{1}} \cdot \hat{\mathbf{I}}_{\mathbf{2}})] \\ &= 0 \end{aligned} \tag{1.3.35}$$

(since $\hat{\mathbf{I}}_{\mathbf{1}} \cdot \hat{\mathbf{I}}_{\mathbf{2}} = \hat{I}_{1x}\hat{I}_{2x} + \hat{I}_{1y}\hat{I}_{2y} + \hat{I}_{1z}\hat{I}_{2z}$) then the average Hamiltonian for the homonuclear dipolar coupling after one cycle of the WHH-4 sequence is zero. If the cycle is repeated and data points are only collected at the end of the cycle then there will be no contribution from homonuclear dipolar coupling observed in the spectrum. However, this is only the case when the assumptions hold true.

The WHH-4 pulse sequence not only has an effect on the homonuclear dipolar Hamiltonian, it also has a similar effect on the chemical shift Hamiltonian. This is an undesired consequence of attempting to remove the homonuclear dipolar couplings in this fashion. Utilizing the same method as shown above for the homonuclear dipolar Hamiltonian, the WHH-4 sequence induces a first-order av-

erage Hamiltonian for the chemical shift interaction given by

$$\bar{\mathcal{H}}_{CS}^{(0)} = \omega_{CS}\frac{\hat{I}_z\tau + \hat{I}_y\tau + \hat{I}_x 2\tau + \hat{I}_y\tau + \hat{I}_z\tau}{6\tau} = \frac{1}{3}\omega_{CS}(\hat{I}_x + \hat{I}_y + \hat{I}_z) \qquad (1.3.36)$$

Comparing this equation with the chemical shift Hamiltonian given in equation (1.2.12) it can be seen that there is an effective magnetic field, $\mathbf{B_{eff}}$, in the (1,1,1) direction of the rotating frame with length $(1/\sqrt{3})$[8]. Thus, a *scaling factor* has been introduced and the apparent perturbation to the Larmor frequency as a result of chemical shift, ω'_{CS}, is

$$\omega'_{CS} = (1/\sqrt{3})\omega_{CS} \qquad (1.3.37)$$

A spectrum recorded using the WHH-4 pulse sequence will then be scaled compared to one recorded without. The scaling will result in a smaller frequency separation between resonances and thus a greater chance of resonance overlap, especially with broad proton resonances. Therefore, the scaling will affect the resolution of the spectrum. Although spectral resolution is proportional to the scaling factor, the enhancement in resolution owing to the reduction of the homonuclear dipolar couplings under this sequence makes the scaling a worthwhile concession.

There are various other homonuclear dipolar decoupling sequences available. Some of these sequences (MREV-8 [27–29], BR-24 [30], BLEW-12 [31], TREV-

[8] A unit vector in the direction (1,1,1) has length $(1/\sqrt{3})$.

8 [32], MSHOT-3 [33], $R18_2^9$ [34]) build upon the initial work of Waugh et al. and take the approximation of the average Hamiltonian to higher-order terms. Others (FSLG [35, 36], PMLGn [37–39], wPMLGn [40]) are based on the Lee-Goldburg method. These applied RF field techniques are capable of achieving greater homonuclear dipolar decoupling than presently available spinning speeds are able to achieve through MAS. However, residual linewidths associated with heteronuclear dipolar interactions and CSAs are still present. This problem can be overcome by combining coordinated multiple-pulse sequences with MAS. This method is known as *CRAMPS* (combined rotation and multiple-pulse spectroscopy). The combination of multiple-pulse NMR and magic angle spinning was first practiced by Gerstein et al. in 1976 [41].

Proton linewidths can be reduced to less than 1 ppm using CRAMPS [42]. However, given the chemical shift range associated with ^{1}H NMR ($\sim$ 10 ppm) further progress into decoupling techniques is needed to obtain satisfactory resolution. Furthermore, CRAMPS introduces its own problems. MAS creates an additional time dependence of the dipolar Hamiltonian. At slow MAS rates, where the decoupling pulse sequence cycle frequency is fast relative to the sample spinning frequency, interference is minimised. Conversely, the latest achievable MAS rates will have a much larger impact on some decoupling pulse sequences since the cycle times of the pulse sequence and the MAS may be of a similar order and the two cannot be considered as independent. Thus, a homonuclear dipolar decoupling

sequence is needed that performs well at various sample spinning frequencies.

2 Proton NMR Spectroscopy in Solids

2.1 The DUMBO-1 Sequence

CRAMPS, using the DUMBO-1 (Decoupling Under Mind-Boggling Optimization) [42] sequence, is the homonuclear dipolar decoupling technique that is used for high-resolution proton (^{1}H) NMR in this thesis. In the DUMBO-1 sequence the phase of the RF field is continuously modulated whilst the amplitude is kept constant. This sequence was developed by a numerical optimization of the decoupling performance of a RF field with a phase, $\phi(t)$, which is defined as a Fourier series:

$$\begin{aligned} \phi(t) &= \sum_{n=0}^{6}[a_n \cos(2nx_c t) + b_n \sin(2nx_c t)] \qquad \text{if} \quad 0 \leq t < \tau_c/2, \\ \phi(t) &= \pi + \phi(\tau_c - t) \qquad\qquad\qquad\qquad \text{if} \quad \tau_c/2 \leq t < \tau_c \end{aligned} \tag{2.1.1}$$

where $x_c = 2\pi/\tau_c$ and τ_c is the cycle time, equal to a 6π pulse.

The Fourier coefficients a_n and b_n are varied and the decoupling performance of the resulting phase modulation is determined using a computer model of a two-spin system under static conditions. The numerically optimized Fourier coefficients for the DUMBO-1 sequence can be seen in Table 2.1.1. These Fourier coefficients correspond to a RF field with the continuously modulated phase de-

Table 2.1.1: Fourier coefficients for the DUMBO-1 sequence.

n	a_n	b_n
0	+0.1056	0
1	+0.0325	+0.1310
2	+0.0189	+0.1947
3	+0.0238	+0.0194
4	+0.0107	+0.1124
5	+0.0038	-0.0456
6	-0.0013	+0.0869

picted in Figure 2.1.1(a). This phase modulation cannot be implemented experimentally because the electronics need a finite time to switch the phase of a pulse. Therefore, the continuously modulated phase of the DUMBO-1 sequence is split into discrete phases. The minimum duration that each discrete phase can be implemented for depends on the phase-switching time of the hardware. For this reason, combined with the use of 100 kHz of RF irradiation (which results in a 6π pulse, and thus τ_c, of 30 μs) in the numerical optimization, the DUMBO-1 sequence is digitized to 64 discrete phases. The phase modulation scheme of these discrete phases is shown in Figure 2.1.1(b).

As stated earlier, modelling under static conditions only allows for pulse sequence reliability with quasi-static[9] experiments. However, the DUMBO-1 sequence has been shown to produce high resolution spectra at MAS frequencies of up to 65

[9]In this case, quasi-static refers to MAS rates that are slow relative to the sequence cycle frequency.

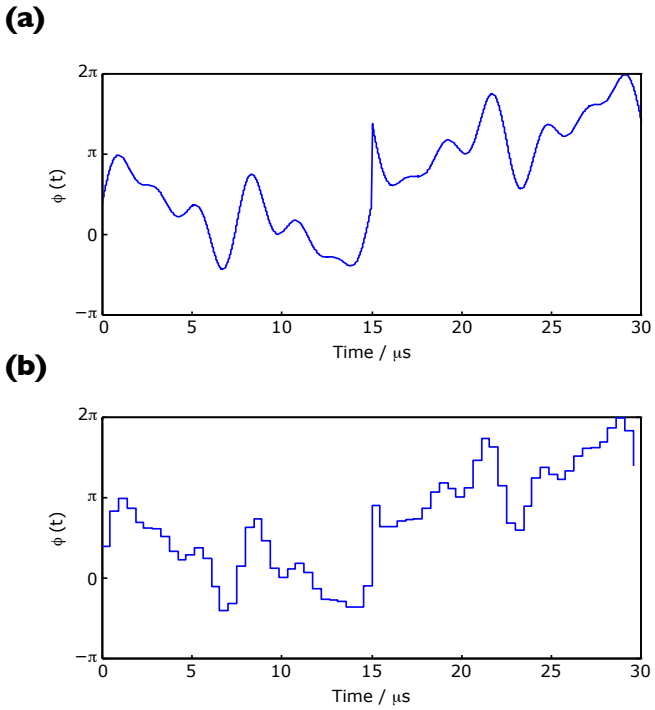

Figure 2.1.1: Illustration of the phase modulation scheme for the DUMBO-1 homonuclear dipolar decoupling pulse sequence (a) and the discrete form which has been divided into 64 segments of equal length (b). One cycle of the periodic modulation is shown.

kHz [43], although there are some rotary resonance conditions where the efficacy of the CRAMPS breaks down. These occur at sequence cycle times (τ_c) that are either half-integer or integer multiples of the MAS cycle time (τ_r), with significant interference observed for the latter [42, 43]. These conditions have also previously been observed for the WHH-4 sequence [44] and the PMLG scheme [38] and are attributed to strong recoupling conditions under these ratios. The inclusion of MAS in computer models of multi-spin systems so as to improve on the performance of the DUMBO-1 sequence has been suggested but attempts to

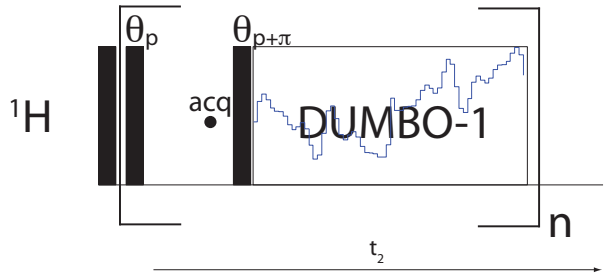

Figure 2.2.1: Pulse sequence used for direct observation of 1D ^{1}H NMR spectra under DUMBO-1 decoupling. Filled vertical bars represent $\pi/2$ pulses unless otherwise stated. The pulses with flip angle θ have phases of p and $p + \pi$, as illustrated.

do so successfully have, thus far, failed [45].

2.2 High-resolution One-dimensional Proton NMR Experiments

The pulse sequence that is used to record one-dimensional ^{1}H NMR spectra under DUMBO-1 decoupling is shown in Figure 2.2.1. This is the *windowed* version of the DUMBO-1 sequence (wDUMBO-1). A time interval is inserted between cycles of the decoupling to allow a data point to be acquired. Like the WHH-4 sequence, one data point is acquired every cycle or integer number of cycles and at this point the homonuclear dipolar couplings are averaged to zero. If many data points are acquired in this manner ($64 \leq n \leq 512$) then a FID can be formed

which yields a high-resolution ^{1}H NMR spectrum.

Note that high-resolution ^{1}H NMR spectra can also be obtained indirectly with the use of a two-dimensional experiment with DUMBO-1 decoupling during t_1. This removes the requirement of an acquisition window. However, no significant enhancement in resolution was observed and the extra time needed to record the data in this manner rendered this experiment unnecessary.

Imperfections in spectrometer hardware mean that the high-resolution ^{1}H NMR experiment has to be empirically optimized to obtain the maximum achievable resolution for the specific hardware. The flip angle θ and the phase p have to be calibrated to ensure maximum resolution and that there are no quadrature images[10] or axial peaks[11] in the resulting spectrum. It has been shown by numerical simulations that large flip angles can have destructive effects on homonuclear decoupled spectra recorded in the direct dimension and that much smaller (or null) flip angles are preferred [46].

It is found that better resolution under DUMBO-1 (and wDUMBO-1) decoupling is obtained slightly off-resonance. This is the case for most multiple-pulse homonuclear dipolar decoupling sequences [42]. Furthermore, as is the case for all multiple-pulse homonuclear dipolar decoupling sequences, and as shown for

[10] Quadrature images are signals that appear as reflections of the true peaks about the centre of the spectrum.

[11] In this instance an axial peak is an artefact observed at zero-frequency offset (i.e. the centre of the spectrum).

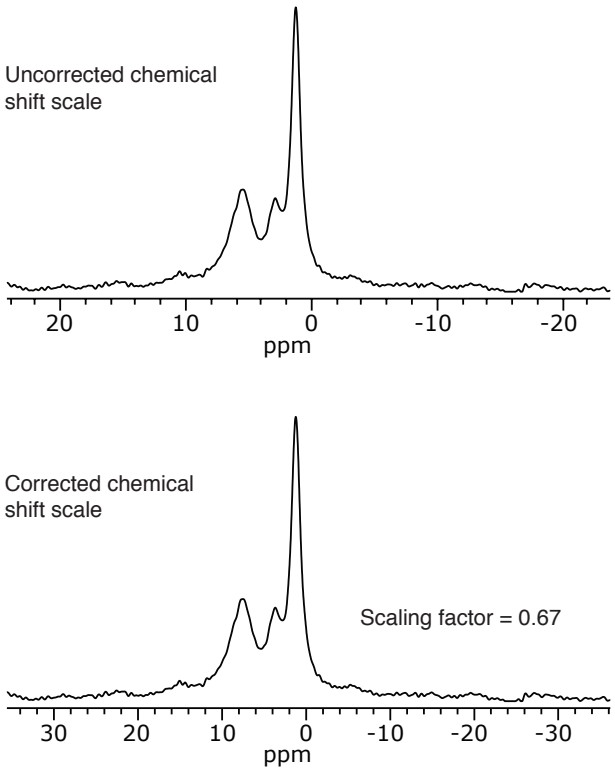

Figure 2.2.2: llustration of the scaling factor associated with wDUMBO-1.

the WHH-4 sequence in section 1.3.6, the DUMBO-1 sequence causes a scaling of the chemical shifts. The calculated scaling factor (λ_{calc}) for the DUMBO-1 sequence is 0.52 [47]. However, the experimental scaling factor (λ_{expt}) may differ from this value. Windowed PMLG sequences have been shown not only to result in a higher λ_{expt} than non-windowed PMLG sequences but also that λ_{expt} may be greater than the theoretical maximum scaling factor for multiple-pulse homonuclear dipolar decoupling sequences which is $1/\sqrt{3}$ [40]. Likewise, the wDUMBO-1 sequence returns a higher λ_{expt} than the non-windowed version [42].

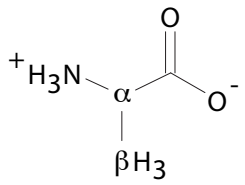

Figure 2.2.3: Structure of alanine. The α and β carbons are indicated.

Figure 2.2.2 shows a ^{1}H NMR spectrum of a solid sample of DL-alanine-2,3-$^{13}C_2$[12] (Figure 2.2.3) with wDUMBO-1 decoupling. The top spectrum shows the chemical shift scale returned from the processing software after the methyl resonance was referenced with a chemical shift of 1.5 ppm. The bottom spectrum shows the *corrected* chemical shift scale. The correction was made after comparison with a ^{1}H MAS NMR spectrum of the same sample under similar conditions. The experimental scaling factor of 0.67 was found from

$$\lambda_{\text{expt}} = \frac{(\delta_{CH}^{w\text{DUMBO-1}} - \delta_{CH_3}^{w\text{DUMBO-1}})}{(\delta_{CH}^{MAS} - \delta_{CH_3}^{MAS})} \tag{2.2.1}$$

The broadening and the chemical shift of the peak corresponding to the NH_3^+ group under CRAMPS are attributed to an interference between the three-site hopping of the protons in the NH_3^+ group and the CRAMPS method [48]. For this reason, the other two proton chemical shift environments of alanine are used to determine the scaling factor. Henceforth, all ^{1}H NMR spectra recorded under

[12]DL-alanine-2,3-$^{13}C_2$ was purchased from *Isotec Inc.* with an isotopic purity of 99 %.

DUMBO-1 (or wDUMBO-1) decoupling will be displayed with corrected chemical shift scales.

The DUMBO-1 sequence shows decoupling robustness to RF inhomogeneity over a range of homonuclear dipolar couplings in simulations [47] and also to variations in B_0 field strength in experiments [42]. This, combined with the good decoupling performance at attainable MAS rates, makes the DUMBO-1 decoupling sequence the optimal sequence to be used for CRAMPS in the experimental setup described below.

2.3 Experimental Setup

All solid-state NMR experiments presented in this thesis were performed on a *Varian Infinity Plus* double-channel spectrometer operating using a wide-bore superconducting magnet with a static magnetic field strength of approximately 7.1 T (which corresponds to a proton Larmor frequency of 300.07 MHz), unless otherwise stated. The spectrometer allows for the manipulation of the length, amplitude, frequency and phase of the RF pulses to a degree that permits the use of the 64 step DUMBO-1 sequence illustrated in Figure 2.1.1(b). Processing of the received FID signal is performed by *Spinsight* software on a *SUN* workstation. The *SUN* workstation also permits the storage of experimental data.

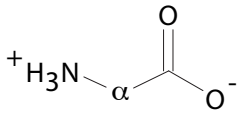

Figure 2.4.1: Structure of glycine. The α carbon is indicated.

2.4 High-resolution One-dimensional Proton NMR Results

Fundamental parameters such as choice of probe and MAS rate were calibrated to give the best possible resolution. It was suggested that the smaller the probe size, the better the RF field homogeneity and, thus, better proton resolution under DUMBO-1 decoupling. However, due to hardware variations, the *Varian* 4 mm triple-resonance MAS probe was found to return higher resolution than the *Varian* 3.2 mm double-resonance MAS probe. Accordingly, the 4 mm probe was used for high-resolution proton studies.

The pulse sequence in Figure 2.2.1 was used to acquire high-resolution one-dimensional ^{1}H NMR spectra of a sample of glycine-2-^{13}C-^{15}N[13] (Figure 2.4.1) at different MAS rates. The variation in wDUMBO-1 performance at these spinning rates is shown in Figure 2.4.2. The acquisition parameters are given in the figure caption. The pulse with flip angle θ, which will be labelled as the *magic*

[13]Universally carbon-13 and nitrogen-15 enriched glycine was purchased from *Sigma-Aldrich* with an isotopic purity of 99.8 % for ^{13}C and 99.2 % for ^{15}N.

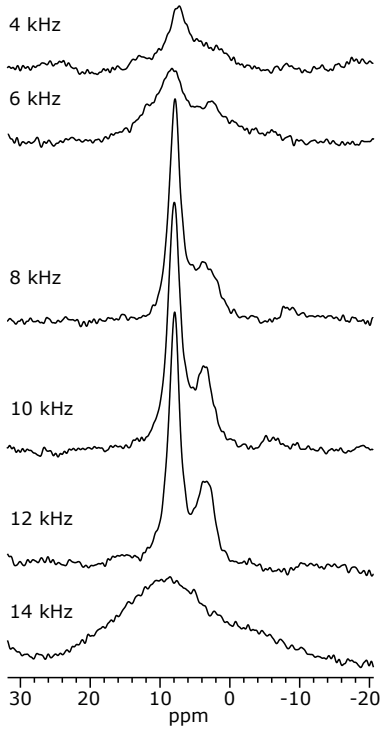

Figure 2.4.2: Variation in wDUMBO-1 performance with MAS rate, tested on a sample of glycine. The experimental parameters were identical for all spectra except for the MAS rate. The spectra were recorded using the pulse sequence in Figure 2.2.1 with an acquisition window of 5.02 μs. The DUMBO-1 cycle time was 30 μs and the ^{1}H frequency was offset to 300.074 MHz. The relaxation delay was 1 s and each experiment took 1 minute to acquire. 50 Hz of Lorentzian line-broadening was used for each spectrum and the number of data points (n) was 256 although the spectra were zero-filled to 8192 points.

angle pulse, was calibrated to have the same amplitude as the $\pi/2$ pulse but a duration of 0.08 μs and a phase, p, of 110°. Also, an additional phase of 110° was added to each of the phases of the DUMBO-1 sequence. This is to ensure that the effective magnetization is in the yz-plane of the rotating frame [42]. Unlike in the literature, where it is recommended that the magic angle pulse duration and phase are calibrated using alternative pulse sequences [42], it was found that these

values were most effectively calibrated for the windowed version of the DUMBO-1 sequence by experimental optimization under the pulse sequence in Figure 2.2.1. This required an incremental modification of the variables with the most suitable values being attained by observation of the resulting spectra.

It can be seen from Figure 2.4.2 that the resolution of the proton spectrum acquired under wDUMBO-1 increases with increasing MAS rate up to 12 kHz, after which the resolution decreases dramatically. This is due to the recoupling conditions associated with a DUMBO-1 sequence cycle time of 30 μs. Therefore, the upper limit of the MAS rate for the 4 mm probe ($\sim$ 15 kHz) could not be used to obtain satisfactory high-resolution ^{1}H NMR spectra. Consequently, a MAS rate of 12 kHz was chosen for all high-resolution proton spectroscopy using the 4 mm probe since it returns the best proton resolution and intensity under the DUMBO-1 sequence.

Figure 2.4.3 can be used to illustrate the effectiveness of CRAMPS. This figure compares the effects of MAS and CRAMPS (using DUMBO-1 decoupling), both with a MAS rate of 12 kHz, on the resolution of ^{1}H NMR spectra of glycine (Figure 2.4.1). It can be seen that the CRAMPS spectrum (black) results in much better resolution than the simple MAS spectrum (blue). In the MAS spectrum none of the glycine resonances can be resolved. However, in the CRAMPS spectrum three resonances can be seen. One for the NH_3^+ group (at higher chemical shift)

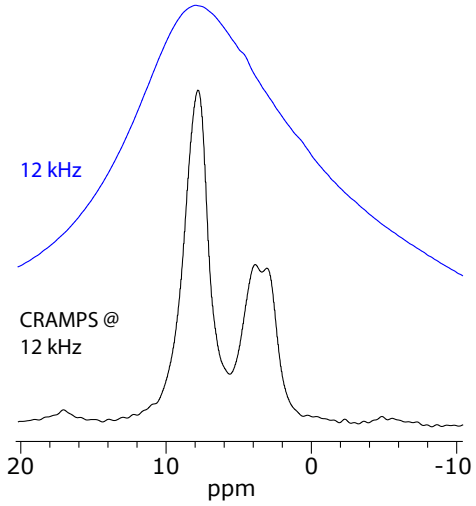

Figure 2.4.3: Illustration of effectiveness of CRAMPS, shown by comparison of MAS (blue) and CRAMPS (black) ^{1}H NMR spectra of glycine. The spectra were recorded with comparable parameters. The MAS spectrum was recorded using a simple $\pi/2$-pulse - acquire experiment and the CRAMPS spectrum was recorded using the same parameters as used to record the spectra of Figure 2.4.2. However, no additional line-broadening was used in the processing of either spectrum.

and two for the CH_2 group (at lower chemical shift).

The solution state ^{1}H spectrum of glycine yields only two resonances; one for the NH_3^+ group and one for the CH_2 group. The two resonances for the CH_2 group observed in the solid state spectrum are due to the diastereotopic nature of the CH_2 protons when in a rigid crystal structure. Although the presence of two resonances for the CH_2 protons in glycine in the solid state is well known, the spectrum helps demonstrate the need for the best possible resolution in solid-state ^{1}H NMR.

Figure 2.4.3 also illustrates a more pertinent point. Extremely similar resolution for ^{1}H NMR spectra of glycine can be obtained by using a combination of high magnetic field strength (11.7 T, corresponding to a ^{1}H Larmor Frequency of 500.17 MHz) and ultra-fast MAS (65 kHz) [43]. To utilise ultra-fast MAS conditions, one must have access to the latest solid-state NMR probe technology. Furthermore, achieving ultra-fast MAS rates requires significantly reduced sample volumes, and thus, significantly reduced sensitivity. This, in turn, demands higher magnetic field strengths to compensate. Ultra-fast MAS rates are not applicable when combining ^{1}H NMR with NMR of nuclei that have low isotopic abundance (e.g. carbon-13 or silicon-29). The tiny sample volume necessitates unrealistic experimental times to achieve adequate signal, even at the highest magnetic field strengths. Additionally, whilst DUMBO-1 decoupling has been shown to be effective at ultra-fast MAS rates, the resolution is not enhanced compared to using DUMBO-1 decoupling at slower rates (but the sensitivity is enhanced) [43].

The information given above suggests that DUMBO-1 decoupling can be used at low field as a practical replacement for 'bigger magnets' and 'faster speeds'. It also suggests that in some cases desired spectra can only be recorded using efficient proton homonuclear dipolar decoupling (such as DUMBO-1) rather than ultra-fast MAS technologies.

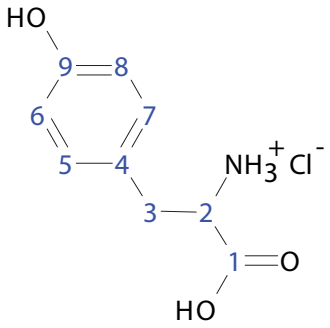

Figure 2.4.4: Structure of tyrosine.HCl. The carbon nuclei have been assigned numbers for ease of reference.

As a comparison, ^{1}H NMR spectra of L-tyrosine hydrochloride (Figure 2.4.4) were recorded at low field with a modest MAS rate and DUMBO-1 decoupling (Figure 2.4.5(a)) and also at high field with ultra-fast MAS and no RF decoupling (Figure 2.4.5(b)). The assignment of the peaks is taken from Refs. [49, 50] and relates to Figure 2.4.4. The asterisks (*) denote quadrature images. It is evident that the resolution of the two spectra is similar. Despite the fact that the linewidths of Figure 2.4.5(a) are larger than those of Figure 2.4.5(b), the resonances can still be resolved, although they may manifest themselves as 'shoulders' on other peaks. This is an interesting achievement since the frequency separation of the resonances is approximately three times smaller in Figure 2.4.5(a) and the MAS rate is almost five times slower.

The high resolution achievable with CRAMPS at low field allows for the quick solution of problems involving protons that would otherwise require more compli-

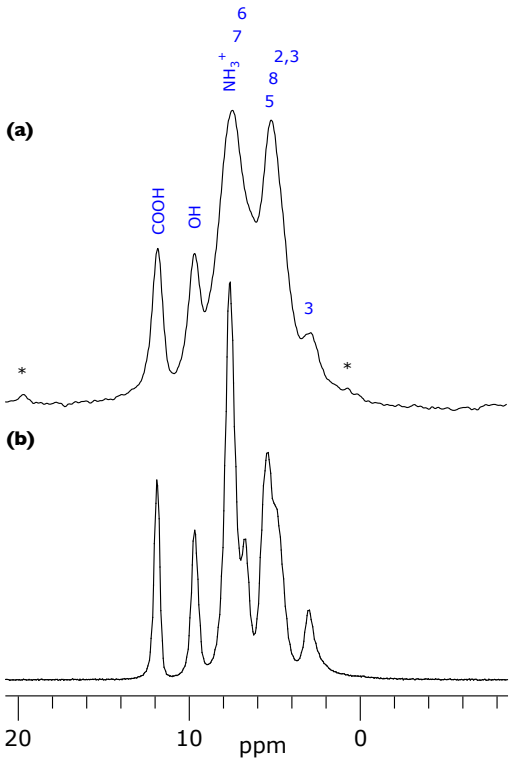

Figure 2.4.5: ^{1}H NMR spectra of L-tyrosine.HCl recorded using a static magnetic field of 7.1 T with a MAS rate of 12 kHz combined with wDUMBO-1 decoupling (a) and using a static magnetic field of 20.1 T with a MAS rate of 55 kHz and no RF decoupling (b). The assignment of the peaks is taken from Refs. [49, 50] and relates to Figure 2.4.4. The asterisks (*) denote quadrature images.

cated methods. Figure 2.4.6 shows two CRAMPS ^{1}H NMR spectra of two types of L-tyrosine hydrochloride. The spectrum in Figure 2.4.6(a) corresponds to L-tyrosine that had been recrystalized after being salted with 1 M hydrochloric acid (HCl) for one hour. The spectrum in Figure 2.4.6(b) corresponds to L-tyrosine that had been recrystalized after being salted with 2 M HCl for twelve hours. The ^{1}H spectra were recorded so that the relative degree to which the L-tyrosine had salted with the HCl could be determined. From the spectra it is obvious that 1

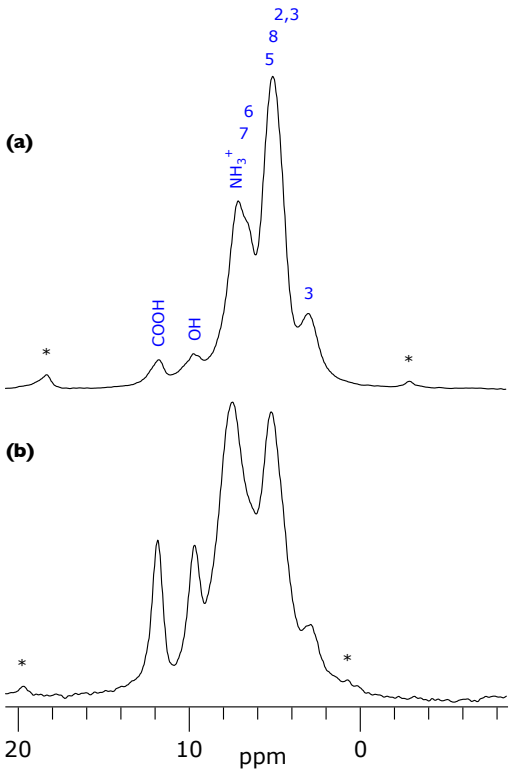

Figure 2.4.6: CRAMPS ^{1}H NMR spectra of two types of L-tyrosine.HCl. The spectra were recorded using the pulse sequence in Figure 2.2.1 with an acquisition window of 5.02 μs. The MAS rate was 12 kHz. The DUMBO-1 cycle time was 30 μs and the ^{1}H frequency was offset to 300.074 MHz. The relaxation delay was 25 s for (a) and 3.5 s for (b). No line-broadening was used for either spectrum and the number of data points (n) was 512 although the spectra were zero-filled to 8192 points. The assignment of the peaks is taken from [49, 50] and relates to Figure 2.4.4. The asterisks (*) denote quadrature images.

M HCl and a one hour duration did not result in significant levels of protonation of the carboxyl group. The extent of protonation gives an indication of how far the salting with HCl has gone. The spectrum in Figure 2.4.6(b) shows a much greater extent of protonation of the carboxyl group and it can be inferred that the salting had gone to completion.

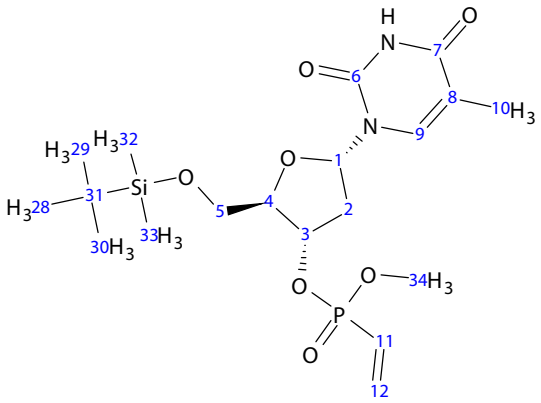

Figure 2.4.7: Structure of **1**: a vinylphosphonate modified nucleotide with a tert-butyldimethylsiloxy (TBS) protecting group. The carbon nuclei have been assigned numbers for ease of reference.

From these spectra it can be concluded that to produce L-tyrosine hydrochloride, 1 M HCl and a one hour salting duration is not sufficient. Without CRAMPS the resolution obtained from a ^{1}H NMR experiment using the experimental setup described in Section 2.3 would not be adequate to determine the extent of protonation because the carboxyl proton resonance would not be resolved. It is worth noting that the CH_2 group (Carbon 3) corresponds to two different proton chemical shifts. This is the same situation as observed for glycine (cf. Figure 2.4.3) where the two resonances arise from two diastereotopic protons.

Another routine that was investigated was the solid-phase synthesis of vinylphosphonate-linked nucleotide dimers. Lera and Hayes [51] use an olefin cross-metathesis reaction [52, 53] to combine a vinylphosphonate modified nucleotide

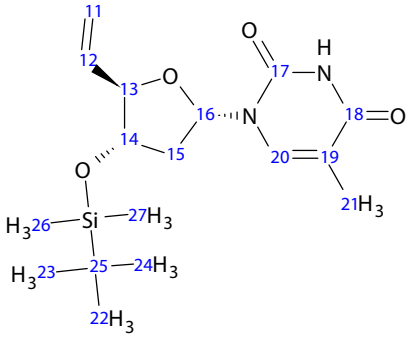

Figure 2.4.8: Structure of **2**: an alkene modified nucleotide with a TBS protecting group. The carbon nuclei have been assigned numbers for ease of reference.

which contains a tert-butyldimethylsiloxy (TBS) protecting group (Figure 2.4.7) with an alkene (Figure 2.4.8) to produce the vinylphosphonate-linked nucleotide dimer with two TBS protecting groups shown in Figure 2.4.9. The vinylphosphonate modified nucleotide with a TBS protecting group will be labelled as **1**, the alkene as **2** and the vinylphosphonate-linked nucleotide dimer with two TBS protecting groups as **3**, for ease of reference. The desired outcome of the investigation is the ability to characterise these nucleotides, whilst attached to a substrate, before and after the solid-phase synthesis.

High-resolution ^{1}H NMR was used to probe the solid reactant, **1**, and the solid product, **3**. Figure 2.4.10 shows ^{1}H NMR CRAMPS spectra of **1** (black) and **3** (blue), both recorded using identical parameters. The CRAMPS utilised DUMBO-1 decoupling and a MAS rate of 12 kHz. It is possible to resolve a large number of proton resonances in the spectrum of **1**. Conversely, in the spectrum of **3** far

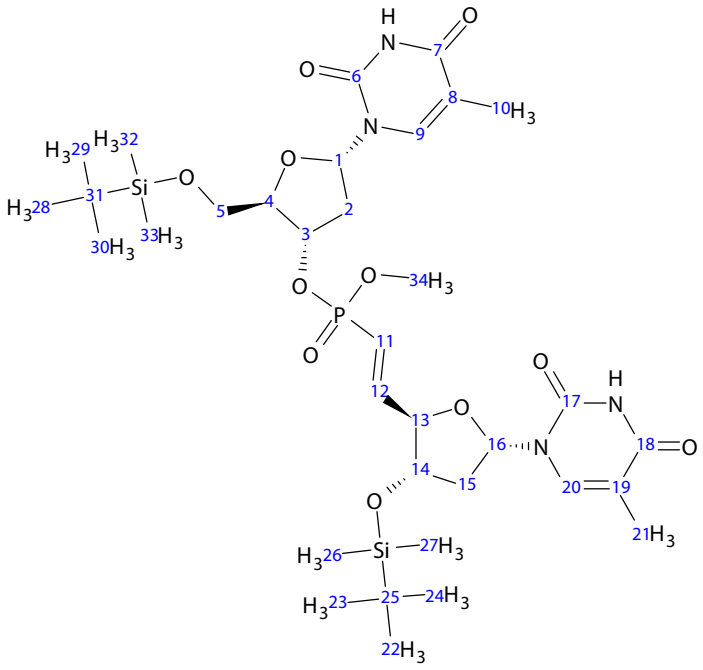

Figure 2.4.9: Structure of **3**: a vinylphosphonate-linked nucleotide dimer with two TBS protecting groups. The carbon nuclei have been assigned numbers for ease of reference.

fewer resonances can be resolved. Nevertheless, the difference in the two spectra does not incontrovertibly indicate a compositional difference in the two samples. It would be difficult to tell from the two spectra which one related to which sample without prior knowledge. Therefore, it can be concluded that high-resolution one-dimensional ^{1}H NMR spectra are not sufficient in determining whether there would be a significant amount of the reactant in the product. Further experiments are required to analyse the sample in more detail.

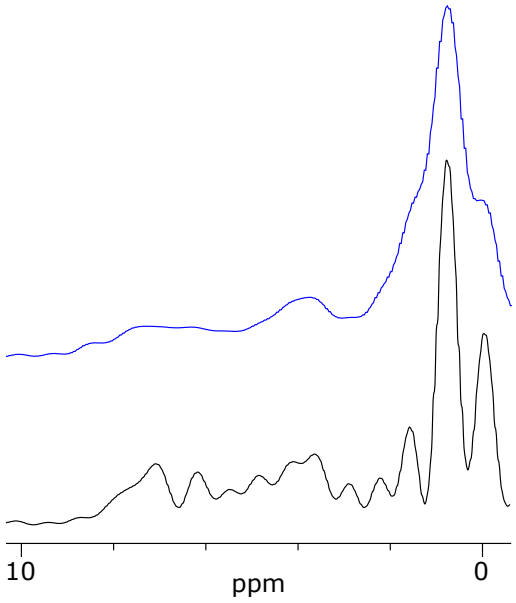

Figure 2.4.10: CRAMPS ^{1}H NMR spectra of **1** (black) and **3** (blue). The spectra were recorded using the pulse sequence in Figure 2.2.1 with an acquisition window of 5.02 μs. The MAS rate was 12 kHz. The DUMBO-1 cycle time was 30 μs and the ^{1}H frequency was offset to 300.074 MHz. The relaxation delay was 1 s and each experiment took 1 minute to acquire. No line-broadening was used for either spectrum and the number of data points (n) was 256 although the spectra were zero-filled to 8192 points.

2.5 High-resolution Two-dimensional Proton NMR Experiments

Compared to one-dimensional NMR, two-dimensional NMR allows for greater spectral resolution by separating the resonances into two-dimensional space. Additionally, two-dimensional NMR can provide structural information that is unattainable by one-dimensional methods.

During a two-dimensional experiment (cf. Section 1.3.2) magnetization can be transferred between spins during the mixing period. A two-dimensional Fourier transform of the recorded signal, $s(t_1, t_2)$, gives a two-dimensional spectrum that is a function of the frequencies of the resonances during the evolution and the detection periods, $s(\omega_1, \omega_2)$. Unlike one-dimensional NMR where the spectrum is plotted as intensity against frequency, in two-dimensional spectra intensity is plotted as a function of two frequencies and usually represented in a contour plot.

Two types of peaks are observed in two-dimensional NMR spectra. These are *cross peaks* and *diagonal peaks*. Cross peaks (where $\omega_1 \neq \omega_2$) arise due to *magnetization transfer* during the mixing period between spins precessing at ω_1 in the first dimension to spins precessing at ω_2 in the second dimension. Diagonal peaks (where $\omega_1 = \omega_2$) arise due to no magnetization transfer between spins during the mixing period. The nature of the mixing period determines the mode of magnetization transfer and, thus, the information contained in the two-dimensional spectrum.

2.5.1 Spin Diffusion CRAMPS

A straight forward two-dimensional experiment uses *spin diffusion* during the mixing period to transfer magnetization and *correlate* spins. In a dipole-coupled nuclear spin system in a solid, a local perturbation of the spin polarization causes

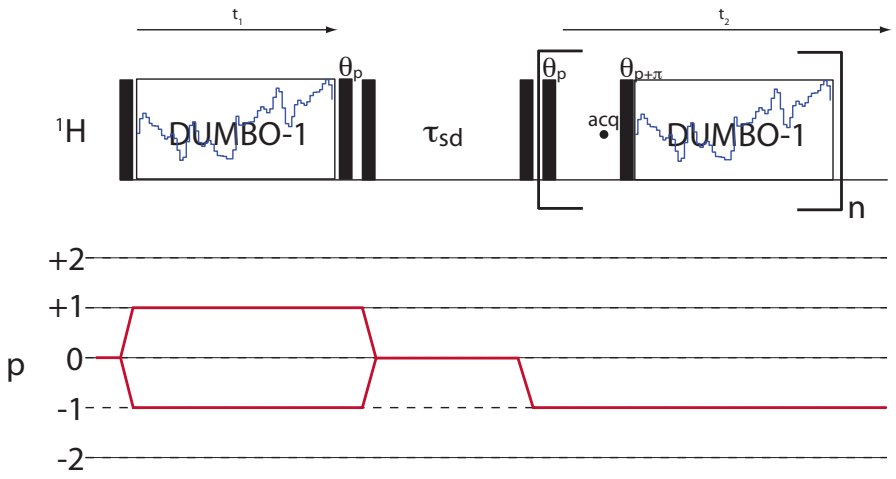

Figure 2.5.1: Pulse sequence used to record 2D ^{1}H -^{1}H spin diffusion correlation NMR spectra under CRAMPS. Filled vertical bars represent $\pi/2$ pulses unless otherwise stated. The pulses with flip angle θ have phases of p and $p + \pi$, as illustrated. τ_{sd} is the mixing period during which spin diffusion occurs.

neighbouring spins to undergo pairwise energy conserving flip-flop processes as the system attempts to redistribute the polarization to an equilibrium state [54]. This process was labelled as spin diffusion by Bloembergen [55]. The kinetics of spin diffusion are dependent on internuclear distances and thus information about the structure of a molecule can be obtained from spin diffusion experiments.

The pulse sequence used for CRAMPS acquisition of high-resolution two-dimensional proton-proton spin diffusion correlation spectra under DUMBO-1 decoupling is given in Figure 2.5.1. This sequence was taken from the literature [45]. The first $\pi/2$ pulse rotates proton magnetization into the xy-plane where it then precesses under DUMBO-1 homonuclear decoupling during t_1. After the t_1 period

the magnetization is returned to the xy-plane by the θ_p pulse before being rotated towards the z-axis by the next $\pi/2$ pulse to facilitate spin diffusion during the mixing time, τ_{sd}. This also acts as a filter, removing unwanted signals from the experiment. The final $\pi/2$ pulse rotates the longitudinal magnetization into the xy-plane ready for direct detection during t_2. This direct detection uses wDUMBO-1 as described earlier (Section 2.2). The resulting spectrum will show diagonal peaks corresponding to the chemical shifts of the spins in the system and cross peaks corresponding to magnetization transfer by spin diffusion between the spins. The duration of the mixing time, τ_{sd}, determines the extent of spin diffusion, i.e. the inter-spin distance over which spin diffusion is able to take place. This then gives an indication of the distances between spins in a molecule.

2.5.2 DQ CRAMPS

Another two-dimensional experiment that uses dipolar couplings to transfer magnetization and correlate spins is the DQ CRAMPS experiment [56]. However, in this experiment dipolar couplings are reintroduced between spins under MAS conditions by a sequence of pulses so that magnetization can be transferred directly rather than by spin diffusion. The pulse sequence used to record DQ CRAMPS proton-proton dipolar correlation spectra under DUMBO-1 decoupling is given in Figure 2.5.2. POST-C7 [57], which is an improved variant of the C7 symmetry

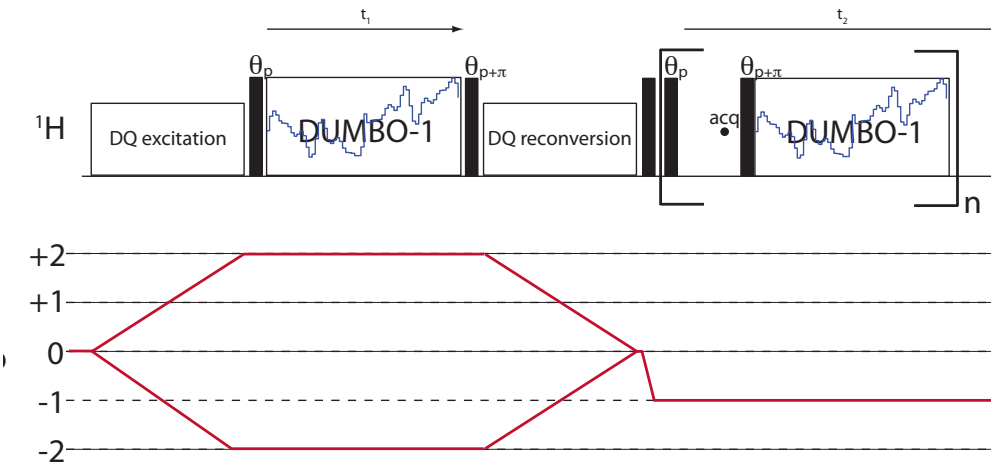

Figure 2.5.2: Pulse sequence for the ^{1}H DQ CRAMPS experiment. Filled vertical bars represent $\pi/2$ pulses unless otherwise stated. The pulses with flip angle θ have phases of p and $p + \pi$, as illustrated. The method of DQ excitation and reconversion is described in the text.

based pulse sequence [58], reintroduces a DQ homonuclear dipolar Hamiltonian between spin-1/2 nuclei in the presence of MAS. This DQ magnetization is rotated into the DUMBO-1 decoupling plane by a θ_p pulse before precessing during t_1 under DUMBO-1 decoupling. A second θ pulse, with an additional π phase shift ($\theta_{p+\pi}$), rotates the magnetization back so that a second block of POST-C7 can be used to reconvert the DQ magnetization to longitudinal magnetization. A $\pi/2$ pulse rotates the longitudinal magnetization into the xy-plane ready for direct detection during t_2. This direct detection uses wDUMBO-1. Cross peaks in the resulting two-dimensional spectrum arise between spins that have a dipolar coupling to one another.

From the CTP under the pulse sequence in Figure 2.5.2 it is observed that only

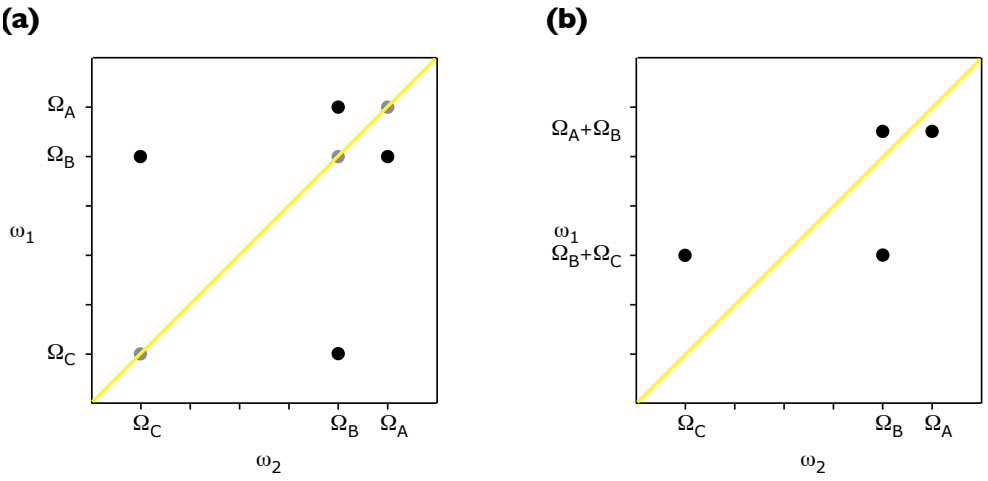

Figure 2.5.3: Schematic of SQ-SQ (a) and DQ-SQ (b) two-dimensional correlation experiment formats. A system of three spins is portrayed. Details of this system are given in the text. Diagonal peaks are represented by filled grey circles and cross peaks are represented by filled black circles. The gradient of the diagonal (yellow) is 1 for the SQ-SQ spectrum and 2 for the DQ-SQ spectrum.

DQ magnetization is allowed to pass, and evolve, during t_1. This indirect detection of DQ magnetization is novel when compared to one-dimensional experiments where only SQ magnetization can be detected. The corresponding spectrum has the standard SQ format in the ω_2 dimension but a DQ format in the ω_1 dimension. There are no diagonal peaks using this DQ-SQ format and the cross peaks for two coupled spins, with offsets Ω_1 and Ω_2, are displayed at $(\Omega_1, (\Omega_1 + \Omega_2))$ and $(\Omega_2, (\Omega_1 + \Omega_2))$. Figure 2.5.3 shows a comparison between two equivalent spectra of a system of three spins, A, B and C which have offsets of Ω_A, Ω_B and Ω_C, respectively. A is coupled to B and B is coupled to C but A is not coupled to C. Figure 2.5.3 illustrates the corresponding two-dimensional SQ-SQ and DQ-SQ

correlation spectra that would result from this system. The DQ-SQ spectrum (b) is plotted with $\omega_1 = 2\omega_2$ for better comparability with the SQ-SQ spectrum (a). All DQ-SQ spectra in this work will be plotted in this manner. Accordingly, the spectrum from a DQ CRAMPS experiment would have similar form to that of Figure 2.5.3(b).

2.6 High-resolution Two-dimensional Proton NMR Results

2.6.1 Spin Diffusion CRAMPS

The efficacy of the proton-proton spin diffusion CRAMPS experiment (Figure 2.5.1) was tested on a model amino acid sample; glycine (Figure 2.4.1). The resulting spectrum is given in Figure 2.6.1. Also shown in the figure (above and to the right of the contour plot) are corresponding high-resolution one-dimensional proton CRAMPS spectra. The two-dimensional spectrum shows the expected correlations when using a mixing time for spin diffusion, τ_{sd}, of 100 μs [59]. Correlations between protons within the CH_2 group are observed, as are correlations between CH_2 and NH_3 protons. Correlations between protons within the NH_3 group may be observed. However, they are indistinguishable from the intense diagonal. Superior resolution is observed in the direct dimension (horizontal

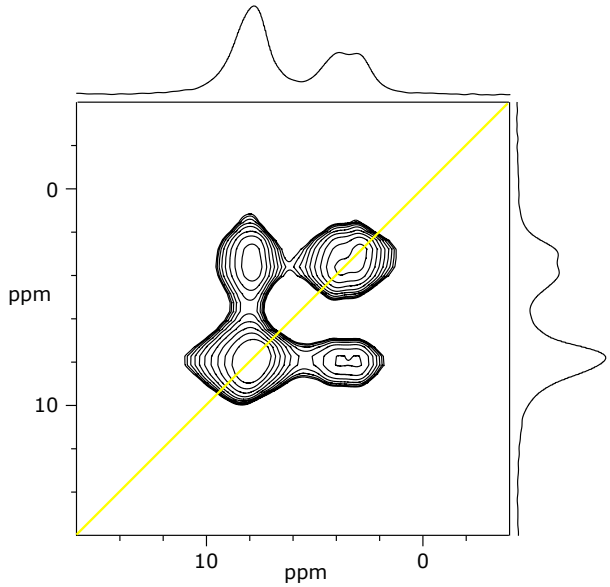

Figure 2.6.1: Two-dimensional ^{1}H-^{1}H spin diffusion CRAMPS correlation spectrum of glycine, recorded using the pulse sequence in Figure 2.5.1. A mixing time for spin diffusion, τ_{sd}, of 100 μs was employed, along with a MAS rate of 12 kHz. 64 scans were recorded for each of 256 t_1 increments with a recycle delay of 1.5 s. A dwell time of 34.8 μs was combined with a direct acquisition time of 17.8 ms in t_2 whilst a dwell time of 30.0 μs was used in t_1 resulting in a total indirect acquisition time of 7.7 ms. Also shown (top and right) are corresponding 1D ^{1}H CRAMPS spectra, given for illustrative purposes.

axis) compared to the indirect dimension (vertical axis). This could be a result of the larger scaling factors associated with direct detection under wDUMBO-1 decoupling (cf. Section 2.2). It could also be due to the ease and certainty of calibration of the homonuclear decoupling in the direct dimension. When the DUMBO-1 parameters are optimized in the direct dimension the results can be directly observed. This is not the case with the indirect dimension where different calibration methods are required (cf. Section 2.4).

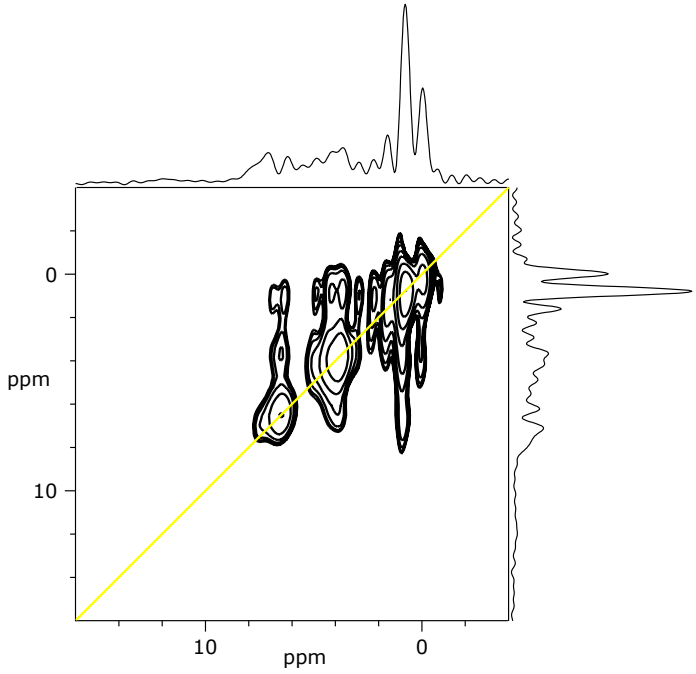

Figure 2.6.2: Two-dimensional ^{1}H-^{1}H spin diffusion CRAMPS correlation spectrum of **1**, recorded using the pulse sequence in Figure 2.5.1. A mixing time for spin diffusion, τ_{sd}, of 300 μs was employed, along with a MAS rate of 12 kHz. 320 scans were recorded for each of 128 t_1 increments with a recycle delay of 1 s. A dwell time of 34.8 μs was combined with a direct acquisition time of 17.8 ms in t_2 whilst a dwell time of 29.5 μs was used in t_1 resulting in a total indirect acquisition time of 3.8 ms. Also shown (top and right) are corresponding 1D ^{1}H CRAMPS spectra, given for illustrative purposes. The 'bumps' in the 1D spectra below $\delta = 0$ ppm are only a result of the lack of truncation of the FID.

The positive result of the spin diffusion experiment on the model sample led to a similar spectrum being recorded for the vinylphosphonate modified nucleotide with a TBS protecting group; sample **1**. This sample was chosen not only because of its relatively high resolution in the one-dimensional proton CRAMPS spectrum (cf. Figure 2.4.10) but because the extra resolution gained by taking the proton spectrum into two dimensions could give insights into the different

proton environments between samples **1** and **3**.

The two-dimensional proton-proton spin diffusion CRAMPS correlation spectrum of sample **1** is shown in Figure 2.6.2. A mixing time for spin diffusion of 300 μs was utilised because sufficient correlations were not observed using only 100 μs (spectrum not shown). The inter-proton distances in glycine are relatively small, even at the furthest separations. Thus, the mixing time does not need to be large for effective transfer of magnetization between the spins. However, inter-proton distances in sample **1** can be much larger, since it is a bigger molecule, and longer mixing times are then required to correlate these protons. The ability to vary the mixing time not only allows the experiment to be selective over the inter-proton distances that will produce correlations, but also permits the estimation of these distances using theoretical models of spin diffusion kinetics [60–63].

In a crowded spectrum, such as for sample **1**, it is difficult to ascertain whether a broad diagonal peak also contains cross peaks using this spin diffusion CRAMPS experiment. Since **3** does not share the relatively high proton resolution of **1**, it was deemed that acquiring a proton-proton spin diffusion correlation spectrum on this sample would result in much poorer resolution close to the diagonal and thus would be of no benefit.

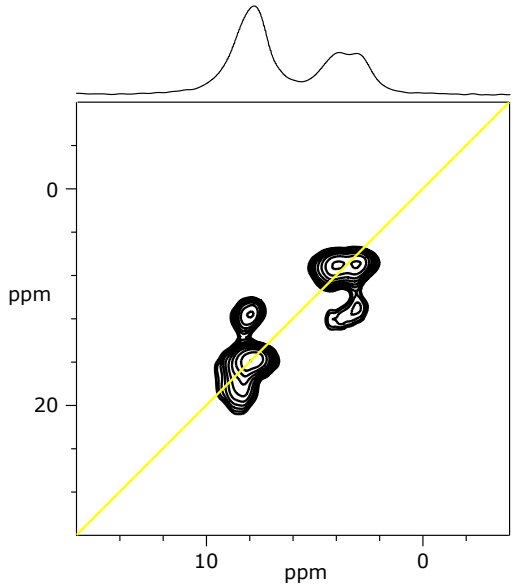

Figure 2.6.3: Two-dimensional ^{1}H-^{1}H DQ CRAMPS correlation spectrum of glycine, recorded using the pulse sequence in Figure 2.5.2. The MAS rate was 12 kHz and 152 scans were recorded for each of 128 t_1 increments with a recycle delay of 1 s being inserted between scans. A dwell time of 35.6 μs was combined with a direct acquisition time of 13.7 ms in t_2 whilst a dwell time of 29.5 μs was used in t_1 resulting in a total indirect acquisition time of 3.8 ms. Also shown (top) is the corresponding 1D ^{1}H CRAMPS spectrum, given for illustrative purposes.

2.6.2 DQ CRAMPS

As previously stated, there are no diagonal peaks with DQ CRAMPS. Consequently, this avoids the problem of differentiating between cross peaks and diagonal peaks. Peaks in a DQ CRAMPS spectrum will be due to a pair of (double-quantum) dipolar coupled spins. Figure 2.6.3 shows the proton-proton DQ CRAMPS spectrum of the glycine test sample, recorded using the pulse sequence in Figure 2.5.2. At proton chemical shift δ values of approximately 8

ppm in the SQ (horizontal) dimension and approximately 16 ppm in the DQ (horizontal) dimension a peak appears that is due to dipolar coupled protons within the NH_3 group. This peak will be labelled as appearing at (8, 16). Using this notation, peaks also appear at (8, 11.5), (4, 12), (3, 11), (4, 7) and (3, 7). The peaks at (4, 7) and (3, 7) are due to dipolar coupled diastereotopic protons within the CH_2 group. The peaks at (4, 12) and (3, 11) correspond to dipolar couplings between these diastereotopic CH_2 protons and the protons in the NH_3 group. These peaks should have their equivalent DQ peaks at (8, 12) and (8, 11), respectively. However, the resolution in the DQ dimension has merged these two peaks into one broad peak, occurring at (8, 11.5) and encompassing (8, 12) and (8, 11).

The same correlations are observed in this DQ CRAMPS experiment as are observed in the corresponding spin diffusion CRAMPS experiment (c.f. Figure 2.6.1). For the spin diffusion CRAMPS experiment cross peaks due to correlations between protons within the NH_3 group appear at the same position as the diagonal peak for this group. Therefore, it is impossible to discriminate between the two and determine for certain that there are correlations between protons in this group. However, the DQ CRAMPS experiment does show for certain that there are these correlations. For these reasons, the DQ CRAMPS experiment is currently the preferred method for analysing proton-proton dipolar correlations in solids.

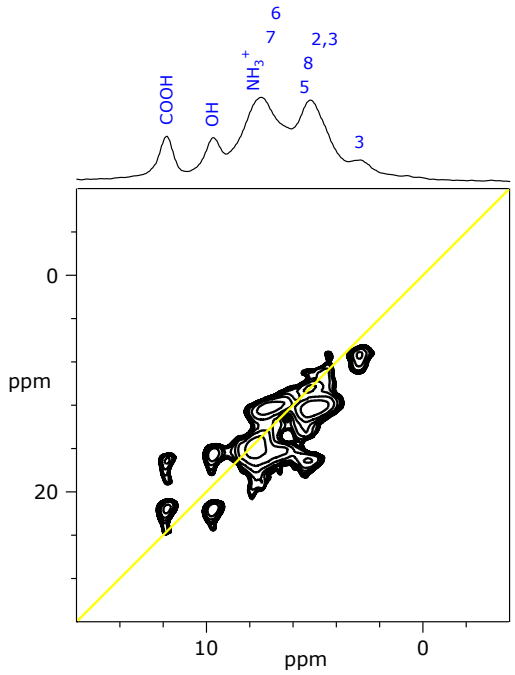

Figure 2.6.4: Two-dimensional ^{1}H-^{1}H DQ CRAMPS correlation spectrum of tyrosine hydrochloride, recorded using the pulse sequence in Figure 2.5.2. The MAS rate was 12 kHz and 216 scans were recorded for each of 256 t_1 increments with a recycle delay of 3.5 s being inserted between scans. A dwell time of 35.8 μs was combined with a direct acquisition time of 18.3 ms in t_2 whilst a dwell time of 30.0 μs was used in t_1 resulting in a total indirect acquisition time of 7.7 ms. Also shown (top) is the corresponding 1D ^{1}H CRAMPS spectrum, given for illustrative purposes.

The sample of tyrosine hydrochloride (Figure 2.4.4) was analysed using the DQ CRAMPS experiment because it gives a good demonstration of the utility of homonuclear proton dipolar couplings when detected through this high-resolution technique. The resulting spectrum is given in Figure 2.6.4. A correlation is observed between the carboxyl proton and the hydroxyl proton (the peaks at approximately (12, 21.7) and (9.7, 21.7)) even though these functional groups are at either end of the molecule. This then gives an indication of intermolecular

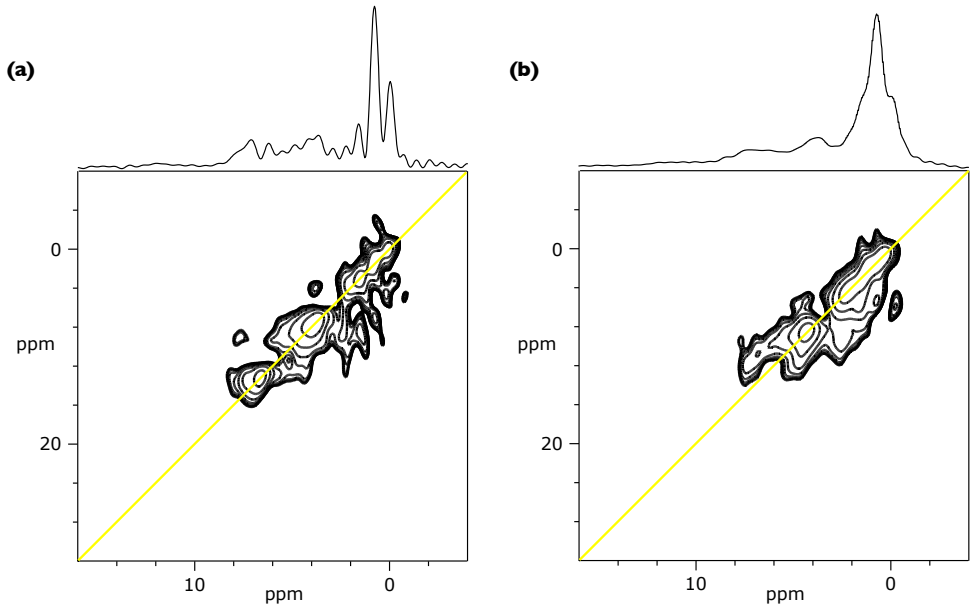

Figure 2.6.5: Two-dimensional ^{1}H-^{1}H DQ CRAMPS correlation spectra of **1** (a) and **3** (b), recorded using the pulse sequence in Figure 2.5.2. The MAS rate was 12 kHz for each and 320 scans were recorded for (a) and 224 scans were recorded for (b) for each of 128 t_1 increments with a recycle delay of 1 s being inserted between scans. A dwell time of 35.8 μs was combined with a direct acquisition time of 9.2 ms in t_2 whilst a dwell time of 30.0 μs was used in t_1 resulting in a total indirect acquisition time of 3.8 ms. Also shown (top) are the corresponding 1D ^{1}H CRAMPS spectra, given for illustrative purposes.

(as well as expected intramolecular) couplings and packing arrangements of the molecules in the solid can be proposed. It is also worth noting that the higher resolution achieved by taking the proton spectrum into a second spatial dimension, combined with the determination of the homonuclear dipolar coupling network, enables the assignment of the resonances in the one-dimensional proton CRAMPS spectrum.

The capability of the DQ CRAMPS experiment in aiding the assignment of proton

resonances has been proven for the sample of tyrosine hydrochloride. However, these proton resonances were previously known [49, 50]. **1** and **3** have proton resonances that have not yet been assigned. Furthermore, different proton-proton correlations for the two samples are expected and therefore the DQ CRAMPS experiment could potentially be used to differentiate between the two samples. Figure 2.6.5(a) shows the DQ CRAMPS spectrum recorded for **1** and Figure 2.6.5(b) shows the DQ CRAMPS spectrum recorded for **3**. It is difficult to ascertain differences between the two spectra at SQ δ values of less than 6 ppm due to the lack of proton resolution observed for **3**. This is the same problem as found for the one-dimensional proton spectra over the entire chemical shift range. However, Figure 2.6.5(a) contains a cross peak at (6.5, 13) that is noticeably absent in Figure 2.6.5(b). This demonstrates that samples **1** and **3** do have a different molecular structure, as expected. Additionally, it also demonstrates that there is not a significant amount, if any, of the reactant (**1**) in the product (**3**).

The peak at (6.5, 13) in Figure 2.6.5(a) is on the diagonal. Accordingly, it is produced by dipolar coupled protons that have the same chemical shift. It is most likely that these protons are in the same environment and bonded to the same carbon atom. A SQ δ value of 6.5 ppm indicates a significant chemical shift. From this evidence only protons on the carbon in position 5 or position 12 (c.f. Figure 2.4.7) could be responsible for the peak at (6.5, 13). Since the peak

is not present in Figure 2.6.5(b), this represents a change of environment of the protons on either carbon 5 or carbon 12 when changing the molecule from **1** to **3**. Exclusively, the protons on carbon 12 change environment and also one proton is removed from carbon 12 when producing **3** from **1** (c.f. Figure 2.4.9). The sole proton remaining on carbon 12 would not produce a peak at (6.5, 13). Thus, **3** differs from **1** by the addition of a new molecule to carbon 12, as expected. Also as expected, this new molecule must have similar proton environments to **1** since there is no clear distinction between the two 2D spectra shown in Figure 2.6.5 except at (6.5, 13).

Despite reaching the conclusion that **1** and **3** are indeed different molecules and that the difference can be elucidated by probing the proton environment of carbon 12 by DQ CRAMPS, an unambiguous assignment of the proton resonances still cannot be made using this technique. Even greater spectral resolution is required.

2.7 Conclusions

The *w*DUMBO-1 proton homonuclear decoupling sequence has been shown to enable the acquisition of high-resolution one-dimensional proton NMR spectra, even at moderate static magnetic field strength and MAS rates. The efficacy of the decoupling is highly MAS rate dependent as well as being RF field dependent. However, it has been shown that *w*DUMBO-1 decoupling can compete with the

latest technological advances in terms of NMR probes capable of ultra-fast MAS rates in combination with ultra-high static magnetic field strengths. The high proton resolution achieved under wDUMBO-1 decoupling has allowed the extent of protonation of L-tyrosine hydrochloride to be determined.

Higher resolution can be gained by the extension of one-dimensional experiments into further dimensions. Two two-dimesional proton-proton correlation experiments have been demonstrated. Spin diffusion CRAMPS and DQ CRAMPS both performed well on a simple model sample of glycine. However, when the more complicated vinylphosphonate modified nucleotide with a TBS protecting group was introduced the DQ CRAMPS experiment proved to be more applicable. This was due to the absence of diagonal peaks in the DQ CRAMPS spectrum which is associated with evolution of DQ magnetization during t_1. Although peaks on the diagonal are observed with DQ CRAMPS, these are cross peaks between protons that share a similar chemical shift.

The DQ CRAMPS experiment resulted in differing spectra for the vinylphosphonate modified nucleotide with a TBS protecting group and the vinylphosphonate-linked nucleotide dimer with two TBS protecting groups. This demonstrates that these two samples are different, which cannot be concluded from one-dimensional spectra alone.

Even with the relatively high resolution achieved using the DUMBO-1 decoupling

sequence, in most solid, proton-containing samples there will be a large amount of spectral overlap of the proton chemical shifts. A method of spreading out the proton chemical shifts over a wider distribution is therefore needed for an enhanced chemical analysis.

3 Heteronuclear Correlation Experiments

To aid the assignment of ambiguous proton resonances in organic molecules, proton-carbon-13 correlation spectra can be used. In the solid state, carbon-13 NMR spectroscopy usually returns peaks of much better resolution when compared to proton NMR spectroscopy, even with state-of-the-art decoupling methods. One reason for this is that the common carbon-13 chemical shift scale range is twenty times that of the proton shift scale (200 ppm compared to 10 ppm). This large range gives a greater separation between resonances in different environments. Thus, when carbon-13 NMR spectroscopy is combined with proton NMR spectroscopy, proton resonances also benefit from this spectral separation.

There are two types of solid-state NMR heteronuclear correlation experiment: dipolar and scalar. Solid-state heteronuclear correlation experiments that utilize dipolar couplings as a mechanism for magnetization transfer include CP, Windowless Isotropic Mixing (WIM) multiple-pulse sequences [64], REDOR-type sequences [65] and symmetry-based sequences [66, 67]. These are much more commonly employed than experiments that utilize scalar couplings. Recently, however, it has been demonstrated that heteronuclear scalar couplings can also be used to facilitate magnetization transfer and obtain a correlation map in solids [49, 68].

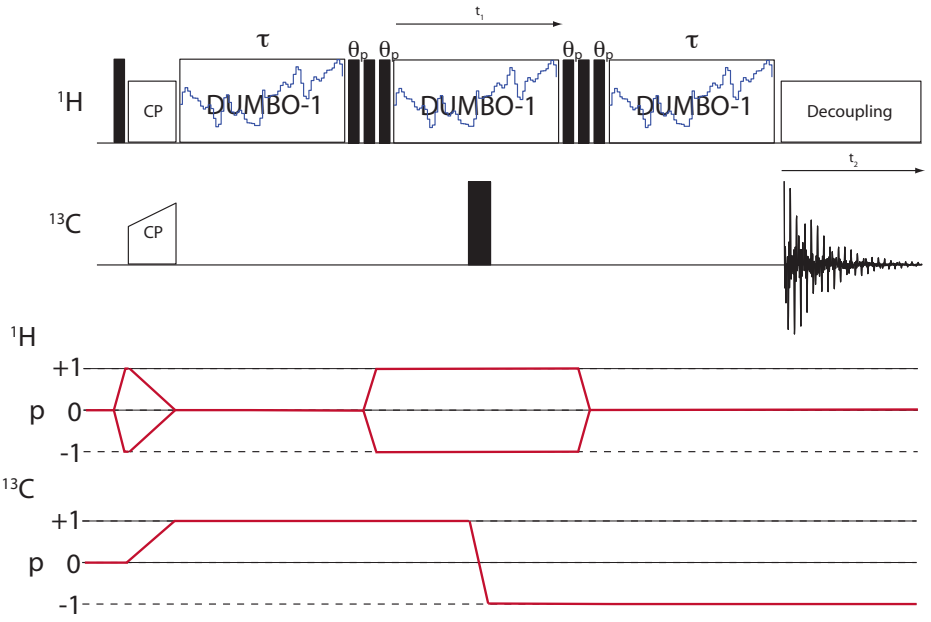

Figure 3.1.1: Pulse sequence used to record MAS-J-HMQC spectra. Narrow and wide filled vertical bars represent $\pi/2$ and π pulses, respectively, unless otherwise stated.

In this chapter the applicability of heteronuclear scalar and also dipolar correlation techniques will be discussed. The latter will then be performed extensively to investigate the inorganic-organic interface for two new types of technologically important nanocomposite particles.

3.1 Heteronuclear Scalar Correlations: MAS-J-HMQC

High-resolution proton-carbon-13 *H*eteronuclear *M*ultiple *Q*uantum *C*orrelations via J-couplings under *MAS* conditions (MAS-J-HMQC) can be explored using the pulse sequence in Figure 3.1.1 [49]. In this pulse sequence carbon-13 (S-spin)

transverse magnetization is created through CP from proton (I-spin) magnetization. The S-spin magnetization evolves during the delay, τ, under the heteronuclear scalar (J_{IS}) coupling Hamiltonian. Proton-S-spin dipolar interactions and also chemical shift anisotropies are averaged by the MAS whereas large proton-proton dipolar couplings are reduced using DUMBO-1 decoupling during this delay. Subsequently, a proton θ_p pulse rotates the proton magnetization from the DUMBO-1 evolution plane onto the z-axis before a proton $\pi/2$ pulse creates heteronuclear MQ coherence from anti-phase ($2\hat{I}_z\hat{S}_y$) coherence that has evolved via the J_{IS} coupling from $\hat{S}_x$. During this section of the experiment the phase cycling selects a mixture of DQ and ZQ heteronuclear coherences. SQ coherences are removed. The second proton θ_p pulse rotates the proton magnetization back into the DUMBO-1 evolution plane so that this magnetization can evolve during t_1 under DUMBO-1 decoupling. The evolution of the S-spin isotropic chemical shift is refocused due to the S-spin π pulse in the centre of the pulse sequence. Therefore, the S-spin chemical shift only appears to evolve during t_2. The combination of θ_p, $\pi/2$ and another θ_p proton pulses have the effect of reconverting heteronuclear MQ (DQ) coherence into anti-phase S-spin coherence before rotating the proton magnetization into the DUMBO-1 evolution plane. The final τ delay allows the anti-phase S-spin magnetization to evolve under the J_{IS} coupling producing observable, in-phase S-spin coherence which then evolves during t_2 under heteronuclear decoupling.

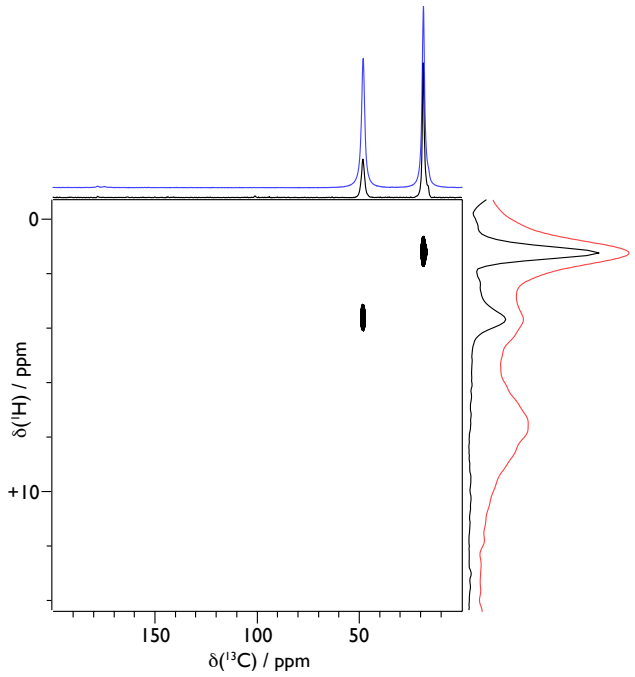

Figure 3.1.2: Two-dimensional ^{1}H-^{13}C MAS-J-HMQC spectrum of DL-alanine-2,3-$^{13}C_2$, recorded using the pulse sequence in Figure 3.1.1. The MAS rate was 12 kHz and 32 scans were recorded for each of 256 t_1 increments with a recycle delay of 1 s being inserted between scans. 100 kHz of CW decoupling was used during t_2. A dwell time of 20.0 μs was combined with a direct acquisition time of 20.48 ms in t_2 whilst a dwell time of 64.0 μs was used in t_1 giving a total indirect acquisition time of 16.4 ms. 50 DUMBO-1 cycles were used in each delay period, resulting in $\tau = 1.5$ ms. Also shown (top and right) are skyline projections of the 2D spectrum in each dimension and corresponding 1D ^{1}H CRAMPS spectrum (red) and 1D ^{13}C CPMAS spectrum (blue), given for illustrative purposes.

The resulting spectrum will contain in-phase peaks corresponding to bonded pairs of heteronuclei. These will appear at the isotropic chemical shift of the I-spin in ω_1 and the isotropic chemical shift of the scalar coupled S-spin in ω_2. Figure 3.1.2 shows an example proton-carbon-13 MAS-J-HMQC spectrum on the model DL-alanine-2,3-$^{13}C_2$ sample. The acquisition parameters are given in the figure caption. High power CW heteronuclear decoupling during t_2 was deemed ade-

quate for high resolution of the carbon-13 resonances. The 1D carbon-13 CPMAS spectrum (blue) was recorded using comparable parameters and the 1D proton CRAMPS spectrum (red) is the scaled spectrum from Figure 2.2.2. It is clear to see from the two correlation peaks that the β carbon is bonded to methyl protons and that the α carbon is bonded to the corresponding CH proton, as expected (c.f. Figure 2.2.3). It is interesting to note from the proton skyline projection (right) that the proton resolution appears much enhanced compared to the 1D proton CRAMPS spectrum. Further enhancement of the proton resolution can be obtained by instead performing a similar MAS-J-HSQC experiment [68]. This experiment transfers magnetization between scalar coupled spins through heteronuclear single quantum coherences. However, greater proton resolution is only returned for samples with high S-spin isotopic abundance using this technique [49].

Since, for the vinylphosphonate modified nucleotide samples (samples **1** (c.f. Figure 2.4.7) and **3** (c.f. Figure 2.4.9)), the S-spin under investigation is carbon-13 at natural abundance, then the MAS-J-HMQC experiment is appropriate to probe proton-carbon-13 heteronuclear scalar correlations. Figure 3.1.3 shows the proton-carbon-13 MAS-J-HMQC spectrum of **1**. The acquisition parameters are given in the figure caption. The 1D carbon-13 CPMAS spectrum (blue) was recorded with a large number of experimental repetitions to achieve a high signal-to-noise ratio whilst XiX decoupling was employed during t_2 for maximum

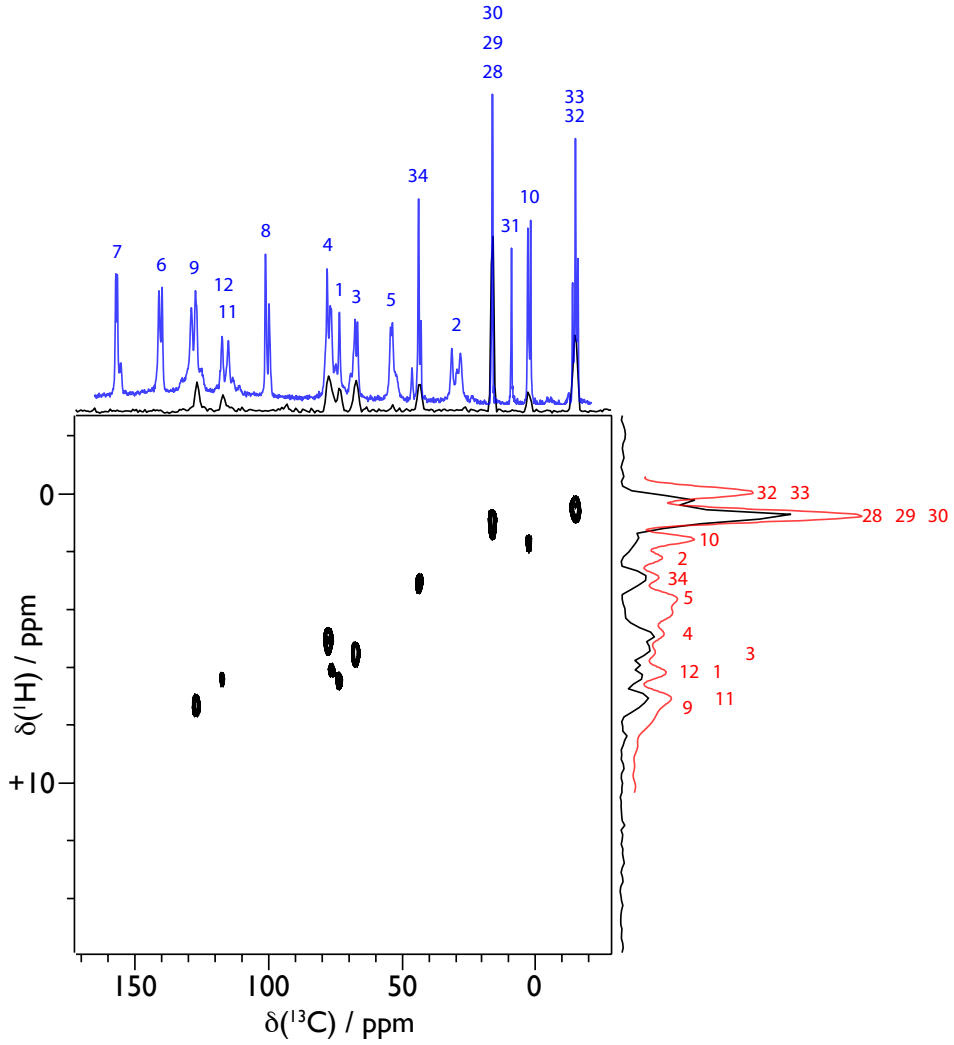

Figure 3.1.3: Two-dimensional ^{1}H-^{13}C MAS-*J*-HMQC spectrum of sample **1** (c.f. Figure 2.4.7). The spectrum was recorded using the pulse sequence in Figure 3.1.1. The MAS rate was 12 kHz and 368 scans were recorded for each of 256 t_1 increments with a recycle delay of 1 s being inserted between scans. 100 kHz of CW decoupling was used during t_2. A dwell time of 20.0 μs was combined with a direct acquisition time of 20.48 ms in t_2 whilst a dwell time of 64.0 μs was used in t_1 giving a total indirect acquisition time of 16.4 ms. 50 DUMBO-1 cycles were used in each delay period, resulting in $\tau = 1.5$ ms. Also shown (top and right) are skyline projections of the 2D spectrum in each dimension and corresponding 1D ^{1}H CRAMPS spectrum (red) and 1D ^{13}C CPMAS spectrum (blue), given for illustrative purposes.

resolution of the carbon-13 resonances. In this high-resolution CPMAS spectrum a large number of the carbon-13 resonances appear to be split into two peaks. This is due to the presence of two enantiomers of **1** in the unit cell of the crystal lattice. The 1D proton CRAMPS spectrum (red) is taken from Figure 2.4.10. The differences between the skyline projections (top and right) and the one-dimensional spectra give a first indication of the assignment of the resonances. The absence of peaks in the skyline projection of the carbon-13 dimension (top) where there are peaks in the corresponding CPMAS spectrum (blue) signifies carbon atoms that are not directly bonded to a proton. Similarly, the absence of peaks in the skyline projection of the proton dimension (right) where there are peaks in the corresponding CRAMPS spectrum (red) signifies protons that are not directly bonded to a carbon atom. Using this spectrum in combination with the corresponding ^{1}H-^{1}H DQ-CRAMPS spectrum (Figure 2.6.5(a)) an assignment of the proton resonances can be made. This assignment is given in the figure.

Since an assignment of the proton resonances from sample **1** has been made, there is no requirement to perform the same experiment on sample **3**. It has been clarified that the peak at $\delta(^{1}\mathrm{H}) = 6.5$ ppm is due to the resonating protons attached to carbon 12 in sample **1**. Thus, this is the resonance that distinguishes between **1** and **3**. Henceforth, a MAS-*J*-HMQC is not required and performing a ^{1}H-^{1}H DQ-CRAMPS experiment will suffice for these samples. This experiment is preferred over the MAS-*J*-HMQC experiment if the same conclusions can be

drawn because it can be recorded in less time. The MAS-J-HMQC experiment requires more experimental repetitions due to the low natural isotopic abundance of carbon-13 nuclei and the relaxation that occurs during the relatively long τ delay periods. Furthermore, when investigating these nucleotides before and after the solid-phase synthesis without removing them from a substrate, a NMR experiment that utilizes a probe nucleus with a large gyromagnetic ratio and large natural isotopic abundance is of paramount importance. This is due to the relatively small amount of nucleotide compared to substrate.

It has been shown that heteronuclear scalar correlations can be used to assign resonances and aid in structure determination. Complementary heteronuclear dipolar correlations can be used to discern between nuclei that are close spatially and nuclei that share a chemical bond. This can give critical additional structural information when attempting to fully characterise a system. Furthermore, in situations where signal-to-noise is the limiting factor, it may be necessary to perform heteronuclear dipolar correlation experiments rather than heteronuclear scalar correlation experiments. Dipolar couplings are, in general, much larger than scalar couplings in solid samples. For example, the dipolar coupling between the α and β carbons in L-alanine (c.f. Figure 2.2.3) has a magnitude of 2105 Hz whereas the scalar coupling between these two carbons is only 34 Hz [69]. Since the rate of transfer of magnetization between two spins is dependent on the reciprocal of the coupling, the transfer maximum is achieved much faster under

dipolar transfer. This means that, for most solid samples, greater signal-to-noise is returned with heteronuclear dipolar correlation experiments because shorter periods of magnetization transfer are required which negates the large intensity losses caused by the rapid decay of magnetization in solids.

3.2 Heteronuclear Dipolar Correlations: DUMBO-LGCP

3.2.1 Previous Studies on Nanocomposite Particles

Inorganic-organic nanocomposite particles are technologically important materials with possible applications as catalysts [70], electronic or photonic devices [71] and scratch-resistant, fire retardant coatings [72]. Previously, Agarwal and co-workers used heteronuclear dipolar correlations to characterise the interface in systems of this type [73]. A poly(4-vinyl pyridine) (P4VP)/silica nanocomposite was prepared using an aqueous silica sol (*Nyacol 2040*[14]). Figure 3.2.1 shows a schematic diagram of this preparation where 4-vinyl pyridine is polymerised in the presence of the silica sol and an ammonium persulfate initiator to form nanocomposite particles with a "currant-bun" morphology. Also shown in the diagram are an illustration of the hypothesized interacting interface (the surface of the silica sol and the P4VP) and an illustration of the currant-bun morphology,

[14] *Nyacol 2040*, a 20 nm aqueous silica sol, supplied as a 40 w/v % solution by Eka Chemicals, Bohus, Sweden.

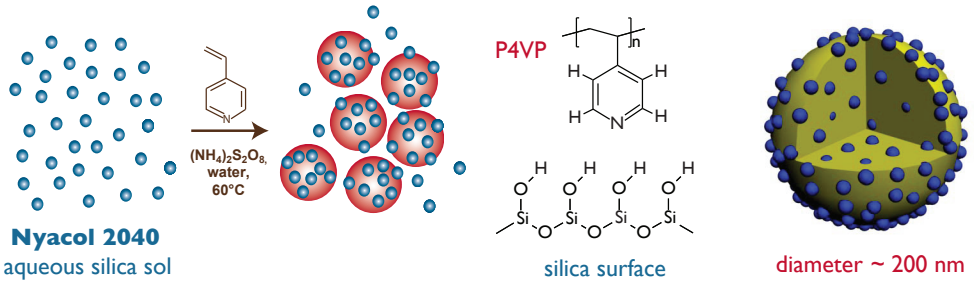

Figure 3.2.1: Schematic representation of the preparation of the colloidal nanocomposite particles by the *in situ* homopolymerization of 4-vinyl pyridine in the presence of an aqueous silica sol.

with the yellow being the polymer latex and the blue balls being the silica sol embedded within and around it. The P4VP/silica nanocomposite particles had a mean diameter of approximately 200 nm. The mean particle diameter was determined separately by Disk Centrifuge Photosedimentometry (DCP) and Dynamic Light Scattering (DLS) techniques.

Agarwal and co. [73] used the pulse sequence given in Figure 3.2.2 to extract information on the heteronuclear dipolar couplings between interfacial protons and silicon-29 nuclei. Figure 3.2.3 shows the resulting spectra from performing this pulse sequence on dried pristine *Nyacol 2040* silica sol (a) and the P4VP/silica nanocomposite (b). The signals in the silicon-29 dimension at δ = -111 and -100 ppm correspond to Q^4 and Q^3 silicon environments, respectively. These are quaternary silicon atoms co-ordinated by four bridging oxygen bonds where the superscript indicates the number of such bridges which link to other silicon atoms.

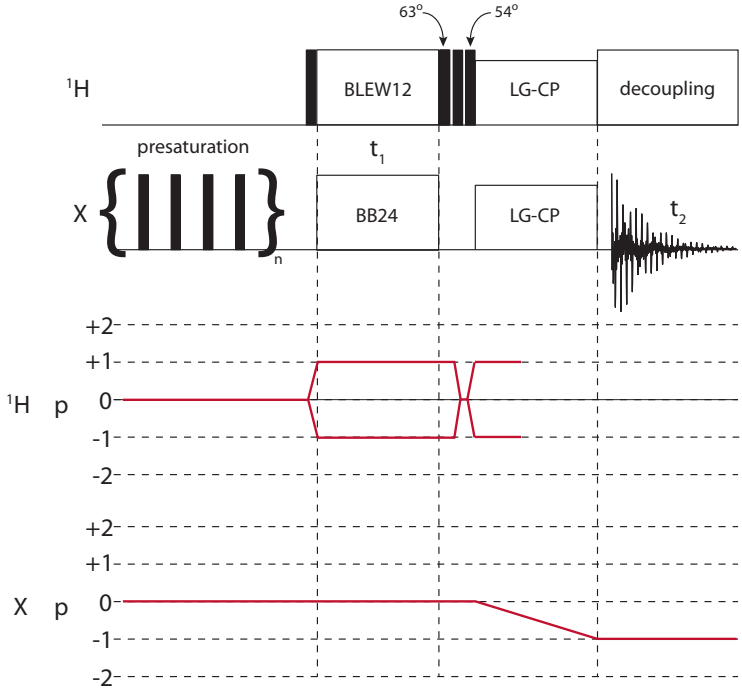

Figure 3.2.2: Pulse sequence used to record two-dimensional BLEW12-LGCP heteronuclear dipolar correlation spectra. Filled vertical bars represent $\pi/2$ pulses unless otherwise stated.

Therefore, the line at δ = -111 ppm results from silicon located in the bulk of the sol and the resonance at δ = -100 ppm can be assigned exclusively to silicon atoms in silanol groups on the surface. The signals in the proton dimension of (a) can be assigned to silanol protons since these are the only protons present in the silica sol. However, the signals in the proton dimension of (b) can be assigned to protons from either the silanol groups or the polymer. It can be seen that some of the protons that correlate to the Q^3 silicon environment come from the aromatic part of the polymer since they have a greater chemical shift than silanol protons. Therefore, the polymer is in close proximity to the silica surface. Furthermore,

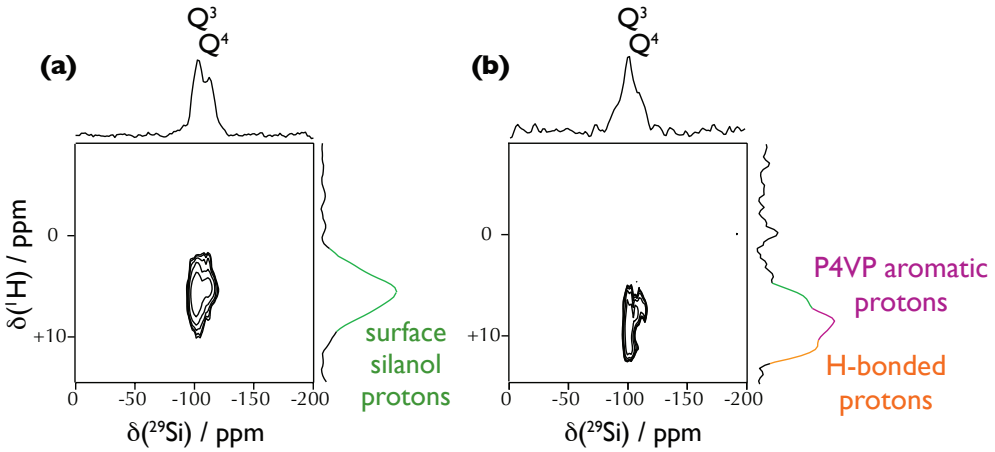

Figure 3.2.3: Proton-silicon-29 dipolar correlation spectra of dried pristine *Nyacol 2040* silica sol (a) and P4VP/silica nanocomposite (b), recorded using the pulse sequence given in Figure 3.2.2. Skyline projections of the two-dimensional spectra parallel to the silicon-29 (top) and proton (right) frequency dimensions are also shown.

a proton chemical shift of greater than 10 ppm is observed which indicates some involvement in hydrogen bonding. It was concluded that the interaction between the polymer and the silica surface occurs via hydrogen bond formation between the pyridine nitrogen and a silanol hydroxyl proton. This interaction is illustrated in Figure 3.2.4.

Agarwal and co. also studied a polystyrene (PS)/silica nanocomposite prepared using an alcoholic silica sol [73]. No evidence for hydrogen bonding was observed in this system. A π-interaction between the aromatic ring of the PS and the surface of the silica sol was postulated as the interaction between the two interfaces.

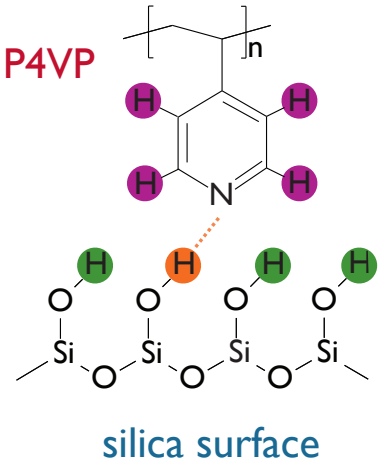

Figure 3.2.4: Illustration of the mode of hydrogen bonding within the interfacial region in the nanocomposite system.

3.2.2 Next-Generation Nanocomposite Particles 1

Aqueous silica sols with fully hydroxylated surfaces are ubiquitous in the formation of organic-inorganic nanocomposite particles [74, 75]. However, surface modification by a condensation reaction between the surface silanol groups and trialkyloxysilane reagents results in aqueous silica sols with enhanced colloidal stability. For example, an ultrafine aqueous sol functionalized with glycerol by reaction with prehydrolyzed γ-glycidoxypropyltrimethoxysilane is marketed commercially as *Bindzil CC40* [76]. This material contains 1 - 2 attached glycerol groups per nm^2 of silica surface, corresponding to 800 glycerol groups per silica particle.

Recently, Armes and co. have synthesized new polymer/silica colloidal nanocom-

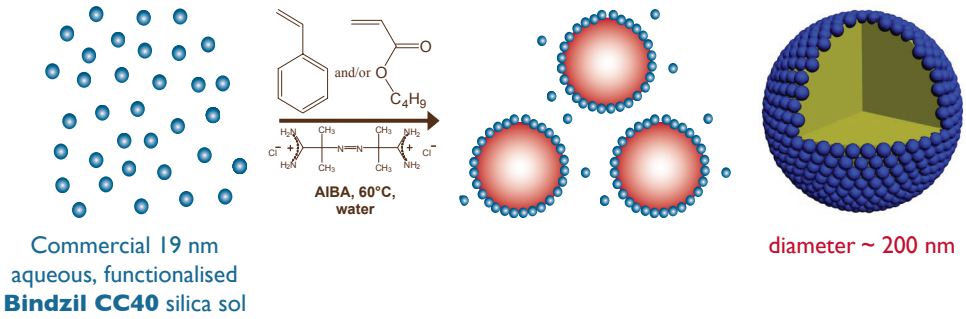

Figure 3.2.5: Schematic representation of the synthesis of colloidal nanocomposite particles by *in situ* aqueous (co)polymerization of styrene and/or n-butyl acrylate in the presence of a *Bindzil CC40* glycerol-functionalized silica sol.

posite particles using such a glycerol-functionalized sol [77]. Figure 3.2.5 shows a schematic diagram of this synthesis. PS/silica nanocomposites with mean particle diameters (measured by DLS) between 280 and 410 nm containing up to 28 wt % silica were prepared by *in situ* aqueous polymerization using a cationic azo initiator (2,2'-azobis(isobutyramidine) dihydrochloride (AIBA)) [78]. Copolymerization with n-butyl acrylate resulted in materials with mean particle diameters between 200 and 250 nm which contained up to 43 wt % silica and formed high-quality transparent films at ambient temperature [79]. Optimization of the initial silica sol concentration gave silica aggregation efficiencies in excess of 95 %, indicating minimal contamination with excess non-aggregated sol. Well-defined "core-shell" morphologies with a monolayer of silica particles surrounding the polymer core were observed using electron spectroscopy imaging / transmission electron microscopy (ESI/TEM). Control syntheses with unmodified aqueous silica sols were not successful, suggesting that surface functionalization is essen-

tial for the production of these colloidal nanocomposite particles. In addition, a combination of X-ray photoelectron spectroscopy (XPS) and differential scanning calorimetry (DSC) suggested that, for the poly(styrene-co-n-butyl acrylate)/silica nanocomposites, the n-butyl acrylate residues interact more strongly with the silica surface than their styrene counterparts [79]. These observations raise interesting questions about the nature of the interface between the organic and inorganic components of colloidal nanocomposite particles prepared by *in situ* polymerization from these aqueous glycerol-functionalized silica sols. Functionalization might promote a new specific polymer-silica interaction, such as hydrogen bond formation between the ester carbonyl in the n-butyl acrylate residue and a glycerol group on the modified surface. On the other hand, given the aqueous synthesis conditions, non-specific hydrophobic interactions between the polymer chains and the functionalized surface might play a role in interfacial adhesion.

As shown by Agarwal and co. [73], solid-state NMR is a good probe of the interface of these types of particles. However, the particles studied in that work have a currant-bun morphology which optimizes the sensitivity of solid-state NMR experiments by maximizing the interfacial area between the organic and inorganic phases. The next-generation nanocomposites described above are more challenging because of the greater complexity of the glycerol-functionalized surface and because of their core-shell morphology. Nanocomposite samples with small mean diameters were selected for solid-state NMR measurements in order to maximize

Table 3.2.1: Silica content and particle size for the *Bindzil CC40* glycerol-functionalized silica sol and the three polymer/silica nanocomposites prepared using it. *a*. Determined by thermogravimetric analysis. *b*. Intensity-average particle diameter measured by DLS. *c*. Weight-average particle diameter measured by DCP. *d*. Number-average particle diameter determined from TEM.

		Particle Diameter (D) / nm		
Sample	Silica Content[a] / wt %	D[b]	D[c]	D[d]
Bindzil CC40 silica sol	100	21	-	19 ± 4
P(n-BuA)/silica	43	169	-	-
PS/silica	26	208	164 ± 29	154 ± 30
60:40 P(S-co-n-BuA)/silica	37	206	163 ± 28	167 ± 19

the interfacial area between polymer and silica components. This results in optimal sensitivity for proton-silicon-29 correlation spectra. Table 3.2.1 shows the silica content and mean diameter for the selected colloidal nanocomposites, as well as the *Bindzil CC40* silica sol. Typical electron micrographs for PS/silica and P(S-co-n-BuA)/silica nanocomposite particles are given in Figure 3.2.6. In each case the nanocomposite particles have relatively narrow size distributions and surfaces composed of silica particles.

Figure 3.2.7(a) shows the silicon-29 CPMAS spectrum of the *Bindzil CC40* glycerol-functionalized silica sol recorded with a contact time of 3 ms. Assignment of the observed resonances to the silicon sites depicted in Figure 3.2.7(b) is facilitated by comparison with the silicon-29 shifts measured for both substituted methyl silanes [80] and other surface-modified colloidal silica systems [81]. Similar to the samples studied by Agarwal and co. [73], the relatively intense signals at δ = -111

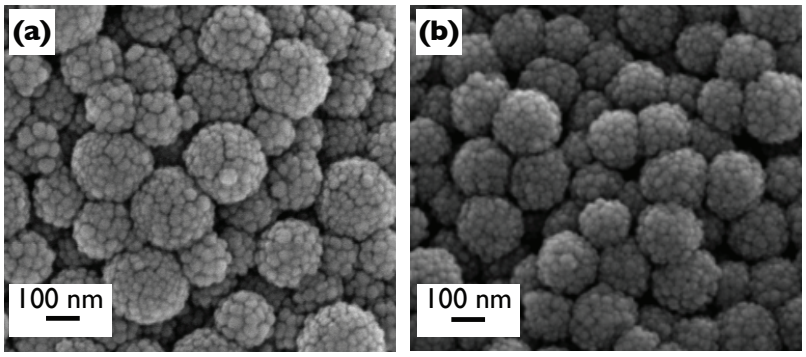

Figure 3.2.6: Scanning electron micrographs of (a) PS/silica and (b) P(S-co-n-BuA)/silica nanocomposite particles.

and -100 ppm correspond to Q^4 and Q^3 silicon environments, respectively. The resonance at δ = -111 ppm results primarily from silicon located in the bulk, as well as a contribution from sites on the silica particle surface where the glycerol-functional silane is attached. The resonance at δ = -100 ppm can be assigned exclusively to silicon atoms in silanol groups on the surface, while a low intensity unresolved shoulder at approximately δ = -92 ppm represents a small fraction of bridging Q^2 silicon atoms. In contrast, the weaker signals at δ = -65 and -56 ppm correspond to T^3 and T^2 silicon environments, respectively. These are tri-substituted silicon environments which are co-ordinated by three bridging oxygen bonds and a single bond to carbon, and therefore they result from the silicon site in the glycerol-functional silane. The line positions suggest that both T^2 and T^3 environments are present, indicating that each silane is attached via bridging oxygen bonds to either two or three silicon atoms. Assuming there is no self-

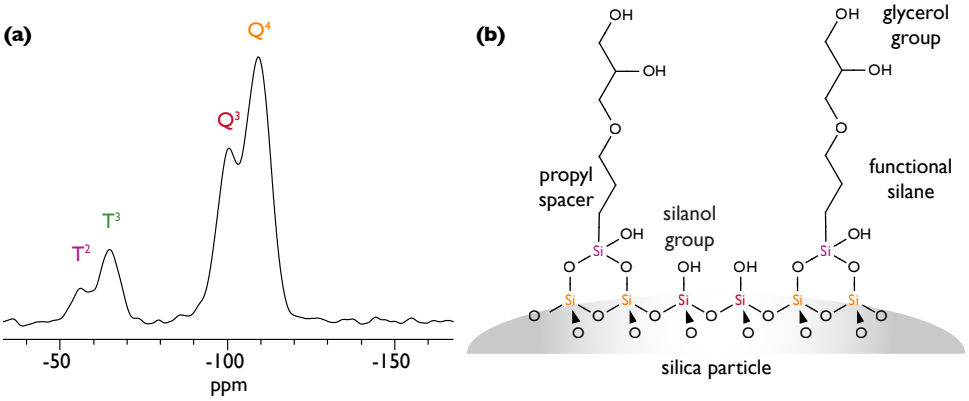

Figure 3.2.7: (a) Silicon-29 CPMAS spectrum of the glycerol-functionalized silica sol (*Bindzil CC40*) recorded at a MAS rate of 12 kHz. (b) Schematic diagram of the functionalization, showing one of the two possible modes of attachment of the glycerol-functional silane to the surface, as suggested by the silicon-29 chemical shifts.

condensation between the silane molecules[15], the first of the two possible modes of attachment suggested by these silicon-29 shifts is illustrated in Figure 3.2.7(b). The second mode involves a tetrahedral structure whereby the silane molecule is attached via bridging oxygen bonds to three surface silicon atoms. Consequently, this mode is not illustrated owing to its three-dimensional structure.

The variation in the CPMAS intensity (points) of the Q^3 (red squares) , T^2 (purple open circles) and T^3 (green filled circles) peaks with the contact time is plotted in Figure 3.2.8. The phenomenological expression for CP transfer in the

[15]Evidence to suggest otherwise cannot be found in the literature although theoretically this self-condensation reaction is possible. Future experiments to test for the proportion of self-condensation between functionalized silanes on silica surfaces are in preparation.

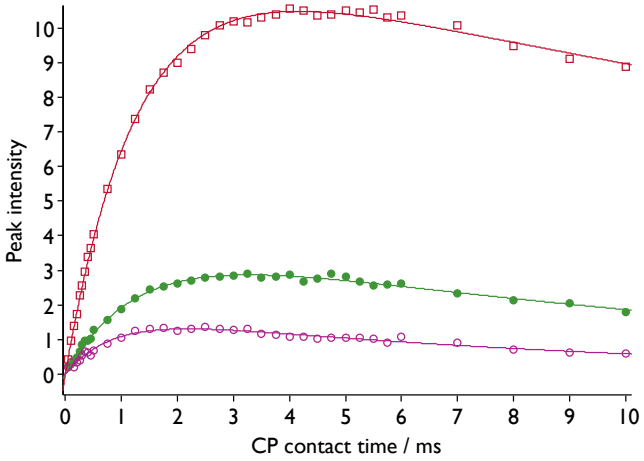

Figure 3.2.8: Peak intensities (points) for Q^3 (red squares), T^2 (purple open circles) and T^3 (green filled circles) silicon environments for a *Bindzil CC40* glycerol-functionalized silica sol as a function of contact time with fits (lines) to a phenomenological expression for their build-up via cross polarization. The fitting of the phenomenological expression was performed by *MATLAB* software.

rotating frame is

$$S(\tau_{cp}) = S_0 \frac{[\exp(-\tau_{cp}/T_{1\rho}) - \exp(-\tau_{cp}/T_{IS})]}{1 - (T_{IS}/T_{1\rho})} \tag{3.2.1}$$

where τ_{cp} is the CP contact time, $T_{1\rho}$ is the spin-lattice relaxation time in the rotating frame and $1/T_{IS}$ is the CP rate constant. Note that this phenomenological expression is for a multi-spin system. The expression breaks down in the limit of few coupled spins. However, the fits (lines in Figure 3.2.8) to this standard expression for the build-up of intensity show that the system is in the multi-spin regime. The fits allow the relative proportions of each of the silicon environments to be quantified. The results of the fits are given in Table 3.2.2. Note that

Table 3.2.2: Results of fits to the phenomenological expression for CP transfer in the rotating frame (equation (3.2.1)) for silicon environments in *Bindzil CC40*. The numbers in brackets are 95 % confidence bounds.

Peak	S_0	T_{IS} / ms	$T_{1\rho}$ / ms
Q^3	12.65 (12.32, 12.98)	1.272 (1.224, 1.320)	29.16 (25.80, 32.52)
T^2	1.868 (1.665, 2.071)	0.8585 (0.7315, 0.9855)	8.607 (7.039, 10.18)
T^3	4.169 (3.890, 4.448)	1.300 (1.198, 1.403)	12.44 (10.84, 14.04)

the Q^3 line arises exclusively from silanol sites on the surface of the silica particles, while both the T lines result from silicon-29 nuclei in the glycerol-functional silane. Comparison of the Q^3 intensity with the total of T^2 and T^3 indicates that there are 2.1 unreacted silanol groups on the silica surface for every attached silane. However, the relative intensity of the T^2 and T^3 lines suggests that silane molecules are 2.2 times more likely to have reacted with three surface silanols than with two. Taken together, these results imply that 56 % of the original silanol groups on the silica surface have reacted during functionalization. Note, however, that this is assuming that no self-condensation between silane molecules occurs.

It is important to comment on the nature of the fitting of the line from equation (3.2.1). It is usually assumed that the CP time for magnetization transfer, T_{IS}, is shorter than the spin-lattice relaxation time in the rotating frame of the abundant spins, $T_{1\rho}$. However, this is not always the case. Erroneous parameters are returned when assuming the fast CP regime ($T_{1\rho} > T_{IS}$) when the spin system

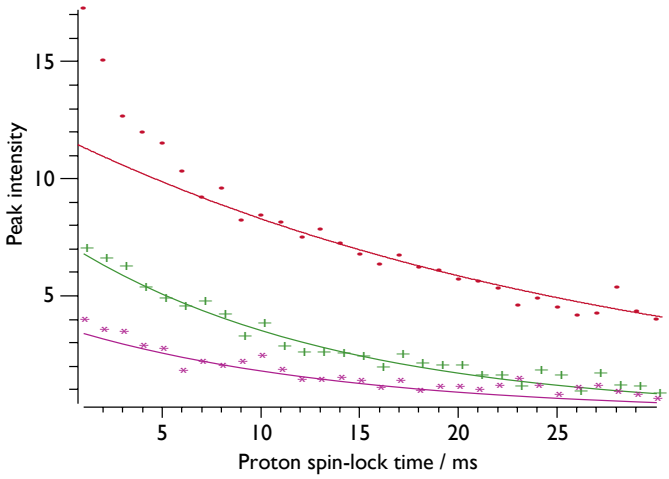

Figure 3.2.9: Peak intensities (points) for Q^3 (red circles), T^2 (purple stars) and T^3 (green crosses) silicon environments for a *Bindzil CC40* glycerol-functionalized silica sol as a function of proton spin-lock time for cross polarization with fits (lines) to an exponential decay, used to determine $T_{1\rho}$. The fitting of the exponential decay was performed by *MATLAB* software.

under investigation is actually in the slow CP regime ($T_{IS} > T_{1\rho}$). It has been shown that the slow CP regime can be found in Q^4 sites in silica gels as well as other systems [82]. Thus, care must be taken. To this effect $T_{1\rho}$ was measured independently. The peak intensity resulting from a modified CP experiment which has an additional period of transverse proton *spin-locking*[16], τ_{SL}, before the dual CP pulses has the form

$$S(\tau_{SL}) = S_0 \exp(-\tau_{SL}/T_{1\rho}) \tag{3.2.2}$$

By varying τ_{SL} and fitting the intensities returned to an exponential decay $T_{1\rho}$

[16]Spin-locking is a pulse sequence that maintains magnetization in a certain plane for a certain duration.

can be determined. Figure 3.2.9 shows the peak intensities (points) for Q^3 (red circles), T^2 (purple stars) and T^3 (green crosses) silicon environments for the *Bindzil CC40* glycerol-functionalized silica sol as a function of τ_{SL} with fits (lines) to an exponential decay. $T_{1\rho}$ was found to be 28.5 ms for Q^3, 14.0 ms for T^2 and 13.6 ms for T^3 sites. These independently measured $T_{1\rho}$ times are of a similar magnitude to those obtained from the original fits to equation (3.2.1) and are at least an order of magnitude greater than the corresponding T_{IS} times in both instances. Therefore, the measured silicon sites are in the fast CP regime where $T_{1\rho} >> T_{IS}$ and the previous analysis can be concluded as valid.

The method of Agarwal and co. [73] employed to characterise the interface of nanocomposite particles involved the use of proton-carbon-13 correlation spectra to resolve and assign the proton resonances for the polymer and silica components of the nanocomposite. Subsequently, complementary proton-silicon-29 correlation spectra allowed the proximity of the different polymer protons to the silica particle surface to be assessed. This method will be used here for the next-generation nanocomposite particles. Figure 3.2.10 shows a proton-carbon-13 correlation spectrum of the P(S-co-n-BuA)/silica nanocomposite. This correlation experiment uses the MAS-J-HMQC pulse sequence of Figure 3.1.1 and is thus mediated by J-couplings between protons and carbon-13 nuclei. This experiment was chosen due to the high-resolution obtained in the proton dimension. The experimental parameters are given in the figure caption. Even though this

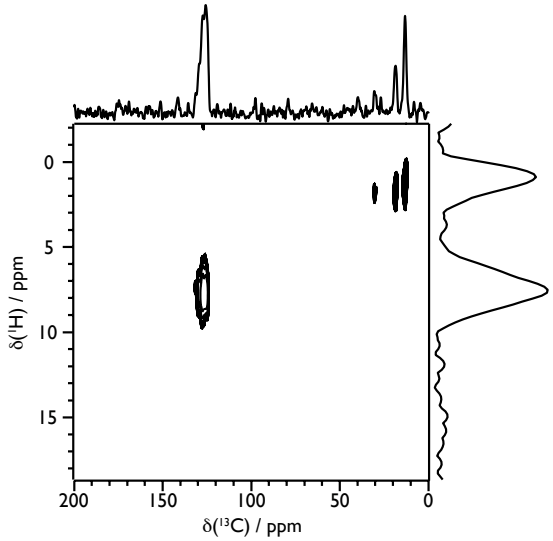

Figure 3.2.10: Two-dimensional ^{1}H-^{13}C MAS-*J*-HMQC spectrum of the P(S-co-n-BuA)/silica nanocomposite, recorded using the pulse sequence in Figure 3.1.1. The MAS rate was 12 kHz and 512 scans were recorded for each of 64 t_1 increments with a recycle delay of 2.3 s being inserted between scans. 100 kHz of CW decoupling was used during t_2. A dwell time of 25.0 μs was combined with a direct acquisition time of 51.20 ms in t_2 whilst a dwell time of 64.0 μs was used in t_1 giving a total indirect acquisition time of 16.4 ms. 50 DUMBO-1 cycles were used in each delay period, resulting in τ = 1.5 ms. Also shown are skyline projections of the two-dimensional spectrum parallel to the ^{13}C (top) and ^{1}H (right) frequency dimensions.

experiment took approximately 21.5 hours to acquire, the signal-to-noise ratio is low and many of the expected peaks are missing. The peaks that are present relate to the protonated carbons in the PS aromatic ring (δ (^{13}C) = +127 ppm) and the three aliphatic carbons from the P(n-BuA) that are furthest away from the polymer backbone (δ (^{13}C) = +13, +18 and +30 ppm).

As illustrated in Figure 3.2.5 the organic polymer latex is a large proportion of the nanocomposite. The interface between the polymer latex and the mod-

ified silica particles is a vastly smaller proportion of the nanocomposite. Even though silicon-29 has approximately four times the natural isotopic abundance of carbon-13, the limiting factor of the small amount of interface will result in a very low signal-to-noise ratio for proton-silicon-29 correlation experiments. Since the proton-carbon-13 MAS-*J*-HMQC spectrum shown in Figure 3.2.10 does not exhibit all of the expected correlation peaks due to the lack of signal-to-noise then it can be presumed that a proton-silicon-29 MAS-*J*-HMQC experiment would also reveal little. Furthermore, a chemical bond is not necessarily formed between the organic and inorganic parts of the nanocomposite (c.f. PS/silica nanocomposite of Ref. [73]) so the use of scalar couplings might not allow the full characterisation of the interface. As stated previously, in certain situations greater signal-to-noise can be achieved by using dipolar correlations rather than scalar correlations. In addition, the proximity of heteronuclei can still be attained using these correlations although the presence of a chemical bond is now not necessary.

A new pulse sequence was devised which combines the high proton resolution achieved with the state-of-the-art homonuclear decoupling described in Section 2 and the dipolar correlations achieved using the pulse sequence from Figure 3.2.2. This should result in the highest proton resolution possible for the heteronuclear correlation experiment, combined with the greater signal-to-noise of dipolar correlation experiments. The pulse sequence for this new experiment is depicted in Figure 3.2.11. This experiment will be labelled as DUMBO-LGCP throughout

this work. At the start of the preparation period carbon-13 or silicon-29 spins are saturated by a small number of $\pi/2$ pulses separated by delays that are short compared to the spin-lattice relaxation time. Subsequently, a $\pi/2$ pulse generates proton transverse magnetization that evolves during t_1 under the windowless DUMBO-1 homonuclear decoupling sequence [42]. The mixing period is initiated by three proton pulses with flip angles of θ, $\pi/2$ and 54.7°, respectively, before transfer of magnetization to neighbouring heteronuclear spins is achieved using Lee-Goldburg cross-polarization (LG-CP) [83]. The θ pulse, which is carefully calibrated according to the procedure given Ref. [42], rotates one component of the proton magnetization precessing about the tilted field under DUMBO-1 into the xy-plane. The $\pi/2$ pulse then rotates the magnetization onto the z-axis. Finally, the proton magnetization is rotated by an additional pulse of flip angle 54.7°. This magnetization is spin-locked during the LG-CP period in an effective magnetic field tilted at this same angle to the z-axis, resulting in the suppression of proton spin diffusion. During the spin-locking, a carbon-13 or silicon-29 RF field is applied at the Hartmann-Hahn condition to give selective magnetization transfer. The carbon-13 or silicon-29 FID is detected as usual with heteronuclear decoupling during t_2.

Before further experiments were performed on the nanocomposites it was deemed necessary to characterise the sol. Figure 3.2.12 shows a series of ^{1}H-^{29}Si DUMBO-LGCP dipolar correlation spectra of the *Bindzil CC40* glycerol-functionalized sil-

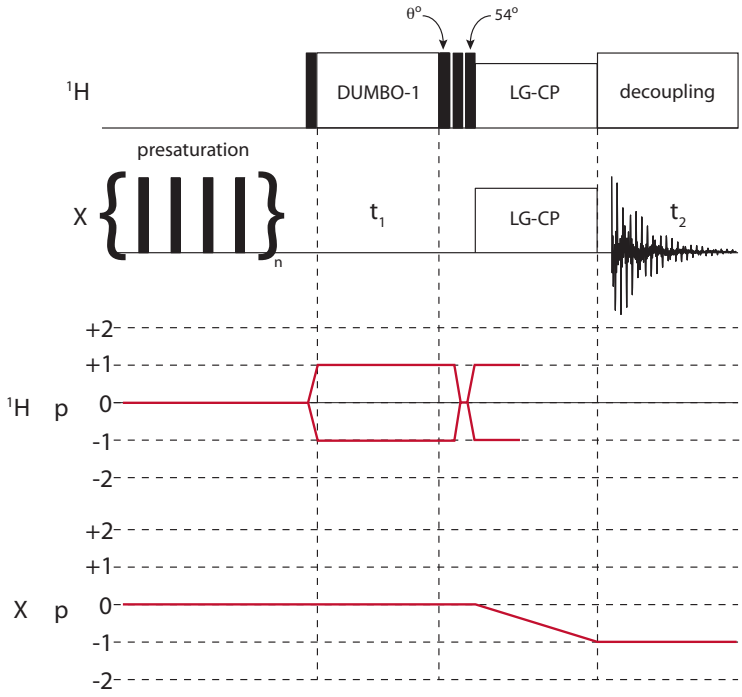

Figure 3.2.11: Pulse sequence used to record high-resolution two-dimensional DUMBO-LGCP heteronuclear dipolar correlation spectra. Filled vertical bars represent $\pi/2$ pulses unless otherwise stated.

ica sol recorded as a function of contact time using the pulse sequence of Figure 3.2.11. The skyline projections taken parallel to the ^{29}Si dimension (top) show the same T and Q silicon environments as the corresponding ^{29}Si CPMAS spectrum (c.f. Figure 3.2.7(a)). For the shortest contact time of 1 ms (Figure 3.2.12(a)) the two-dimensional spectrum shows peaks which result from selective cross polarization to ^{29}Si nuclei from nearest neighbour protons only. The most intense peak correlates the Q^3 silanol line at δ = -100 ppm in the ^{29}Si dimension with a broad resonance centering at δ = +4.5 ppm in the ^{1}H dimension. This can be assigned to the silanol protons and is similar to that observed in unmodified silica sols

[73]. The T lines around $\delta(^{29}\text{Si})$ = -65 ppm are correlated to a narrower ^{1}H signal at δ = +1.0 ppm which therefore arises from the propyl spacer in the functional silane. The propyl and silanol resonances are resolved in the skyline projection parallel to the ^{1}H dimension (right). As the contact time increases to 3 ms (Figure 3.2.12(b)) the main change is an increase in the relative intensity of the Q^4 correlation peak. This is expected since cross polarization becomes efficient over larger distances at longer contact times and these sites are further away from their nearest proton neighbours. In contrast, for the Q^3 silanol environment the cross peak shape does not change significantly, suggesting that cross polarization in this case is still dominated by nearest neighbour silanol protons. Even at the longest contact time of 5 ms (Figure 3.2.12(c)) there are no correlations between the silicon T sites and the glycerol protons which are separated by more than 5 Å. This observation provides an upper limit on the distance over which cross polarization from protons to ^{29}Si nuclei is effective, and demonstrates that the ^{1}H-^{29}Si dipolar correlation spectra can be used to identify those protons which are closer than 5 Å to the surface of the silica particle.

To analyse the nanocomposite samples in greater detail the chemical shifts of the protons in the polymers also need to be characterised. Subsequently, an assignment of the ^{1}H-^{29}Si correlations in each of the nanocomposite samples can be made using the knowledge of the polymer and funcitionalized-silica proton chemical shifts. Figure 3.2.13 shows ^{1}H-^{13}C DUMBO-LGCP dipolar correlation spectra

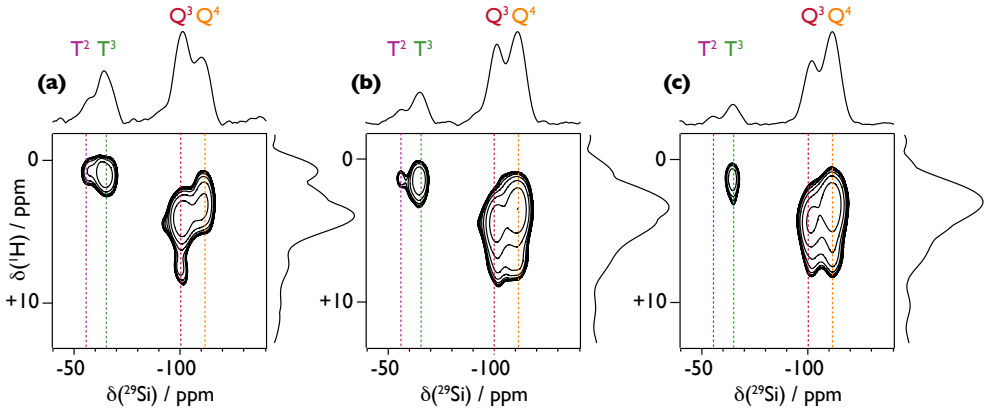

Figure 3.2.12: Two-dimensional ^{1}H-^{29}Si DUMBO-LGCP spectra of the *Bindzil CC40* silica sol recorded using the pulse sequence in Figure 3.2.11 with LG-CP contact times of 1 ms (a), 3 ms (b) and 5 ms (c), respectively. For each spectrum the MAS rate was 12 kHz and 1408 scans were recorded for each of 64 t_1 increments with a recycle delay of 1 s being inserted between scans. 100 kHz of CW decoupling was used during t_2. A dwell time of 20 μs was combined with a direct acquisition time of 20.48 ms in t_2 whilst a dwell time of 30 μs was used in t_1 giving a total indirect acquisition time of 1.92 ms. Also shown are skyline projections of the two-dimensional spectra parallel to the ^{29}Si (top) and ^{1}H (right) frequency dimensions.

of the P(n-BuA)/silica nanocomposite ((a) and (b)) and the PS/silica nanocomposite (c). The ^{1}H resonances extracted from these spectra will be predominantly associated with the polymer phase since the relative amount of carbon contained within the glycerol-functionalized silica sol can be considered negligible when compared to the amount of polymer latex. The chemical shifts of the carbon-13 environments in these polymers are relatively well known and thus an assignment of the ^{1}H resonances can be made from correlations to these environments. The spectra in Figures 3.2.13(a) and 3.2.13(b) were recorded at different temperatures as given in the figure caption. The spectrum in Figure 3.2.13(a) was recorded at

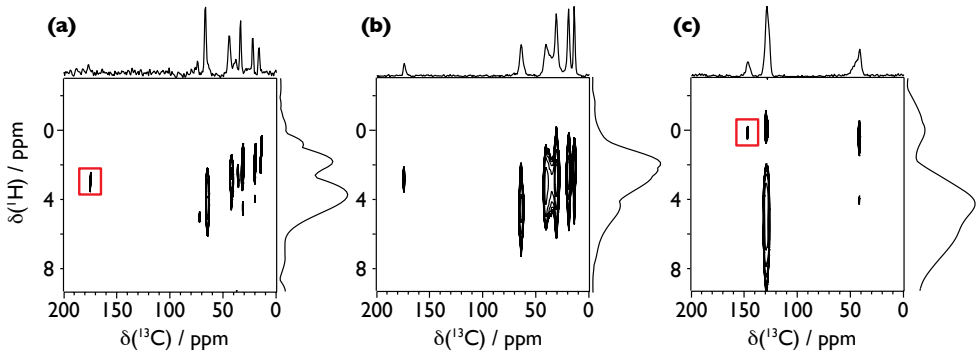

Figure 3.2.13: Two-dimensional ^{1}H-^{13}C DUMBO-LGCP spectra of the P(n-BuA)/silica nanocomposite taken at a temperature of 291 K (a) and 213 K (b) and also the PS/silica nanocomposite at 291 K (c). All were recorded using the pulse sequence in Figure 3.2.11 with a LG-CP contact time 1 ms. For each spectrum the MAS rate was 12 kHz and 704 scans were recorded for each of 128 t_1 increments for (a) and (c) and 144 scans were recorded for each of 128 t_1 increments for (b) all with a recycle delay of 1 s being inserted between scans. 100 kHz of CW decoupling was used during t_2. A dwell time of 20 μs was combined with a direct acquisition time of 20.48 ms in t_2 whilst a dwell time of 30 μs was used in t_1 giving a total indirect acquisition time of 3.84 ms. Also shown are skyline projections of the two-dimensional spectra parallel to the ^{13}C (top) and ^{1}H (right) frequency dimensions. The sections highlighted by red rectangles have been plotted at lower contour levels to allow correlations to be revealed.

a temperature above the glass transition temperature (T_g) of the sample whereas the spectrum in Figure 3.2.13(b) was recorded at a temperature below the T_g of the sample. This results in resonances from the glycerol-functionalized silane being observed in Figure 3.2.13(a) (for example the peak at $\delta(^{13}\mathrm{C}) = +72$ ppm) which would not be expected in a spectrum of the solid sample. Thus, it was necessary to record a spectrum of the nanocomposite sample below the T_g as a comparison. The P(n-BuA)/silica nanocomposite is the only sample in this study which is above its T_g at normal operating temperatures (room tempera-

ture). It is worth noting that the skyline projections parallel to the ^{1}H dimension demonstrate that the linewidths of the proton resonances are smaller in the sample above its T_g but that the chemical shifts are the same; although the ratios of the intensities of the resonances are different. The variation in ^{1}H projection intensity between Figures 3.2.13(a) and 3.2.13(b) is solely due to the different state of the sample in each. Since the ^{1}H-^{13}C DUMBO-LGCP spectrum for the P(n-BuA)/silica nanocomposite does not differ significantly above and below its T_g it can be said that the sample acts similarly to the solid at room temperature. Thus, it was deemed satisfactory to record the ^{1}H-^{29}Si DUMBO-LGCP spectrum at room temperature.

Figure 3.2.14 shows ^{1}H-^{29}Si DUMBO-LGCP dipolar correlation spectra of the PS/silica (a) and the P(n-BuA)/silica (b) nanocomposites, both recorded at a temperature of 291 K. Also shown (right) are the skyline projections parallel to the ^{1}H dimension from the complementary ^{1}H-^{13}C DUMBO-LGCP correlation spectra. For Figure 3.2.14(b) the ^{1}H projection from the ^{1}H-^{13}C correlation spectrum of the P(n-BuA)/silica nanocomposite sample below its T_g was used. The contact time for the ^{1}H-^{29}Si DUMBO-LGCP experiments was 3 ms which represented the best compromise between the signal-to-noise ratio in the spectra and the selectivity of the cross polarization process. Compared to the sol the silica content of the nanocomposites is reduced, and so correlations involving T silicon environments are no longer of sufficient signal-to-noise to be detectable.

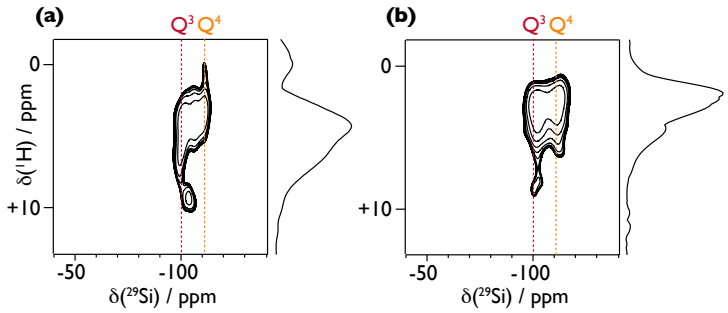

Figure 3.2.14: Two-dimensional ^{1}H-^{29}Si DUMBO-LGCP spectra of the PS/silica (a) and P(n-BuA)/silica (b) nanocomposites recorded using the pulse sequence in Figure 3.2.11 with a LG-CP contact time 3 ms. For both spectra the MAS rate was 12 kHz and 2800 scans were recorded for each of 64 t_1 increments for (a) and 1552 scans were recorded for each of 128 t_1 increments for (b), both with a recycle delay of 1 s being inserted between scans. 100 kHz of CW decoupling was used during t_2. A dwell time of 20 μs was combined with a direct acquisition time of 20.48 ms in t_2 whilst a dwell time of 30 μs was used in t_1 giving a total indirect acquisition time of 1.92 ms for (a) and 3.84 ms for (b). Also shown (right) are skyline projections of DUMBO-LGCP ^{1}H-^{13}C dipolar correlation spectra of the same samples which show predominantly ^{1}H resonances associated with the polymer phase. The latter can be used to assign correlations involving polymer protons which appear in the former.

Nevertheless, the spectra provide useful information about the interface between the polymer and silica components of these nanocomposites. For the PS/silica nanocomposite (Figure 3.2.14(a)) the Q^3 cross peak is elongated towards higher δ in the ^{1}H dimension when compared with the corresponding spectrum of the glycerol-functionalized silica sol in Figure 3.2.12(b). This implies that, for the nanocomposite, ^{29}Si nuclei in Q^3 sites at the surface of the silica particles are cross polarized by additional protons with signals in the range $\delta = +6$ to $+8$ ppm. These protons can be identified by comparison with the ^{1}H skyline projection. Styrene aromatic protons at $\delta = +7.0$ ppm are clearly the origin of

the additional cross polarization to the Q^3 silicon environment observed in the ^1H-^{29}Si spectrum. This demonstrates that in the PS/silica nanocomposite some styrene protons are no more than 5 Å from Q^3 ^{29}Si nuclei in the surface of the silica particle. Therefore, these pendent styrene side groups are actually closer to the Q^3 silanol sites in the silica surface than the glycerol groups themselves. In addition, there is a significant extra cross peak between a new Q silicon site which appears at δ = -104 ppm and a highly deshielded proton which resonates at δ = +9.5 ppm. A possible explanation for these unusual ^1H and ^{29}Si shifts is the presence of a π-interaction between the silanol group and the aromatic ring in the styrene residues, providing further evidence for the close proximity of the polymer side groups to the silica surface. Another possible explanation is that the AIBA initiator used in the preparation of the nanocomposites is present at the interface. AIBA contains NH_2 protons which could resonate at δ values similar to those observed for the highly deshielded proton at δ = +9.5 ppm if they were hydrogen-bonded to the surface.

In the ^1H-^{29}Si spectrum of the P(n-BuA)/silica nanocomposite (Figure 3.2.14(b)) the shape of the Q^3 peak indicates an additional correlation with shielded protons at δ values as low as +2 ppm when compared with the glycerol-functionalized silica sol (Figure 3.2.12(b)). Comparison with the ^1H skyline projection identifies these as aliphatic protons in the n-butyl side chains of the acrylate residues with resonances at +2.0 and +3.5 ppm. Therefore, the spectra depicted in Figure

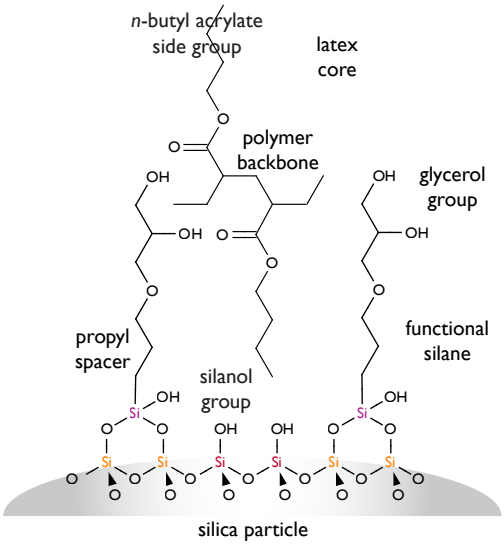

Figure 3.2.15: Schematic representation of the latex/silica interface, showing the n-butyl side groups of the (co)polymer extending between the propyl spacers of the glycerol-functional silane molecules towards the silica surface.

3.2.14 provide clear evidence that, in both nanocomposites, polymer chains at the latex surface contact glycerol-functional silane molecules with at least some of their side groups extending between the propyl spacers towards the silica particle surface, as shown schematically in Figure 3.2.15. If this were not the case, the ^{1}H-^{29}Si dipolar correlation spectra of both nanocomposites (Figure 3.2.14) would be identical to that of the silica sol (Figure 3.2.12(b)), since all polymer protons would be too distant to cross polarize Q silicon sites at the particle surface. Given the aqueous emulsion polymerization conditions, it is possible that hydrophobic interactions promote initial adsorption of the water-insoluble styrene and n-butyl acrylate monomers between the glycerol-functional silane molecules prior to polymerization.

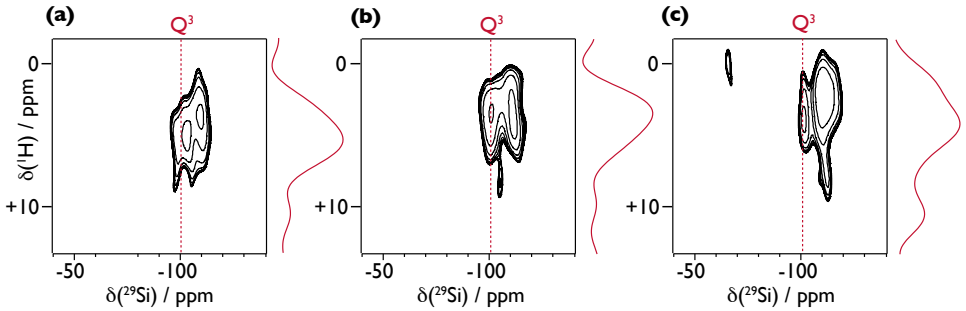

Figure 3.2.16: Two-dimensional ^{1}H-^{29}Si DUMBO-LGCP spectra of the P(S-co-n-BuA)/silica nanocomposite recorded using the pulse sequence in Figure 3.2.11 with LG-CP contact times of 1 ms (a), 3 ms (b) and 5 ms (c), respectively. For each spectrum the MAS rate was 12 kHz and 2496 scans were recorded for each of 64 t_1 increments for (a) and (c) and 1696 scans were recorded for each of 64 t_1 increments for (b) all with a recycle delay of 1 s being inserted between scans. 100 kHz of CW decoupling was used during t_2. A dwell time of 20 μs was combined with a direct acquisition time of 20.48 ms in t_2 whilst a dwell time of 30 μs was used in t_1 giving a total indirect acquisition time of 1.92 ms. Also shown (right) are cross-sections taken parallel to the ^{1}H dimension at the Q^3 ^{29}Si frequency, as indicated by the dotted line.

The copolymer/silica nanocomposite presents a further uncertainty compared to the separate polymer/silica nanocomposites. With the latter nanocomposites there is evidence that polymer chains are in close proximity to the surface of the silica sol. However, when the polymers are combined as a copolymer there is an uncertainty as to whether one, both or neither of the polymers is/are able to approach the surface of the sol. Figure 3.2.16 shows ^{1}H-^{29}Si DUMBO-LGCP dipolar correlation spectra of the P(S-co-n-BuA)/silica nanocomposite, recorded as a function of contact time. Note that all these spectra bear a close resemblance to that of the P(n-BuA)/silica nanocomposite (Figure 3.2.14(b)) and are quite different to that of the PS/silica nanocomposite (Figure 3.2.14(a)). In particular,

the correlation between the Q^3 silicon at the surface of the silica particle and the styrene aromatic protons observed for the latter nanocomposite is absent. This indicates that in the P(S-co-n-BuA)/silica nanocomposite n-butyl acrylate residues are preferentially located at the silica surface to the exclusion of styrene residues. Corroborating evidence for this is provided by a detailed examination of the Q^3 cross peak shapes as a function of contact time, as well as the cross-sections (right) taken parallel to the ^{1}H dimension at the Q^3 ^{29}Si frequency. At short contact times the latter are expected to be dominated by signals from the nearest neighbour silanol protons, but at longer times there will be an increasing contribution from polymer protons, since these are present in greater concentration. At the shortest contact time (Figure 3.2.16(a)) the ^{1}H cross-section shows a silanol resonance similar to that observed for the glycerol-functionalized silica sol in Figure 3.2.12(a) with $\delta = +5.0$ ppm. However, as the contact time is increased to 3 ms (Figure 3.2.16(b)) there is a distinct shift in the Q^3 correlation peak along the ^{1}H dimension to lower δ values, and this is clearly observed in both the peak shape and the cross-section. This behavior is similar to that observed for the P(n-BuA)/silica nanocomposite (Figure 3.2.14(b)), but different from the glycerol-functionalized silica sol, and suggests that the Q^3 ^{29}Si nuclei are cross polarized at longer times by aliphatic protons on the n-butyl side chains in the range $\delta = +2.0$ to $+3.5$ ppm. When the contact time reaches 5 ms (Figure 3.2.16(c)) protons from the propyl spacer in the glycerol-functional silane at +1.0 ppm also

cross polarize the Q^3 ^{29}Si nuclei, since the cross polarization process is no longer as selective. However, even at 5 ms no correlations are observed between Q^3 silicon environments and aromatic protons in the styrene residues. These observations confirm that n-butyl acrylate residues in the copolymer interact with the surface of the silica particles in preference to styrene residues.

This result is consistent with both XPS and DSC data already reported [79] for the P(S-co-n-BuA)/silica nanocomposite particles. The former technique which probes the elemental composition of the 200 nm diameter nanocomposite particles with a typical sampling depth of 2 - 5 nm indicated that their surface is rich in silicon, consistent with their known core-shell morphology. In contrast, the ^{1}H-^{29}Si NMR experiments provide chemical information about the region within 5 Å of the surface of the silica particles which form the shell surrounding the (co)polymer latex core. Note that a carbonyl peak in the C1s core-line X-ray photoelectron spectrum was observed previously [79] for a P(S-co-n-BuA)/silica film. This suggests that n-butyl acrylate residues are preferentially located at the surface of the nanocomposite particles and corroborates the NMR results. T_g for a series of P(S-co-n-BuA)/silica nanocomposite particles were determined experimentally by DSC and compared with theoretical values calculated from the Flory-Fox equation by Schmid et al. [79]. The observed discrepancies increase with the acrylate content, indicating a specific interaction between the silica particles and the n-butyl acrylate residues. One plausible explanation could be

a hydrogen bonding interaction which could occur between the n-butyl acrylate ester carbonyl and either the silanol or the glycerol groups on the functionalized surface. The NMR spectra in Figures 3.2.14 and 3.2.16 allow the former to be conclusively eliminated, since there is no evidence for a correlation between any hydrogen-bonded protons (expected at higher δ) and the silanol silicon sites. However, the latter interaction cannot be ruled out on the basis of the NMR evidence because the glycerol protons are too distant to effectively cross polarize ^{29}Si nuclei at the surface of the silica particle. With regard to the mechanism of particle formation, Schimd et al. have raised the possibility of chain transfer from growing polystyrene radicals to the surface glycerol groups. While the NMR results presented here are not incompatible with this hypothesis, they do not conclusively prove it.

3.2.3 Next-Generation Nanocomposite Particles 2

The next stage in the development of the nanocomposite particles was investigated. These nanocomposite particles were prepared using an unmodified silica sol and fall into two categories. Firstly, core-shell nanocomposite particles prepared *in situ* from a standard silica sol (*Nyacol 2040*) and secondly, core-shell nanocomposite particles prepared by heteroflocculation[17] of a sterically-stabilised

[17]Flocculation: a process whereby colloids come out of suspension to form into small clumps or masses.

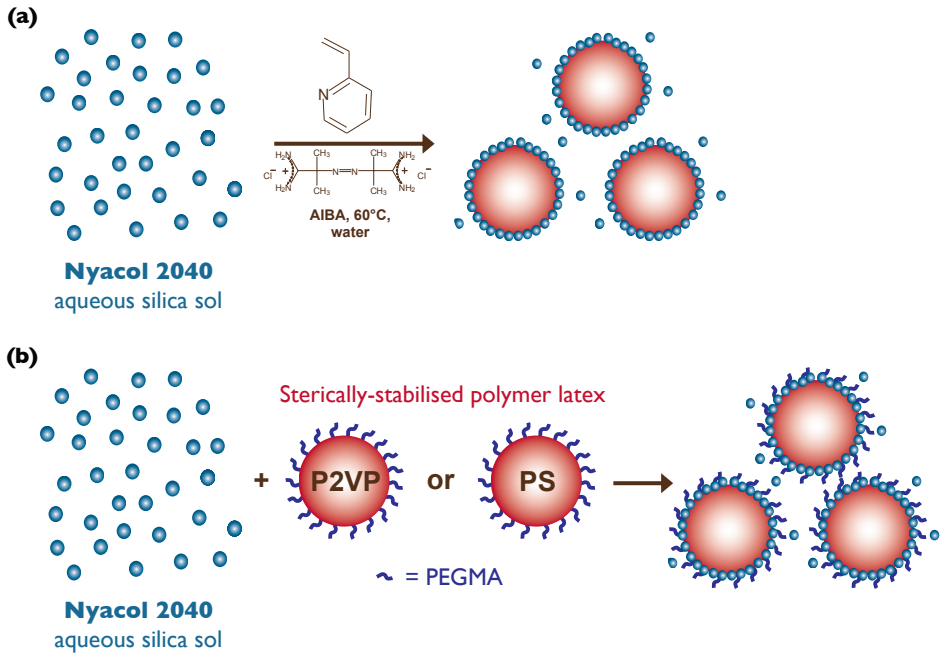

Figure 3.2.17: Schematic representation of the synthesis of colloidal nanocomposite particles by *in situ* aqueous polymerization of 2-vinyl pyridine in the presence of a *Nyacol 2040* silica sol (a) and by adsorption of a *Nyacol 2040* silica sol onto a sterically-stabilised polymer latex (b).

polymer latex with the *Nyacol 2040* silica sol. Figure 3.2.17 shows a schematic diagram of the syntheses of these nanocomposites. Figure 3.2.17(a) shows that the poly(2-vinyl pyridine) (P2VP)/silica nanocomposite particles were prepared in a similar manner to the P(n-BuA)/silica nanocomposite particles described in Section 3.2.2 except that the monomer is 2-vinyl pyridine and the silica sol is *Nyacol 2040*. A detailed description of this synthesis can be found in the literature [84]. Figure 3.2.17(b) depicts a different method of synthesis where a sterically-stabilised polymer latex was first formed before heteroflocculation with the silica sol. Monomethoxy-capped poly(ethylene glycol) methacrylate (PEGMA) was

used as the stabilising agent and thus (P2VP-PEGMA)-silica and (PS-PEGMA)-silica nanocomposite particles were formed[18]. A more detailed description of the synthesis of these nanocomposites can be found in the literature [85]. Heteroflocculation of non-stabilised polymer latexes with *Nyacol 2040* silica sol have so far been unsuccessful, suggesting that stabilisation of the polymer latex is essential for the production of these colloidal nanocomposite particles and that the PEGMA has a role in the binding interaction. Furthermore, it is known that poly(ethylene glycol) is physically adsorbed onto the surface of colloidal silica [86–89]. Therefore, this interaction could be the driving force for heteroflocculation in these nanocomposites [85].

The ^{29}Si CPMAS spectrum of the *Nyacol 2040* silica sol is shown in Figure 3.2.18(a). This figure illustrates that there are only the three silicon-29 environments expected and that no appreciable amount of unwanted surface modification of the silica sol has occurred. Unlike the *Bindzil CC40* glycerol-modified silica sol studied earlier, the Q^4 resonance from the *Nyacol 2040* silica sol is only due to bulk silicon whereas the Q^3 and Q^2 resonances are from similar silicon sites in silanol and bridging silanol groups on the surface, respectively. Figure 3.2.18(b) shows the ^{1}H-^{29}Si DUMBO-LGCP spectrum of the *Nyacol 2040* silica sol recorded with a LG-CP contact time of 3 ms. The skyline projection taken parallel to the

[18]The nomenclature of the nanocomposites is determined by the method of production. Polymer/silica nanocomposites are prepared by *in situ* polymerization of the monomer with the silica sol whereas the polymer-silica nanocomposites are prepared by heteroflocculation of the polymer latex with the silica sol.

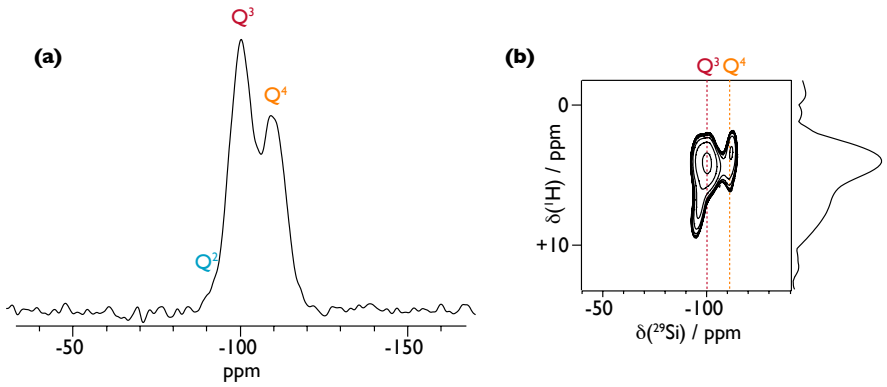

Figure 3.2.18: Silicon-29 CPMAS (a) and two-dimensional ^{1}H-^{29}Si DUMBO-LGCP (b) spectra of the *Nyacol 2040* silica sol recorded at a MAS rate of 12 kHz, with a contact time of 10 ms for (a) and 3 ms for (b) and with a recycle delay of 1 s being inserted between scans for both. For the two-dimensional spectrum shown in (b) 4640 scans were recorded for each of 64 t_1 increments, 100 kHz of CW decoupling was used during t_2, a dwell time of 20 μs was combined with a direct acquisition time of 20.48 ms in t_2 and a dwell time of 30 μs was used in t_1 giving a total indirect acquisition time of 1.92 ms. Also shown in (b) is a skyline projection (right) of the spectrum parallel to the ^{1}H frequency dimension

^{1}H dimension (right) highlights the range of chemical shifts that result from the surface silanol protons since these are the only protons present in this system. The projection also demonstrates that the maximum proton intensity in this system is at $\delta = +4.5$ ppm, which is consistent with the value for the silanol protons in the *Bindzil CC40* glycerol-modified silica sol (Figure 3.2.12) and also the value recorded previously for this silica sol [73].

Like the analysis of the nanocomposites in the previous section, ^{1}H-^{13}C dipolar correlation spectra of these nanocomposites prepared from the *Nyacol 2040* silica sol were recorded so that the chemical shifts of the protons in the polymers could

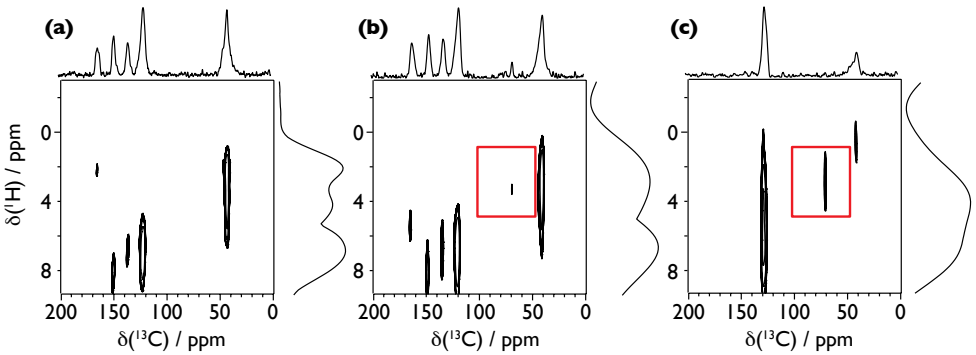

Figure 3.2.19: Two-dimensional ^{1}H-^{13}C DUMBO-LGCP spectra of the P2VP/silica (a), (P2VP-PEGMA)-silica (b) and (PS-PEGMA)-silica (c) nanocomposites. All were recorded using the pulse sequence in Figure 3.2.11 with a LG-CP contact time 1 ms. For each spectrum the MAS rate was 12 kHz and 704 scans were recorded for each of 128 t_1 increments for (a), 864 scans were recorded for each of 64 t_1 increments for (b) and 1024 scans were recorded for each of 64 t_1 increments for (c), all with a recycle delay of 1 s being inserted between scans. 100 kHz of CW decoupling was used during t_2. A dwell time of 20 μs was combined with a direct acquisition time of 20.48 ms in t_2 whilst a dwell time of 30 μs was used in t_1 giving a total indirect acquisition time of 3.84 ms for (a) and 1.92 ms for (b) and (c). Also shown are skyline projections of the two-dimensional spectra parallel to the ^{13}C (top) and ^{1}H (right) frequency dimensions. The sections highlighted by red rectangles have been plotted at lower contour levels to allow correlations to be revealed.

be ascertained. Figure 3.2.19 shows the ^{1}H-^{13}C DUMBO-LGCP spectra of the P2VP/silica nanocomposite (a), the (P2VP-PEGMA)-silica nanocomposite (b) and the (PS-PEGMA)-silica nanocomposite (c). Also shown are the skyline projections of the two-dimensional spectra parallel to the ^{13}C (top) and ^{1}H (right) frequency dimensions. The known assignment of the carbon-13 chemical shifts of the polymers allow the proton resonances to be assigned from the correlations. The spectra from Figures 3.2.19(b) and 3.2.19(c) exhibit a correlation at $\delta(^{13}\mathrm{C}) =$ +70 ppm. However, the signal-to-noise ratio of this correlation peak is very low

and as a result it is not observed within the plotted contour levels. The sections highlighted by red rectangles have been plotted starting from lower contour levels and this allows this correlation to be revealed. This correlation is not observed at any range of the contours of the spectrum from Figure 3.2.19(a). This is to be expected since the correlation at $\delta(^{13}C) = +70$ ppm is from the poly(ethylene glycol) tail of the PEGMA. The very low signal-to-noise ratio is due to the relatively small amount of PEGMA compared to the polymer (approximately 1-2 wt %). This carbon-13 resonance from the PEGMA is correlated to a proton resonance centering at $\delta = +3.5$ ppm. This is consistent with the value quoted in the literature for the oxyethylene protons of PEGMA [85].

Figure 3.2.20 shows ^{1}H-^{29}Si DUMBO-LGCP dipolar correlation spectra of the P2VP/silica (a), (P2VP-PEGMA)-silica (b) and (PS-PEGMA)-silica (c) nanocomposites. Also shown (right) are the skyline projections parallel to the ^{1}H dimension from the complementary ^{1}H-^{13}C DUMBO-LGCP correlation spectra. For the P2VP/silica nanocomposite (Figure 3.2.20(a)) the Q^3 cross peak has greatest intensity in the range $\delta(^{1}H) = +4.0$ to $+8.0$ ppm. This can be compared with the corresponding spectrum of the *Nyacol 2040* silica sol in Figure 3.2.18(b) which has greatest intensity centered at +4.5 ppm. This implies that, for the nanocomposite, ^{29}Si nuclei in Q^3 sites are cross polarized by additional protons with resonances in the range $\delta = +6$ to $+ 8$ ppm. These protons can be identified by comparison with the ^{1}H skyline projection. P2VP aromatic protons are

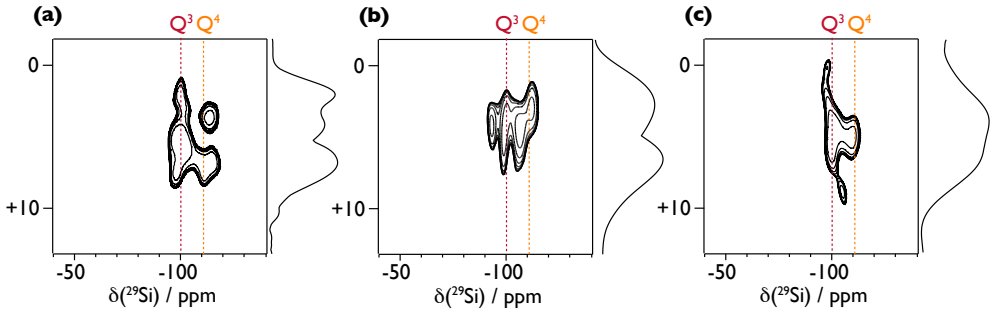

Figure 3.2.20: Two-dimensional ^{1}H-^{29}Si DUMBO-LGCP spectra of the P2VP/silica (a), (P2VP-PEGMA)-silica (b) and (PS-PEGMA)-silica (c) nanocomposites recorded using the pulse sequence in Figure 3.2.11 with LG-CP contact times of 3 ms. For each spectrum the MAS rate was 12 kHz and 1552 scans were recorded for each of 128 t_1 increments for (a), 3264 scans were recorded for each of 64 t_1 increments for (b) and 5600 scans were recorded for each of 64 t_1 increments for (c) all with a recycle delay of 1 s being inserted between scans. 100 kHz of CW decoupling was used during t_2. A dwell time of 20 μs was combined with a direct acquisition time of 20.48 ms in t_2 whilst a dwell time of 30 μs was used in t_1 giving a total indirect acquisition time of 3.84 ms for (a) and 1.92 ms for (b) and (c). Also shown (right) are skyline projections of DUMBO-LGCP ^{1}H-^{13}C dipolar correlation spectra of the same samples which show predominantly ^{1}H resonances associated with the polymer phase.

responsible for this additional cross polarization. Owing to the distance restraint enforced by using a LGCP contact time of 3 ms, it can be concluded that some pyridine protons are no more than 5 Å from Q^3 ^{29}Si nuclei in the surface of the silica particle. In addition, like the PS/silica nanocomposite of Figure 3.2.14(a), there is a significant extra cross peak between a new Q silicon site which appears between $\delta(^{29}\text{Si})$ = -100 and -111 ppm and a deshielded proton which resonates at δ = +6.5 ppm. This gives more evidence in support of the hypothesis put forward for the PS/silica nanocomposite that this unusual ^{29}Si shift is caused by the presence of a π-interaction. However, in this instance, the π-interaction is between a

silanol group and the pyridine ring in the 2VP residues. This also provides further evidence for the close proximity of the polymer side groups to the silica surface. Additionally, it is interesting to note that, unlike the P4VP/silica nanocomposites studied previously [73], there are no correlations to highly deshielded protons ($\delta \approx +10$ ppm). This indicates the absence of hydrogen bonding at the interface in this system. Hydrogen bond formation in the P4VP/silica nanocomposite system results from an interaction between the lone pair of electrons on the pyridine nitrogen and a proton in a surface silanol group (c.f. Figure 3.2.4). It is presumed that the position of the nitrogen in the pyridine ring of the 2VP residues results in a steric hindrance that prevents the formation of such a bond.

The ^{1}H-^{29}Si dipolar correlation spectrum of the (P2VP-PEGMA)-silica nanocomposite shown in Figure 3.2.20(b) is much different to the spectrum of the P2VP/silica (Figure 3.2.20(a)). This gives substantiation to the previous claim that the PEGMA is involved in the interfacial interaction. Furthermore, Figure 3.2.20(b) shows correlations between silicon-29 nuclei and protons with resonances in the range $\delta = +3$ to $+6$ ppm. Since protons in the PEGMA and protons from surface silanol groups have been shown to resonate at $\delta = +3.5$ ppm and $+4.5$ ppm, respectively, then it is these protons that are responsible for cross polarizing the silicon-29 nuclei and not protons from the P2VP. More evidence for this is from the comparison of the shape of the contours with the ^{1}H skyline projection (right) from the complementary ^{1}H-^{13}C DUMBO-LGCP spectrum. Correlations

from pyridine protons are not present. Thus, the PEGMA is responsible for the interaction at the interface with the silica sol and not the P2VP side groups.

The ^{1}H-^{29}Si dipolar correlation spectrum of the (PS-PEGMA)-silica nanocomposite given in Figure 3.2.20(c) shows an interesting system. Although the polymer latex in this nanocomposite was PEGMA-stabilised, the resulting spectrum is not similar to that of the (P2VP-PEGMA)-silica nanocomposite (Figure 3.2.20(b)). This gives a first indication that the PEGMA is not solely involved in the interfacial interaction in this case. Further indication comes from the comparison of the shape of the Q^3 cross peak with the ^{1}H skyline projection (right) from the complementary ^{1}H-^{13}C DUMBO-LGCP spectrum. It can be seen that surface silicon Q^3 sites have been cross polarized by protons with resonances in the range $\delta = +3$ to $+8$ ppm. The protons with higher δ (between $\delta = +6$ and $+8$ ppm) can be identified by comparison with the ^{1}H skyline projection as styrene aromatic protons. The protons with lower δ (between $\delta = +3$ and $+6$ ppm) can be identified by comparison with the ^{1}H-^{29}Si dipolar correlation spectrum of the *Nyacol 2040* silica sol (Figure 3.2.18(b)) as protons from silanol groups. However, this proton chemical shift range could also be attributed to protons from the PEGMA. Thus, an interaction of the PEGMA with the silica surface cannot be conclusively ruled out. Nevertheless, it must be noted that the shape of the cross peaks in the ^{1}H-^{29}Si dipolar correlation spectrum of the (PS-PEGMA)-silica nanocomposite are very similar to those from the corresponding spectrum of the

PS/silica nanocomposite studied earlier (Figure 3.2.14(a)). This would suggest that styrene side groups are closer to the Q^3 silanol sites in the silica surface than the PEGMA stabiliser and that the PEGMA does not have a role in the interfacial interaction. This is also suggested by the lack of new Q sites which appear in the corresponding spectrum of the (P2VP-PEGMA)-silica (Figure 3.2.20(b)) and are presumably a result of the interaction with the PEGMA.

Again analogous to the PS/silica nanocomposite studied earlier, there is a significant extra cross peak between a new Q silicon site which appears at δ = -104 ppm and a highly deshielded proton which resonates at δ = +9 ppm. This new Q site also produces a cross peak with a proton resonance at δ = +5 ppm. The explanation for this cross peak is that the new Q site, which is hypothesised to be induced by a π-interaction between a silanol group and the aromatic ring in the styrene residues, is cross polarized by its own silanol proton. Furthermore, the presence of this new silicon Q site in this sample indicates that it is not the AIBA initiator that is responsible for this site in the PS/silica nanocomposite studied earlier since AIBA was not used in the preparation of the (PS-PEGMA)-silica nanocomposite.

Although there is no solid-state NMR evidence for hydrogen bonding in the P2VP/silica, (P2VP-PEGMA)-silica or (PS-PEGMA)-silica nanocomposite systems, there is evidence for a π-interaction in both the P2VP/silica and (PS-

PEGMA)-silica nanocomposites. For the (P2VP-PEGMA)-silica nanocomposite there is no evidence for a π-interaction. In this nanocomposite the PEGMA is in close proximity to the silica surface to the exclusion of the 2VP residues. It is likely that the PEGMA physically adsorbs onto the silica surface, as poly(ethylene glycol) is known to do with colloidal silica [86–89], during heteroflocculation. It is possible that this physical adsorption of the PEGMA is also the driving force behind the heteroflocculation of the sterically-stabilised PS latex with the silica sol but that a more thermodynamically stable state is eventually reached where the styrene residues are interacting with the silica surface rather than the PEGMA.

3.3 Conclusions

The MAS-*J*-HMQC experiment in combination with DUMBO-1 homonuclear decoupling has been shown to be useful for recording correlation spectra with a high-resolution proton dimension. Proton-carbon-13 scalar correlations from this experiment have enabled the assignment of the proton resonances from the complicated vinylphosphonate modified nucleotide with a TBS protecting group.

However, it has also been shown that the MAS-*J*-HMQC experiment is not applicable in situations where sensitivity is a major issue or where the interactions of interest do not involve a chemical bond. The study of the interface between the inorganic and organic phases of nanocomposite materials exemplifies such

limitations.

Despite the complexity of the novel nanocomposite materials studied here, improved solid-state NMR heteronuclear dipolar correlation experiments have allowed important aspects of the adhesion between the polymer phase and the silica particles to be elucidated. In contrast to the poly(4-vinyl pyridine)/silica particles prepared from a non-functionalized aqueous sol [73], there is no direct solid-state NMR evidence for hydrogen bonding between the organic and inorganic components in any of the systems. However, polymer protons are in close proximity (< 5 Å) to Q^3 silanol sites in all the nanocomposites studied, with the exception of the (P2VP-PEGMA)-silica nanocomposite where the PEGMA protons are in close proximity to Q^3 silanol sites and no P2VP interaction is observed. For the nanocomposites produced from the *Bindzil CC40* glycerol-functionalized silica sol this indicates that either aromatic styrene or aliphatic n-butyl side groups extend between the glycerol-functional silane molecules towards the surface of the silica particles. For the P(S-co-n-BuA)/silica nanocomposite produced from the *Bindzil CC40* n-butyl acrylate residues are preferentially located at the surface of the silica particle to the exclusion of styrene residues, suggesting that there is a specific interaction between the n-butyl acrylate residues and the glycerol-functionalized silica surface. The most likely explanation is hydrogen bonding between the ester carbonyl and the glycerol functionalizing groups, although this interaction cannot be observed directly. Furthermore, for the *Bindzil CC40* glycerol-functionalized

silica sol the relative intensities of ^{29}Si NMR lines corresponding to T and Q^3 environments imply that there are approximately twice as many unreacted silanol groups on the silica surface as attached silane molecules.

For the P2VP/silica and (PS-PEGMA)-silica nanocomposites produced from the *Nyacol 2040* non-functionalized silica sol the proximity of aromatic protons to the Q^3 silanol sites indicates a π-interaction between the polymer phase and the silica particles. This is interesting in the case of the (PS-PEGMA)-silica nanocomposite since in the (P2VP-PEGMA)-silica nanocomposite the PEGMA appears to dominate the interaction.

4 Homonuclear Scalar Correlations: SAR-COSY

Homonuclear scalar correlation experiments are not frequently employed on organic samples in the solid state. However, this type of experiment, such as DQF-COSY [90], is ubiquitous in solution-state NMR. In the DQF-COSY experiment coherence is transfered between scalar-coupled nuclei via magnetization which is anti-phase with respect to the active coupling and generated in a straightforward fashion by a period of evolution under the weak-coupling Hamiltonian $2\pi J_{12}\hat{I}_{1z}\hat{I}_{2z}$. However, the resulting multiplet structure, in which components separated by the active coupling have opposing signs, causes a loss in intensity when J_{12} is within the linewidth. This is a particular problem in NMR spectroscopy of disordered solids for which the inhomogeneous contribution to the linewidth, arising for example from distributions of chemical shifts, is considerable. In such cases the ratio of the linewidth to the scalar coupling is often so large that almost complete cancellation of the cross peaks can result, as shown in Figure 4.0.1. In this figure, cross-sections of an anti-phase cross peak multiplet resulting from an arbitrary 50 Hz active coupling are given for three varying linewidths: 50 Hz (a), 250 Hz (b) and 500 Hz (c). In the solid regime (Figure 4.0.1(c)) negligible signal-to-noise is returned. Fortunately, two complementary approaches have been introduced recently which overcome this problem and allow the design of viable scalar correlation techniques for solids.

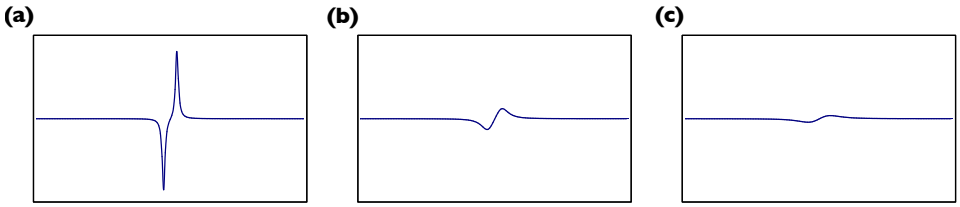

Figure 4.0.1: Cross-sections of an anti-phase cross peak multiplet resulting from an arbitrary 50 Hz active coupling with linewidths of 50 Hz (a), 250 Hz (b) and 500 Hz (c).

One of these uses the isotropic-mixing Hamiltonian $2\pi J_{12}\hat{I}_1 \cdot \hat{I}_2$ for coherence transfer and results in solid-state counterparts of the solution-state TOCSY experiment [91]. The rotor-synchronized symmetry based pulse sequence POST-C9$^1_3$ [92] utilises its generation of this isotropic-mixing Hamiltonian under MAS to achieve coherence transfer. This method has the advantage that coherence transfer occurs directly via in-phase magnetization, so that multiplet components separated by the active coupling have the same sign and cancellation is avoided. However, isotropic mixing sequences suffer from reduced transfer efficiencies arising from resonance offset effects and pulse imperfections, while extended periods of isotropic mixing can cause probe damage.

The second approach involves adapting existing solution-state experiments so that the anti-phase magnetization is refocused by an additional period of evolution under the weak-coupling Hamiltonian prior to detection in t_2. This modification results in multiplets which are in-phase with respect to the active coupling. Figure 4.0.2 shows cross-sections of an in-phase cross peak multiplet resulting

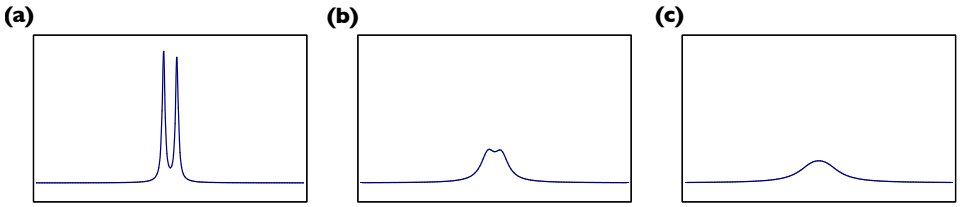

Figure 4.0.2: Cross-sections of an in-phase cross peak multiplet resulting from an arbitrary 50 Hz active coupling with linewidths of 50 Hz (a), 250 Hz (b) and 500 Hz (c).

from an arbitrary 50 Hz active coupling with linewidths of 50 Hz (a), 250 Hz (b) and 500 Hz (c). It can be clearly noted that in the solid regime (Figure 4.0.2(c)) there is still a significant signal-to-noise ratio. Despite the addition of an extra delay, such experiments can result in substantial gains in sensitivity over their non-refocused antecedents when the inhomogeneous contribution to the linewidth dominates. This is because the corresponding magnetization decay can be reversed by a π pulse inserted at the midpoint of the refocusing delay. It has been shown [93, 94] that the sensitivity gain obtained with the refocused variant of a particular scalar correlation pulse sequence is determined by two factors. The first is the ratio T_2'/T_2^* of the time constants associated with the homogeneous linewidth which cannot be refocused by a π pulse and the apparent linewidth which includes the inhomogeneous contribution, respectively. The second is the reduced coupling constant $\pi J_{12} T_2^*$ which measures the extent to which the active coupling is resolved. A widely established example of this approach is the refocused INADEQUATE (r-INADEQUATE) experiment [93] which is derived

from the eponymous solution-state double-quantum correlation pulse sequence [95]. Many applications of this experiment have been demonstrated, including conformational studies of spider dragline silk [96], structural investigations of crystalline and disordered phosphates [97] and the direct detection of hydrogen bonds [98].

Recently, a new refocused scalar correlation experiment suitable for solids, named UC2QF-COSY, was described [94, 99]. This method retains the straightforward single-quantum shift correlation format of DQF-COSY, while benefiting from the sensitivity gains associated with in-phase multiplets in common with r-INADEQUATE. An improved scalar correlation experiment which has some advantages over UC2QF-COSY, including a doubling of intensity for the cross peaks coupled with good suppression of the uninformative diagonal, is presented here. For convenience the new experiment is referred to as SAR-COSY (for Sensitive, Absorptive, Refocused COSY). The advantages mentioned above make SAR-COSY ideal for recording scalar correlation spectra for nuclei at low natural abundance or for samples with large inhomogeneous linewidths. It should be noted that a constant-time variant [100, 101] of UC2QF-COSY has also been proposed which results in even larger gains in cross peak intensity, particularly in uniformly labelled systems. However, these gains are achieved in exchange for loss of the ability to suppress the natural abundance background which means that this experiment is not appropriate for the systems studied here.

4.1 SAR-COSY Pulse Sequence

The SAR-COSY pulse sequence, which is shown in Figure 4.1.1, is based on the solution-state ISECR-COSY experiment of Talluri and Scheraga [102]. Carbon-13 magnetization generated by cross polarization evolves under the scalar coupling Hamiltonian during a preparation delay of total duration 2τ. Evolution under the isotropic part of the chemical shift is refocused by a π pulse which occurs at the midpoint of this delay. In principle full refocusing is only achieved when τ is equal to an integral number of rotor periods but in practice this synchronization is not required at high MAS rates. The resulting magnetization is passed through a double-quantum filter (DQF) before the t_1 evolution period. After the t_1 period a $\pi/2$ pulse transfers the magnetization between pairs of scalar-coupled spins. A further refocusing 2τ delay and π pulse are combined with a z-filter (ZF) and inserted before the acquisition period. Heteronuclear decoupling is applied during the whole of the sequence after the cross polarization step, except for during the ZF delay. Numerous phase cycles which select the required coherence transfer pathway (shown in red in Figure 4.1.1) can be designed based on the principles described by Bodenhausen et al. [6]. In principle, the full cycle for the carbon-13 pulses excludes coherences of order $p = 0, \pm 1$ during the DQF and $p \neq 0$ during the ZF and selects a change in order $\Delta p = \pm 2$ for each π pulse. In practice, this procedure requires co-adding a prohibitively large number of experimental repetitions, resulting in overly long two-dimensional experiments.

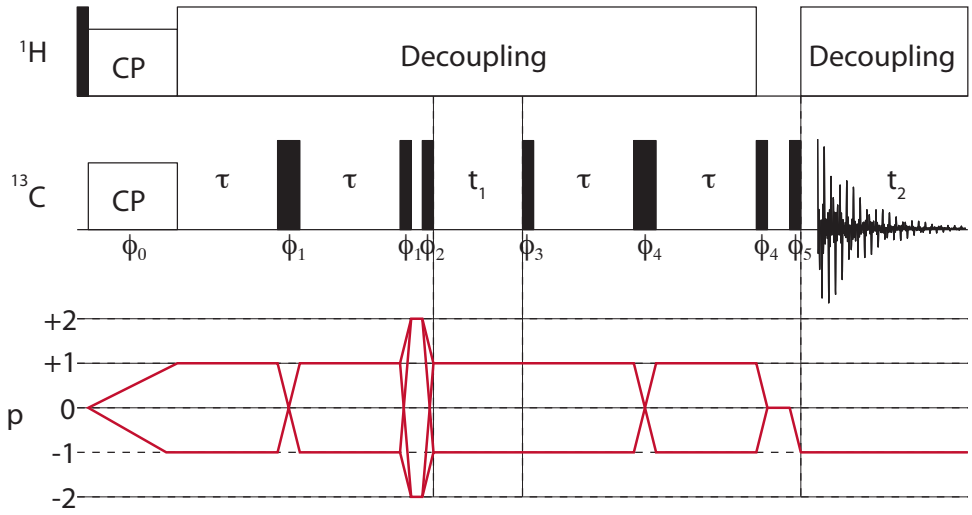

Figure 4.1.1: Pulse sequence used to record SAR-COSY scalar correlation spectra. Narrow and wide filled vertical bars represent $\pi/2$ and π pulses, respectively. The phase of each pulse is represented by ϕ_n and these phases correspond to the phase cycle given in Table 4.1.1.

As an alternative, the coherence transfer pathway can be selected by the use of pulse field gradients [94] or a reduced phase cycle. One possibility for the latter is given in Ref. [102] and is reproduced in Table 4.1.1.

4.2 Product Operator Analysis of SAR-COSY

A thorough understanding of the SAR-COSY experiment can be obtained from a product operator analysis (c.f. Section 1.2.11). This analysis will allow a convenient visualization of the expected acquired signal. For completeness the method

Table 4.1.1: Phase cycle and corresponding receiver phase for the SAR-COSY pulse sequence. All the phases are in degrees.

Step	ϕ_0	ϕ_1	ϕ_2	ϕ_3	ϕ_4	ϕ_5	receiver phase
1	90	0	0	90	0	0	0
2	90	0	0	90	0	90	90
3	90	0	0	90	0	180	180
4	90	0	0	90	0	270	270
5	90	0	0	270	0	0	0
6	90	0	0	270	0	90	90
7	90	0	0	270	0	180	180
8	90	0	0	270	0	270	270
9	90	0	90	0	90	0	180
10	90	0	90	0	90	90	270
11	90	0	90	0	90	180	0
12	90	0	90	0	90	270	90
13	90	0	90	180	90	0	180
14	90	0	90	180	90	90	270
15	90	0	90	180	90	180	0
16	90	0	90	180	90	270	90
17	90	0	180	90	0	0	180
18	90	0	180	90	0	90	270
19	90	0	180	90	0	180	0
20	90	0	180	90	0	270	90
21	90	0	180	270	0	0	180
22	90	0	180	270	0	90	270
23	90	0	180	270	0	180	0
24	90	0	180	270	0	270	90
25	90	0	270	0	90	0	0
26	90	0	270	0	90	90	90
27	90	0	270	0	90	180	180
28	90	0	270	0	90	270	270
29	90	0	270	180	90	0	0
30	90	0	270	180	90	90	90
31	90	0	270	180	90	180	180
32	90	0	270	180	90	270	270

is detailed below in its entirety.

Assuming a two spin system, which is initially at thermal equilibrium, i.e $\rho(0) = \hat{I}_{1z} + \hat{I}_{2z}$, a product operator treatment is applied to the pulse sequence given in Figure 4.1.1. Starting with an assumed RF pulse of flip angle $\pi/2$ along the x-axis

$$\hat{I}_{1z} + \hat{I}_{2z} \xrightarrow{(\pi/2)(\hat{I}_{1x}+\hat{I}_{2x})} -\hat{I}_{1y} - \hat{I}_{2y} \tag{4.2.1}$$

A spin echo sequence of duration 2τ is then applied

$$\xrightarrow{4\pi J_{12}\tau \hat{I}_{1z}\hat{I}_{2z}} \quad -\cos(2\pi J_{12}\tau)\hat{I}_{1y} + \sin(2\pi J_{12}\tau)2\hat{I}_{1x}\hat{I}_{2z}$$
$$-\cos(2\pi J_{12}\tau)\hat{I}_{2y} + \sin(2\pi J_{12}\tau)2\hat{I}_{1z}\hat{I}_{2x} \qquad (4.2.2)$$

$$\xrightarrow{\pi(\hat{I}_{1x}+\hat{I}_{2x})} \quad \cos(2\pi J_{12}\tau)\hat{I}_{1y} - \sin(2\pi J_{12}\tau)2\hat{I}_{1x}\hat{I}_{2z} +$$
$$\cos(2\pi J_{12}\tau)\hat{I}_{2y} - \sin(2\pi J_{12}\tau)2\hat{I}_{1z}\hat{I}_{2x} \qquad (4.2.3)$$

Next is the first pulse (a $\pi/2$ pulse along x) of the DQF

$$\xrightarrow{(\pi/2)(\hat{I}_{1x}+\hat{I}_{2x})} \quad \cos(2\pi J_{12}\tau)\hat{I}_{1z} + \sin(2\pi J_{12}\tau)2\hat{I}_{1x}\hat{I}_{2y} +$$
$$\cos(2\pi J_{12}\tau)\hat{I}_{2z} + \sin(2\pi J_{12}\tau)2\hat{I}_{1y}\hat{I}_{2x} \qquad (4.2.4)$$

A DQF only allows double quantum coherence to pass (c.f. Table 1.2.4) $\Longrightarrow$

$$\text{equation (4.2.4)} \rightarrow \sin(2\pi J_{12}\tau)2\hat{I}_{1x}\hat{I}_{2y} + \sin(2\pi J_{12}\tau)2\hat{I}_{1y}\hat{I}_{2x} \qquad (4.2.5)$$

Since,

$$2\hat{I}_{1x}\hat{I}_{2y} = \frac{1}{2}(2\hat{I}_{1x}\hat{I}_{2y} + 2\hat{I}_{1y}\hat{I}_{2x}) - \frac{1}{2}(2\hat{I}_{1y}\hat{I}_{2x} - 2\hat{I}_{1x}\hat{I}_{2y}) \qquad (4.2.6)$$

and

$$2\hat{I}_{1y}\hat{I}_{2x} = \frac{1}{2}(2\hat{I}_{1x}\hat{I}_{2y} + 2\hat{I}_{1y}\hat{I}_{2x}) + \frac{1}{2}(2\hat{I}_{1y}\hat{I}_{2x} - 2\hat{I}_{1x}\hat{I}_{2y}) \qquad (4.2.7)$$

where $(2\hat{I}_{1y}\hat{I}_{2x} - 2\hat{I}_{1x}\hat{I}_{2y})$ is zero quantum coherence and therefore does not pass through the DQF, then after the second $\pi/2$ pulse along x of the DQF the resultant magnetization is

$$\text{equation (4.2.5)} \xrightarrow{(\pi/2)(\hat{I}_{1x}+\hat{I}_{2x})} S_{12}(\hat{I}_{1x}\hat{I}_{2z} + \hat{I}_{1z}\hat{I}_{2x}) + S_{12}(\hat{I}_{1x}\hat{I}_{2z} + \hat{I}_{1z}\hat{I}_{2x}) = S_{12}(2\hat{I}_{1x}\hat{I}_{2z} + 2\hat{I}_{1z}\hat{I}_{2x}) \quad (4.2.8)$$

where $S_{12} = \sin(2\pi J_{12}\tau)$. The spin system is then allowed to evolve during the t_1 period

$$\text{equation (4.2.8)} \xrightarrow{\Omega_1 t_1 \hat{I}_{1z}} S_{12}\cos(\Omega_1 t_1)2\hat{I}_{1x}\hat{I}_{2z} + S_{12}\sin(\Omega_1 t_1)2\hat{I}_{1y}\hat{I}_{2z} + S_{12}2\hat{I}_{1z}\hat{I}_{2x} \quad (4.2.9)$$

$$\xrightarrow{\Omega_2 t_1 \hat{I}_{2z}} S_{12}\cos(\Omega_1 t_1)2\hat{I}_{1x}\hat{I}_{2z} + S_{12}\sin(\Omega_1 t_1)2\hat{I}_{1y}\hat{I}_{2z} + S_{12}\cos(\Omega_2 t_1)2\hat{I}_{1z}\hat{I}_{2x} + S_{12}\sin(\Omega_2 t_1)2\hat{I}_{1z}\hat{I}_{2y} \quad (4.2.10)$$

$$\xrightarrow{2\pi J_{12} t_1(\hat{I}_{1z}+\hat{I}_{2z})} S_{12}\cos(\Omega_1 t_1)[\alpha_{12}2\hat{I}_{1x}\hat{I}_{2z} + \beta_{12}\hat{I}_{1y}] + S_{12}\sin(\Omega_1 t_1)[\alpha_{12}2\hat{I}_{1y}\hat{I}_{2z} - \beta_{12}\hat{I}_{1x}] + S_{12}\cos(\Omega_2 t_1)[\alpha_{12}2\hat{I}_{1z}\hat{I}_{2x} + \beta_{12}\hat{I}_{2y}] + S_{12}\sin(\Omega_2 t_1)[\alpha_{12}2\hat{I}_{1z}\hat{I}_{2y} - \beta_{12}\hat{I}_{2x}] \quad (4.2.11)$$

where $\alpha_{12} = \cos(\pi J_{12} t_1)$ and $\beta = \sin(\pi J_{12} t_1)$, before a $\pi/2$ pulse is applied along y to transfer magnetization between the two spins

$$\begin{aligned} \text{equation (4.2.11)} \xrightarrow{(\pi/2)(\hat{I}_{1y}+\hat{I}_{2y})} \quad & S_{12}\cos(\Omega_1 t_1)[-\alpha_{12} 2\hat{I}_{1z}\hat{I}_{2x} + \beta_{12}\hat{I}_{1y}] + \\ & S_{12}\sin(\Omega_1 t_1)[\alpha_{12} 2\hat{I}_{1y}\hat{I}_{2x} + \beta_{12}\hat{I}_{1z}] + \\ & S_{12}\cos(\Omega_2 t_1)[-\alpha_{12} 2\hat{I}_{1x}\hat{I}_{2z} + \beta_{12}\hat{I}_{2y}] + \\ & S_{12}\sin(\Omega_2 t_1)[\alpha_{12} 2\hat{I}_{1x}\hat{I}_{2y} + \beta_{12}\hat{I}_{2z}] \end{aligned} \quad (4.2.12)$$

Lines 1 and 3 of equation (4.2.12) represent magnetization transfer whereas lines 2 and 4 represent combinations of zero and double quantum magnetization, which are removed in the phase cycling $\Longrightarrow$

$$\begin{aligned} \text{equation (4.2.12)} \rightarrow \quad & S_{12}\cos(\Omega_1 t_1)[-\alpha_{12} 2\hat{I}_{1z}\hat{I}_{2x} + \beta_{12}\hat{I}_{1y}] + \\ & S_{12}\cos(\Omega_2 t_1)[-\alpha_{12} 2\hat{I}_{1x}\hat{I}_{2z} + \beta_{12}\hat{I}_{2y}] \end{aligned} \quad (4.2.13)$$

Following the magnetization transfer, a second spin echo period is applied

$$\begin{aligned} \xrightarrow{4\pi J_{12}\tau(\hat{I}_{1z}+\hat{I}_{2z})} \quad & S_{12}\cos(\Omega_1 t_1)[-\alpha_{12}\{C_{12} 2\hat{I}_{1z}\hat{I}_{2x} + S_{12}\hat{I}_{2y}\} + \\ & \beta_{12}\{C_{12}\hat{I}_{1y} - S_{12} 2\hat{I}_{1x}\hat{I}_{2z}\}] + \\ & S_{12}\cos(\Omega_2 t_1)[-\alpha_{12}\{C_{12} 2\hat{I}_{1x}\hat{I}_{2z} + S_{12}\hat{I}_{1y}\} + \\ & \beta_{12}\{C_{12}\hat{I}_{2y} - S_{12} 2\hat{I}_{1z}\hat{I}_{2x}\}] \end{aligned} \quad (4.2.14)$$

where $C_{12} = \cos(2\pi J_{12}\tau)$

$$\text{equation (4.2.14)} \xrightarrow{\pi(\hat{I}_{1x}+\hat{I}_{2x})} \quad S_{12}\cos(\Omega_1 t_1)[\alpha_{12}\{C_{12}2\hat{I}_{1z}\hat{I}_{2x} + S_{12}\hat{I}_{2y}\} + \beta_{12}\{S_{12}2\hat{I}_{1x}\hat{I}_{2z} - C_{12}\hat{I}_{1y}\}] + S_{12}\cos(\Omega_2 t_1)[\alpha_{12}\{C_{12}2\hat{I}_{1x}\hat{I}_{2z} + S_{12}\hat{I}_{1y}\} + \beta_{12}\{S_{12}2\hat{I}_{1z}\hat{I}_{2x} - C_{12}\hat{I}_{2y}\}] \tag{4.2.15}$$

The final part of the pulse sequence is the ZF. The first pulse of the ZF is a $\pi/2$ x-pulse.

$$\xrightarrow{(\pi/2)(\hat{I}_{1x}+\hat{I}_{2x})} \quad S_{12}\cos(\Omega_1 t_1)[\alpha_{12}\{-C_{12}2\hat{I}_{1y}\hat{I}_{2x} + S_{12}\hat{I}_{2z}\} + \beta_{12}\{-S_{12}2\hat{I}_{1x}\hat{I}_{2y} - C_{12}\hat{I}_{1z}\}] + S_{12}\cos(\Omega_2 t_1)[\alpha_{12}\{-C_{12}2\hat{I}_{1x}\hat{I}_{2y} + S_{12}\hat{I}_{1z}\} + \beta_{12}\{-S_{12}2\hat{I}_{1y}\hat{I}_{2x} - C_{12}\hat{I}_{2z}\}] \tag{4.2.16}$$

Coherence except that of order zero is eliminated by the phase cycling of the ZF. The $2\hat{I}_x\hat{I}_y$ and $2\hat{I}_y\hat{I}_x$ terms of equation (4.2.16) are mixtures of DQ and ZQ coherences. Thus, the ZQ parts will pass through the ZF. These ZQ parts will be ignored for now and will be discussed later. Accordingly, after the second pulse

of the ZF, a $\pi/2$ pulse along $-x$, the resulting density operator at time $t_2 = 0$ is

$$\begin{aligned} \text{equation (4.2.16)} \xrightarrow{(\pi/2)(\hat{I}_{1(-x)}+\hat{I}_{2(-x)})} \quad & S_{12}\cos(\Omega_1 t_1)[\alpha_{12}\{S_{12}\hat{I}_{2y}\} + \\ & \beta_{12}\{-C_{12}\hat{I}_{1y}\}] + \\ & S_{12}\cos(\Omega_2 t_1)[\alpha_{12}\{S_{12}\hat{I}_{1y}\} + \\ & \beta_{12}\{-C_{12}\hat{I}_{2y}\}] \end{aligned} \tag{4.2.17}$$

$$\begin{aligned} = \quad & \sin^2(2\pi J_{12}\tau)\cos(\pi J_{12}t_1)[\cos(\Omega_1 t_1)\hat{I}_{2y} + \cos(\Omega_2 t_1)\hat{I}_{1y}] \\ & -\sin(2\pi J_{12}\tau)\cos(2\pi J_{12}\tau)\sin(\pi J_{12}t_1) \times \\ & [\cos(\Omega_1 t_1)\hat{I}_{1y} + \cos(\Omega_2 t_1)\hat{I}_{2y}] \end{aligned} \tag{4.2.18}$$

It can be seen from equation (4.2.18) that the cross peaks are in-phase and absorptive in both dimensions:

$$\sin^2(2\pi J_{12}\tau)\cos(\pi J_{12}t_1)[\cos(\Omega_1 t_1)\hat{I}_{2y} + \cos(\Omega_2 t_1)\hat{I}_{1y}] \tag{4.2.19}$$

and that the diagonal peaks are in-phase and absorptive in the ω_2 dimension but anti-phase and dispersive in the ω_1 dimension:

$$-\sin(2\pi J_{12}\tau)\cos(2\pi J_{12}\tau)\sin(\pi J_{12}t_1)[\cos(\Omega_1 t_1)\hat{I}_{1y} + \cos(\Omega_2 t_1)\hat{I}_{2y}] \tag{4.2.20}$$

It should be pointed out that the in-phase and absorptive nature of the cross peaks is what is desired to prevent intensity losses when the coupling is smaller than the linewidth, as is usually the case in disordered solids. It is also worth noting that the anti-phase multiplet structure in ω_1 of the diagonal peaks typically results in their partial cancellation when the coupling is smaller than the linewidth. This is beneficial because suppression of the diagonal peaks will improve the resolution of cross peaks close to the diagonal in crowded spectra.

During the ZF, ZQ coherence was ignored. The second pulse of the ZF transforms the ZQ coherence into anti-phase x-magnetization. As shown previously, an anti-phase multiplet structure results in intensity losses when the active coupling is within the linewidth, as is usually the case for solids. Hence, negligible intensity would be returned from the ZQ coherence that passes through the ZF and therefore it was disregarded.

A similar product operator analysis can be performed on the UC2QF-COSY experiment and gives the density operator at time $t_2 = 0$ to be

$$\begin{aligned}&\frac{1}{2}\sin^2(2\pi J_{12}\tau)\cos(\pi J_{12}t_1)[\cos(\Omega_1 t_1)\hat{I}_{2y} + \cos(\Omega_2 t_1)\hat{I}_{1y}] \\ &+\frac{1}{2}\sin^2(2\pi J_{12}\tau)\cos(\pi J_{12}t_1)[\cos(\Omega_1 t_1)\hat{I}_{1y} + \cos(\Omega_2 t_1)\hat{I}_{2y}] \qquad (4.2.21)\end{aligned}$$

The first term shows identical cross peaks to those obtained from SAR-COSY

except for a halving of the amplitude. The second term shows that the resulting diagonal peaks have the same phase and multiplet structure as the cross peaks. This can cause problems when poorly resolved cross peaks are close to the diagonal since the cross peaks may become indistinguishable from diagonal peaks.

The intensity of the cross peaks and the diagonal peaks resulting from a SAR-COSY experiment are plotted as a function of τ in Figure 4.2.1. Figure 4.2.1(a) demonstrates that, for a scalar coupling of $J_{12} = 50$ Hz and neglecting relaxation effects, maximum cross peak intensity (blue) is returned when using a τ delay of 5 ms. This corresponds to a refocusing delay, 2τ, of 10 ms. Using $\tau = 5$ ms results in zero intensity for the diagonal peaks (orange). In practice, relaxation effects will always be present. Figure 4.2.1(b) shows that when relaxation effects are included maximum cross peak intensity (blue) is achieved somewhat below 5 ms. Selecting for maximum cross peak intensity in this case would result in negative diagonal intensity (orange). Negative diagonal intensity helps to further distinguish cross peaks from diagonal peaks.

4.3 Sensitivity Comparison of SAR-COSY

Firstly, *SPINEVOLUTION* [103] simulations were performed on universally carbon-13 labelled (U-^{13}C) DL-alanine (c.f. Figure 2.2.3) in the solid state for various COSY-type experiments with identical parameters so as to obtain a sensitivity

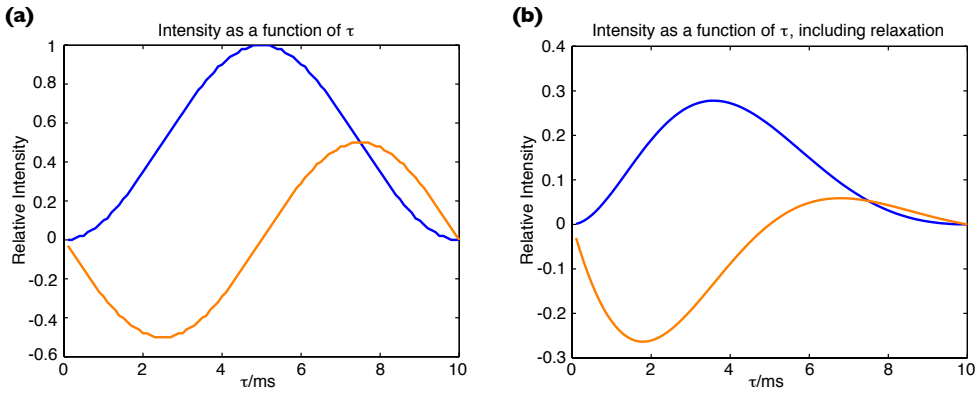

Figure 4.2.1: Intensity of the cross (blue) and diagonal (orange) peaks resulting from a SAR-COSY experiment as a function of τ, neglecting (a) and including (b) relaxation effects. A scalar coupling of $J_{12} = 50$ Hz was used for both and a decay constant of 12.5 ms was used to simulate relaxation in (b).

comparison between each. An example *SPINEVOLUTION* input file is given in Appendix I. Figure 4.3.1 shows cross sections parallel to ω_2 taken from the simulated two-dimensional datasets of SAR-COSY (a), UC2QF-COSY (b) and DQF-COSY (c). It is clear to note that the DQF-COSY cross sections (Figure 4.3.1(c)) exhibit the well-known anti-phase multiplet structure. What is more pertinent is that these cross sections have had their intensities multiplied by one order of magnitude so that they are observable. This instantly illustrates the necessity of utilising refocused COSY-type experiments for solid-state studies. It is also clear to note that the cross peaks resulting from the SAR-COSY simulation (Figure 4.3.1(a)) have twice the intensity compared to their simulated UC2QF-COSY counterparts (Figure 4.3.1(b)). What is less evident, but nonetheless present, is the existence of *relay* cross peaks in the SAR-COSY simulation. These are due

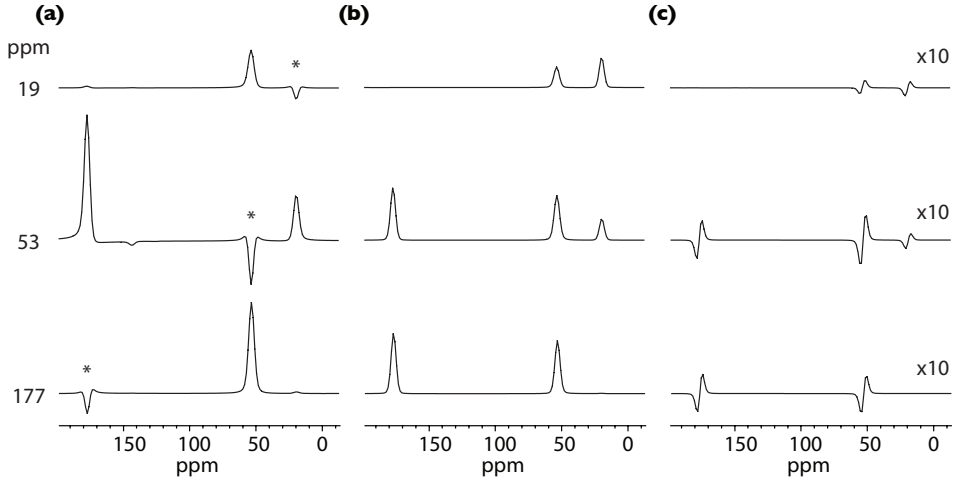

Figure 4.3.1: Cross sections parallel to ω_2 taken from *SPINEVOLUTION* [103] simulations on solid-state U-^{13}C DL-alanine for SAR-COSY (a), UC2QF-COSY (b) and DQF-COSY (c). Diagonal peaks are identified in (a) with asterisks. The δ values (left) indicate the chemical shift at which the cross section is taken from ω_1. The intensity of the DQF-COSY cross sections (c) has been multiplied by a factor of 10 so that the peaks are made apparent.

to a two-step coherence transfer process where transfer of magnetization occurs in a multi-spin system from one spin that is not directly coupled to the second spin but shares a mutual coupling partner. For the example of U-^{13}C DL-alanine, relay cross peaks can be seen (Figure 4.3.1(a)) between the β-carbon (δ = 17 ppm) and the carbonyl carbon (δ = 177 ppm). These nuclei have a negligible scalar coupling but share the α-carbon as a mutual coupling partner.

Secondly, experimental studies were performed to compare the sensitivity of the SAR-COSY experiment and its contemporaries. The pulse sequence used to record SAR-COSY spectra is that from Figure 4.1.1 and a time of 3 μs was consistently used for the ZF delay. Pure phase two-dimensional lineshapes were

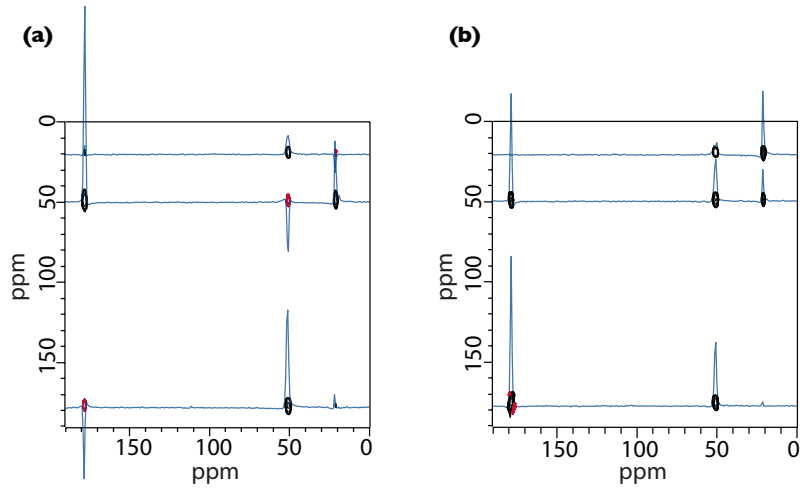

Figure 4.3.2: SAR-COSY (a) and UC2QF-COSY (b) experiments on U-^{13}C DL-alanine. The experimental parameters were identical for both (a) and (b). A *Varian* 3.2 mm double-resonance MAS probe was employed at a carbon-13 Larmor frequency of 75.47 MHz and a MAS rate of 17.6 kHz. 64 scans were recorded for each of 256 t_1 increments with a recycle delay of 1 s. A dwell time of 20.0 μs was combined with a direct acquisition time of 20.48 ms in t_2 whilst a dwell time of 10.0 μs was used in t_1 resulting in a total indirect acquisition time of 2.6 ms. The refocusing delay, 2τ, was 4 ms and 150 kHz of CW heteronuclear decoupling was used. In the two-dimensional spectra black contours have positive intensity and red contours have negative intensity. Cross sections parallel to ω_2 are shown in blue.

obtained using TPPI.

Figure 4.3.2 compares the SAR-COSY (a) and UC2QF-COSY (b) spectra of U-^{13}C DL-alanine[19]. Note that a DQF-COSY spectrum was not recorded due to the signal-to-noise limitations of this technique for studies on most solid samples. As expected from the product operator analyses and the simulation data, the cross peaks resulting from the SAR-COSY experiment have approximately twice the intensity of the corresponding cross peaks from the UC2QF-COSY experiment.

[19]U-^{13}C DL-alanine was purchased from *Isotec Inc.* with an isotopic purity of 99 %.

This is confirmed from the cross sections taken parallel to the ω_2 dimension at the resonances of the cross peaks (shown in blue). Using a τ delay of 2 ms (refocusing delay, 2τ, of 4 ms) results in diagonal peaks that are negative (shown in red) in the SAR-COSY spectrum (Figure 4.3.2(a)) but positive in the UC2QF-COSY spectrum (Figure 4.3.2(b)). This is, again, expected from the results of the corresponding product operator analyses. Another point of note is that the relay cross peaks that were predicted in the simulation data also appear in the experimental data for the SAR-COSY spectrum. Furthermore, these relay cross peaks also appear in the UC2QF-COSY spectrum, if at somewhat lesser intensity.

The other solid-state contemporary of SAR-COSY, r-INADEQUATE [93], contains an identical sensitivity factor ($sin^2(2\pi J_{12}\tau)$) for the cross peaks. Thus, to this level of approximation, the sensitivities of SAR-COSY and r-INADEQUATE should be comparable. However, different coherences evolve during t_1 for the two experiments. As a result, if the active coupling is resolved ($\pi J_{12}T_2^* > 1$), the SAR-COSY cross peaks are split into a doublet in ω_1, resulting in a two-fold loss of signal relative to r-INADEQUATE. However, in this regime a non-refocused experiment is more appropriate anyway. Similarly, for the multi-spin systems which dominate at higher abundance, the refocused INADEQUATE cross peaks are broadened in ω_1 by unresolved passive couplings to both the spins involved in the DQ coherence. The SAR-COSY cross peaks are broadened by just one set of unresolved passive couplings, but this is in addition to the active coupling already

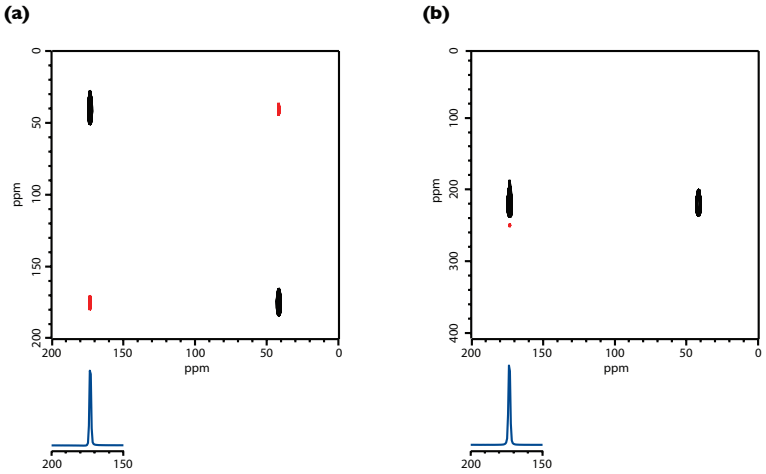

Figure 4.3.3: SAR-COSY (a) and zfr-INADEQUATE (b) experiments on glycine-2-^{13}C-^{15}N. The experimental parameters were almost identical for both (a) and (b). A *Varian* 4 mm double-resonance MAS probe was employed at a carbon-13 Larmor frequency of 75.47 MHz and a MAS rate of 12.0 kHz. 128 scans were recorded for each of 128 t_1 increments with a recycle delay of 1 s. A dwell time of 20.0 μs was combined with a direct acquisition time of 20.48 ms in t_2 for both whilst dwell times of 10.0 μs (a) and 5.0 μs (b) were used in t_1 resulting in total indirect acquisition times of 1.3 ms and 0.7 ms, respectively. Half the dwell time in t_1 was used for (b) as a result of DQ magnetization evolving during this time so that comparable data to (a) was produced. The refocusing delay, 2τ, was 4 ms and 100 kHz of CW heteronuclear decoupling was used. In the two-dimensional spectra black contours have positive intensity and red contours have negative intensity. Cross sections parallel to ω_2 of the cross peak at $\delta(\omega_2) = 173$ ppm are shown in blue beneath the two-dimensional spectra and are used as a sensitivity comparison.

mentioned. Hence, in the solids regime when the couplings are unresolved the sensitivity of SAR-COSY and INADEQUATE is roughly equivalent.

The addition of a z-filter has been shown to be effective at suppressing undesired contributions to r-INADEQUATE spectra [104]. These undesired contributions consist of artifacts that are capable of distorting lineshapes and also producing

peaks that could be misinterpreted as correlation peaks. The z-filtered refocused (zfr-) INADEQUATE experiment is compared to SAR-COSY in Figure 4.3.3. This figure shows two spectra, recorded using equivalent parameters, of glycine-2-^{13}C-^{15}N (c.f. Figure 2.4.1). Figure 4.3.3(a) is the SAR-COSY spectrum and Figure 4.3.3(b) is the zfr-INADEQUATE spectrum with its DQ-SQ correlation format. Also shown (in blue) are cross sections parallel to ω_2 of the cross peak at chemical shift $\delta(\omega_2) = 173$ ppm. These cross sections show that SAR-COSY results in approximately equal sensitivity when compared to zfr-INADEQUATE. This conclusion has been supported by further cross peak comparisons from SAR-COSY and zfr-INADEQUATE spectra on various other samples (not shown).

4.4 Demonstration of SAR-COSY

To demonstrate the utility of diagonal peak suppression with SAR-COSY a spectrum of U-^{13}C L-tyrosine.HCl[20] was recorded. This spectrum is given in Figure 4.4.1. In the crowded aromatic region of the spectrum between $\delta = 100$ and 150 ppm the positive cross peaks are well resolved (black contours), while the negative diagonal (red contours) is virtually absent. This effect of self-cancellation of the diagonal is more pronounced for poorly resolved spectra where diagonal cancellation is important.

[20]U-^{13}C L-tyrosine.HCl was purchased from *Aldrich Chem. Co.* with an isotopic purity of 99 %

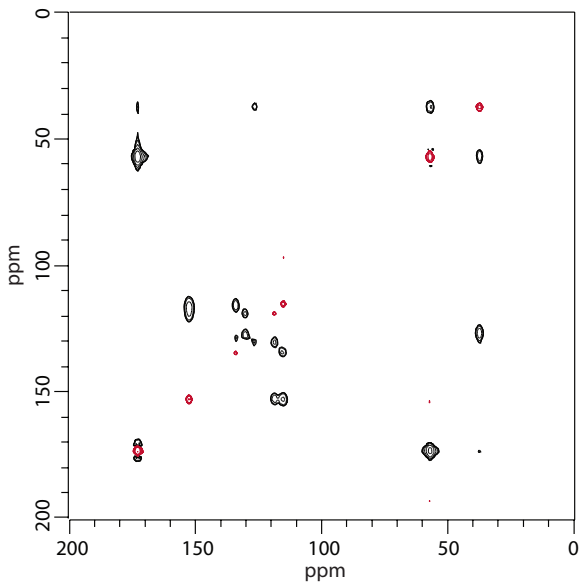

Figure 4.4.1: SAR-COSY spectrum of U-^{13}C L-tyrosine.HCl. A *Varian* 3.2 mm double-resonance MAS probe was employed at a carbon-13 Larmor frequency of 75.47 MHz and a MAS rate of 17.0 kHz. 64 scans were recorded for each of 512 t_1 increments with a recycle delay of 1 s. A dwell time of 20.0 μs was combined with a direct acquisition time of 20.48 ms in t_2 whilst a dwell time of 10.0 μs was used in t_1 resulting in a total indirect acquisition time of 5.2 ms. The refocusing delay, 2τ, was 4 ms and 150 kHz of CW heteronuclear decoupling was used. Black contours have positive intensity and red contours have negative intensity.

Comment should be made on the presence of relay cross peaks in this spectrum. Low intensity "cross peaks" are observed at (38,173) and (173,38), to use the notation described earlier. These peaks are assigned to a coupling between carbon 3 and carbon 1 (c.f. Figure 2.4.4) of the L-tyrosine.HCl. These carbons are not directly bonded and therefore have a negligible scalar coupling but they do share a mutual coupling partner; carbon 2. The *Relay-COSY* experiment [105] sets out to purposefully obtain relayed cross peaks to aid in molecular structure determination. In this experiment a refocusing period and an extra $\pi/2$ pulse are

used after the traditional COSY sequence to attain the desired coherence transfer via the following scheme:

$$
\begin{aligned}
&\hat{I}_{1z} + \hat{I}_{2z} + \hat{I}_{3z} \\
&\qquad \xrightarrow{t_1 \text{ period}} (\Omega_1 t_1)(2\hat{I}_{1x}\hat{I}_{2z}) + (\Omega_3 t_1)(2\hat{I}_{3x}\hat{I}_{2z}) \\
&\qquad \xrightarrow{\text{magnetization transfer}} (\Omega_1 t_1)(2\hat{I}_{1z}\hat{I}_{2x}) + (\Omega_3 t_1)(2\hat{I}_{3z}\hat{I}_{2x}) \\
&\qquad \xrightarrow{\text{evolution under } J_{12} \text{ and } J_{23}} (\Omega_1 t_1)(2\hat{I}_{2x}\hat{I}_{3z}) + (\Omega_3 t_1)(2\hat{I}_{1z}\hat{I}_{2x}) \\
&\qquad \xrightarrow{\text{magnetization transfer}} (\Omega_1 t_1)(2\hat{I}_{2z}\hat{I}_{3x}) + (\Omega_3 t_1)(2\hat{I}_{1x}\hat{I}_{2z}) \\
&\qquad \xrightarrow{t_2 \text{ period}} (\Omega_1 t_1)(\Omega_3 t_2) + (\Omega_3 t_1)(\Omega_1 t_2) \qquad (4.4.1)
\end{aligned}
$$

Note that this is only the form of the scheme and that many terms have been omitted; the omitted terms are not relevant for the purposes of this illustration.

It can be seen that "cross peaks" will be produced that appear at (Ω_1, Ω_3) and (Ω_3, Ω_1) even though there is no direct J_{13} coupling. However, it can also be seen that the presence of a mutual coupling partner (in this case I_2) is required.

A similar sequence to that of Relay-COSY after the t_1 period is employed in the SAR-COSY experiment. Thus, SAR-COSY will result in relayed cross peaks that have been produced by the same mechanism. In the SAR-COSY spectrum of U-^{13}C L-tyrosine.HCl carbon 2 acts as the mediator for coherence transfer between

carbon 1 and carbon 3 and the magnetization follows the scheme above.

4.5 Application of SAR-COSY to Natural Abundance Samples

Sensitivity is a major issue with carbon-13 scalar correlation spectroscopy. Furthermore, at natural abundance the probability of obtaining a carbon-13 spin pair is 0.0001. This is four orders of magnitude less than U-^{13}C samples. However, UC2QF-COSY has been shown to perform well on natural abundance samples of tyrosine [94] and crystalline vitamin D_3 [99]. For the latter, UC2QF-COSY was used to assign the 54 carbon-13 resonances which result from the two inequivalent conformations in the unit cell. The superior sensitivity of SAR-COSY relative to UC2QF-COSY makes larger molecules tractable, as well as samples with unfavourably long relaxation times.

In order to record homonuclear carbon-13 scalar correlation spectra of solid samples within realistic time constraints, maximum signal-to-noise must be achieved. Consequently, all parameters need to be calibrated fully. Once the pulses have been calibrated, the lengths of the delays are then also required. For a SAR-COSY spectrum of natural abundance L-tyrosine.HCl, the length of the refocusing delays presents the largest threat to signal-to-noise. As shown in Figure 4.2.1(b)

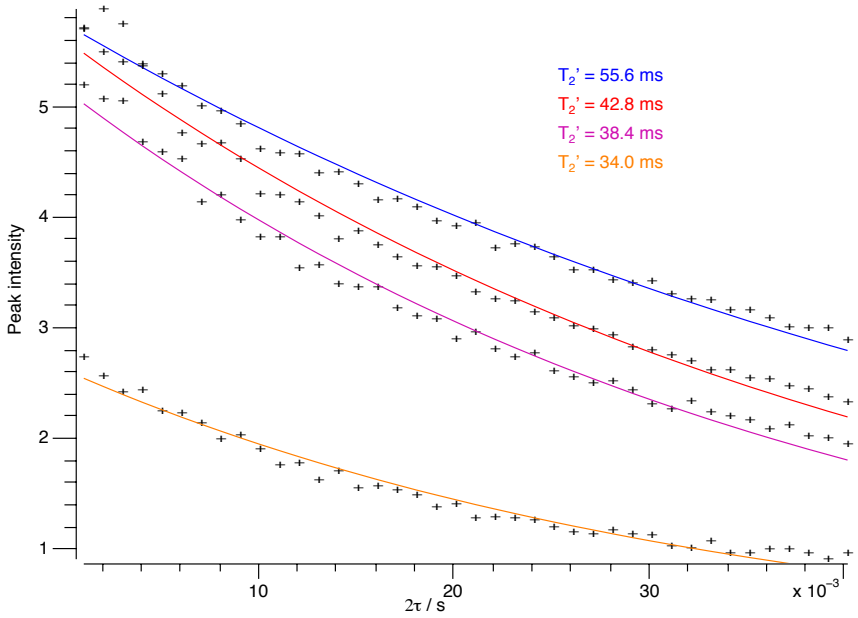

Figure 4.5.1: Intensity decay as a function of τ for a spin echo experiment on L-tyrosine.HCl, used to determine T_2'. The MAS rate was 12 kHz and 100 kHz of CW decoupling was employed. There were 200 experimental repetitions for each value of τ with a relaxation delay of 5 s between each experiment. The four peaks that were used in the analysis were the peaks corresponding to carbon 1 (orange), 7 (purple), 8 (red) and 5 (blue) [c.f. Figure 2.4.4]. The fitting of the exponential decay was performed by *Spinsight* software.

a compromise between J-signal buildup and relaxation decay is essential to obtain maximum cross peak intensity. Due to the inclusion of the π refocusing pulse, the relaxation decay is dominated by the time constant associated with the homogeneous linewidth which cannot be refocused with a π pulse (T_2').

T_2' can be determined experimentally for the sample under investigation. The value of T_2' is dependent upon experimental parameters, such as the heteronuclear dipolar decoupling utilised. The more effective the heteronuclear decoupling, the

larger the value of T_2'. Figure 4.5.1 shows a plot of peak intensity for four of the carbon-13 resonances from L-tyrosine.HCl against the refocusing delay, 2τ, for a spin echo experiment. The heteronuclear dipolar decoupling utilised was CW decoupling. In this instance, different heteronuclear decoupling techniques did not significantly effect the value of T_2'. Since a spin echo experiment uses a refocusing π pulse then the intensity decay for increasing values of 2τ will have the form:

$$S(\tau) = S_0 \exp(-2\tau/T_2') \tag{4.5.1}$$

Fitting of the experimental points to the exponential decay of equation (4.5.1) allows T_2' to be established. The results of the fittings are given in Figure 4.5.1. The value for T_2' that will be used is the mean average of the values for the four fittings, which equals 42.7 ms. This result can then be used in conjunction with the equation for the buildup of cross peak intensity to find the value for τ that returns maximum intensity. Accordingly, a plot was constructed using

$$S(\tau) = \sin^2(2\pi J_{12}\tau) \exp(-4\tau/T_2') \tag{4.5.2}$$

This plot is shown in Figure 4.5.2. The scalar coupling constant between pairs of spins was assumed to be 50 Hz. For a relaxation decay constant of 42.7 ms (dotted blue line) it is found that the maximum possible cross peak intensity is 64 % of the theoretical maximum in the absence of relaxation (dotted red line) and

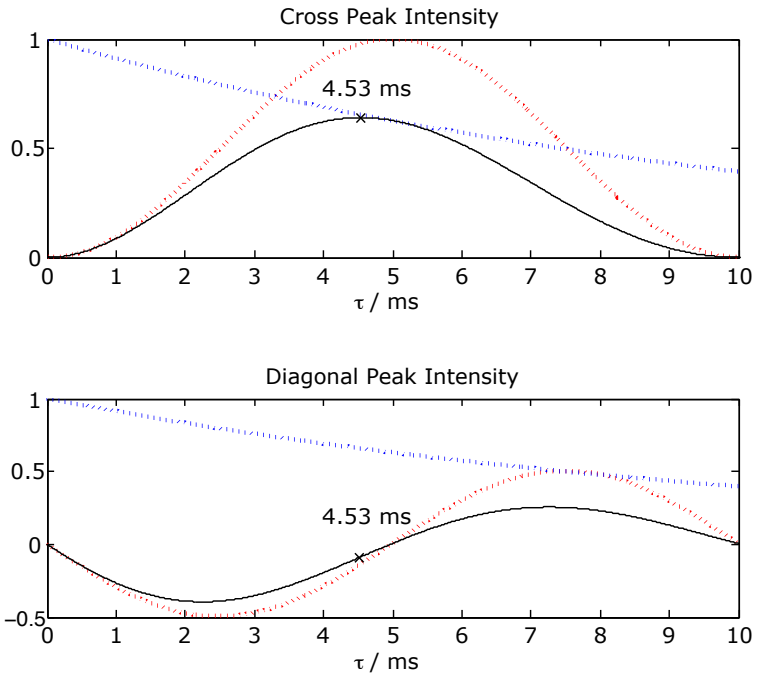

Figure 4.5.2: Illustration of the intensity buildup curves of the cross peaks and diagonal peaks as a function of τ for a SAR-COSY experiment on L-tyrosine.HCl. The dotted red line represents the intensity buildup in the absence of relaxation assuming a J-coupling of 50 Hz. The dotted blue line represents the T_2' decay assuming $T_2' = 42.7$ ms. The solid black line represents the combination of the J-buildup and relaxation processes. Also indicated is the τ time at which maximum cross peak intensity is returned under these conditions.

is observed at $\tau = 4.53$ ms. Also shown in the figure is the corresponding plot for the diagonal peak intensity. This illustrates that the diagonal peak intensity for spin pairs with a 50 Hz scalar coupling resulting from a refocusing delay $2\tau = 9.06$ ms is small (10 % of the theoretical maximum for the intensity of the cross peaks in the absence of relaxation) and negative.

Therefore, when performing a SAR-COSY experiment on this sample of natural

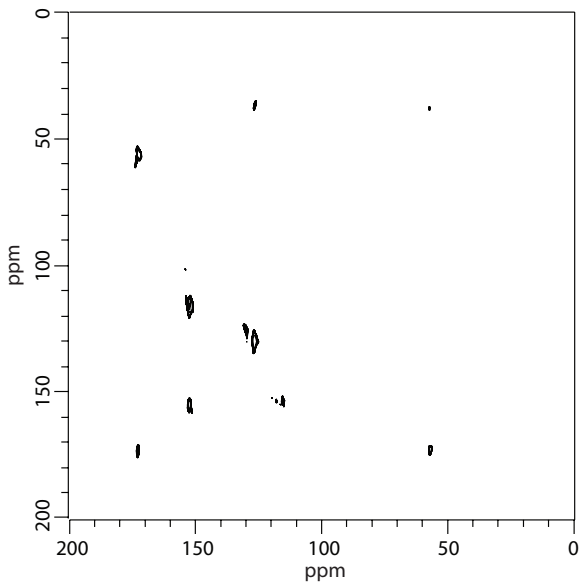

Figure 4.5.3: SAR-COSY spectrum of natural abundance L-tyrosine.HCl. A *Varian* 4 mm double-resonance MAS probe was employed at a carbon-13 Larmor frequency of 75.47 MHz and a MAS rate of 12.0 kHz. 3456 scans were recorded for each of 64 t_1 increments (linear-predicted to 512) with a recycle delay of 1.8 s. A dwell time of 20.0 μs was combined with a direct acquisition time of 20.48 ms in t_2 whilst a dwell time of 10.0 μs was used in t_1 resulting in a total indirect acquisition time of 0.6 ms. The refocusing delay, 2τ, was 9.6 ms and 100 kHz of XiX heteronuclear decoupling was used. The total experiment time was 111 h.

abundance L-tyrosine.HCl, a refocusing delay (2τ) of 9.06 ms should be employed to maximise the signal from the cross peaks. However, 9.6 ms was used because this also returns 64 % of the maximum theoretical intensity of the cross peaks in the absence of relaxation[21] but only 4 % is returned for the diagonal peaks (compared to 10 % with $2\tau = 9.06$). The resulting spectrum from this experiment is given in Figure 4.5.3. Further improvement in the signal-to-noise of the cross peaks was achieved with high-performance heteronuclear decoupling; in this case

[21] $2\tau = 9.06$ ms returns 64.00 % and $2\tau = 9.60$ ms returns 63.53 %

XiX decoupling. In addition, the *Varian* 4 mm double-resonance MAS probe was chosen for the experiment since a combination of high MAS rate, high decoupling power and substantial sample volume could be used; all resulting in enhanced signal-to-noise. Instantly noticeable in Figure 4.5.3, through comparison with the SAR-COSY spectrum of U-^{13}C L-tyrosine.HCl (Figure 4.4.1), is that not all of the cross peaks are present. What is also noticeable is that diagonal peaks at (173,173) and (152,152) are present, and furthermore that the contours of these peaks have a positive intensity. Diagonal peaks appear positive as a result of a scalar coupling to another spin that exceeds the estimated 50 Hz. Although this experiment does not produce all of the expected cross peaks associated with L-tyrosine, it can be concluded that SAR-COSY is applicable to the study of natural abundance carbon-13 homonuclear scalar correlations since cross peaks are observed.

The signal-to-noise ratio for the SAR-COSY spectrum of natural abundance L-tyrosine was too low for a complete set of cross peaks to be observed within the time dedicated to the experiment. In principle greater signal-to-noise can be achieved by performing the experiment at a higher magnetic field strength and also by dedicating more time to the acquisition. Figure 4.5.4 shows a SAR-COSY spectrum of approximately 80 mg of natural abundance progesterone. Although progesterone is an example of a sample that has an unfavourably long relaxation time, with proton T_1 times of the order of 6 s, the carbon-13 linewidths

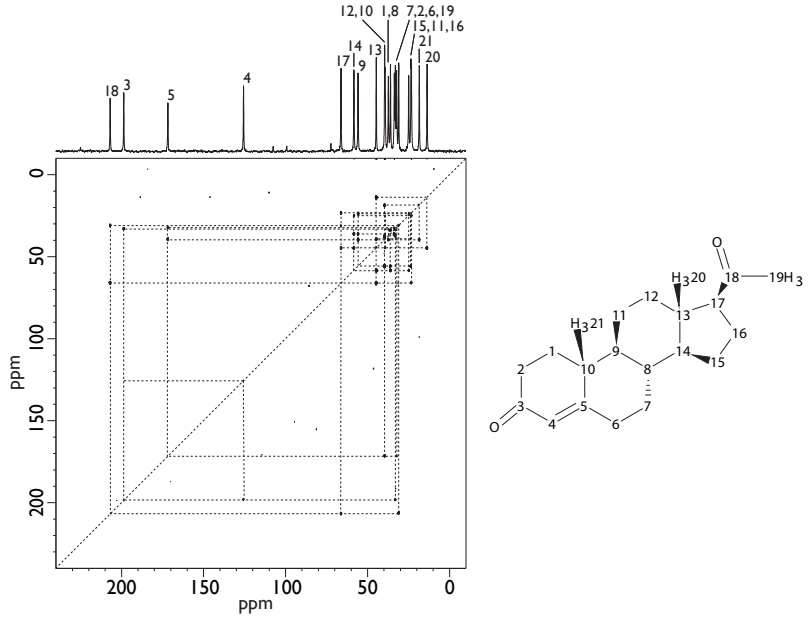

Figure 4.5.4: SAR-COSY spectrum of progesterone. A *Bruker* 4 mm double-resonance MAS probe was employed at a carbon-13 Larmor frequency of 125.74 MHz and a MAS rate of 12.5 kHz. 256 scans were recorded for each of 300 t_1 increments with a recycle delay of 10 s. A dwell time of 13.2 μs was combined with a direct acquisition time of 27.08 ms in t_2 whilst a dwell time of 14.0 μs was used in t_1 resulting in a total indirect acquisition time of 4.2 ms. The refocusing delay, 2τ, was 12.16 ms and 125 kHz of SPINAL 64 [106] heteronuclear decoupling was used. The assignment of the carbon-13 resonances made on the basis of the SAR-COSY cross peaks is given on the one-dimensional MAS spectrum and relates to the structure of progesterone shown (right). The total experiment time was 240 h.

are favourably small and hence the signal-to-noise is relatively large. Recording a SAR-COSY spectrum at a higher magnetic field and for over twice the time as for the natural abundance L-tyrosine results in the complete set of cross peaks for this sample. Furthermore, efficient suppression of the diagonal peaks is demonstrated, especially compared to the very similar UC2QF-COSY spectrum of vitamin D_3 in Ref. [99], resulting in good resolution of the cross peaks in the

crowded region at low δ values. The large number of scalar correlations observed allows the assignment of the carbon-13 spectrum. Although the duration of the experiment is long, further reductions can be expected given larger magnetic fields and improved probe technologies, such as the advent of cryogenic MAS probes.

4.6 Application of SAR-COSY to Caesium Fulleride

The utility of SAR-COSY for recording scalar correlation spectra of disordered solids is illustrated here by an application to the assignment of the carbon-13 spectrum of the polymer phase of caesium fulleride. The alkali metal intercalated fullerides RbC_{60} and CsC_{60} form several phases [107, 108] with interesting electronic and magnetic properties. Above $\sim$ 350 K these samples adopt a fcc[22] structure. However, below this temperature these samples undergo a reversible phase change. Figure 4.6.1 illustrates the ambient temperature orthorhombic phase of CsC_{60} where the separation between the fullerene molecules along the c-axis is approximately 9 % smaller than along a and b [109]. This unusually short distance is indicative of the formation of linkages between fullerene molecules by a [2+2] cyclo-addition, resulting in polymeric chains along the c-axis [110], as depicted in Figure 4.6.1(a). Figure 4.6.1(b) depicts the structure of this ambient temperature orthorhombic phase as viewed along each of the crystallographic

[22]fcc = face centered cubic; the same structure as is formed by NaCl

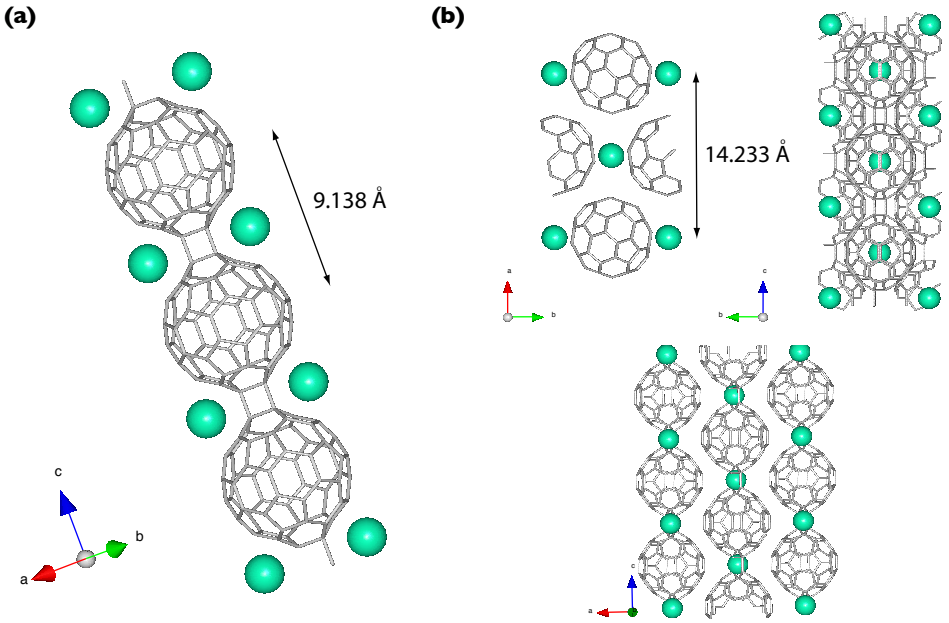

Figure 4.6.1: The ambient temperature orthorhombic phase of CsC_{60}, showing the polymeric chains along the *c*-axis (a) and the three-dimensional crystal structure viewed along each of the crystallographic axes (b).

axes.

Carbon-13 MAS allows resonances from the 16 inequivalent sites on the fullerene molecule to be resolved [111] with resonance frequencies determined by the sum of Knight shift (c.f. 1.2.8) and chemical shift contributions. Figure 4.6.2 shows this carbon-13 MAS spectrum. Note that the peaks observed at $\delta = 143$ and $\delta = 179$ ppm are produced by unpolymerized C_{60} and fcc CsC_{60}, respectively. All other carbon-13 nuclei (those from the polymerized orthorhombic phase), except for the linkage carbons (site 1 on the fullerene monomer unit shown in the figure), could be expected to have a similar chemical shift to the C_{60} carbon-13 nuclei

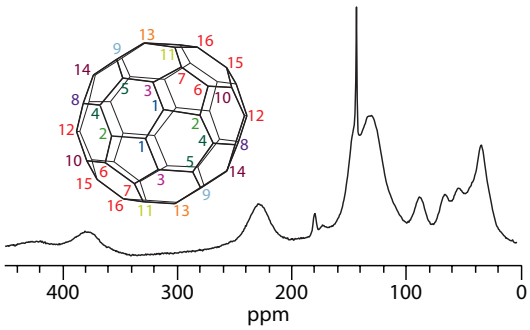

Figure 4.6.2: Carbon-13 MAS NMR of CsC_{60}. A *Varian* 3.2 mm double-resonance MAS probe was employed at a carbon-13 Larmor frequency of 75.47 MHz and a MAS rate of 17.4 kHz. 64 scans were recorded with a recycle delay of 5 s. A dwell time of 16.67 μs was combined with a direct acquisition time of 17.07 ms in t_2. No heteronuclear decoupling was necessary. Note the Knight-shifted resonances which extend well beyond the normal carbon-13 chemical shift range. A fullerene monomer unit from polymer CsC_{60} is also shown, viewed along a direction which is approximately parallel to the crystallographic *c*-axis. The 16 inequivalent carbon sites are labelled.

($\delta = 143$ ppm). Any deviation from this δ value will be a result of a Knight shift and thus, a result of a hyperfine coupling to unpaired electrons.

Magnetic spin susceptibility [109] and frequency-dependent conductivity measurements [113] suggested that the polymeric phase is a quasi one-dimensional metallic conductor. However, band structure calculations [114] predicted a surprising three-dimensional semi-metallic band structure in which electron transport is dominated by inter-chain hopping and the fullerene molecules are connected by insulating contacts. In order to test the conflicting structural models the carbon-13 resonances were assigned to the sites on the fullerene so that the variation of the hyperfine coupling with site could be established. This assign-

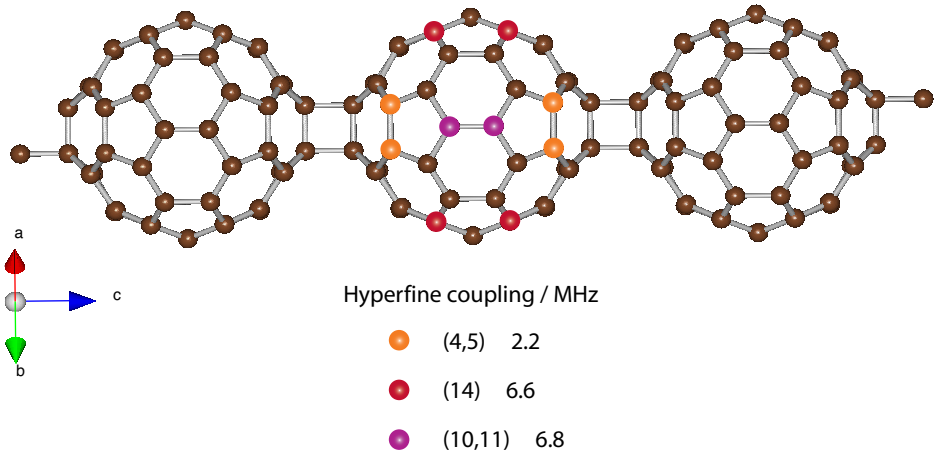

Figure 4.6.3: Hyperfine couplings in CsC_{60} obtained from DFT calculations based on a three-dimensional band structure [112].

ment was performed using carbon-13 r-INADEQUATE spectra of 50 % enriched U-^{13}C CsC_{60} [115], combined with two further pieces of experimental evidence. These are the identification of the peak at $\delta = 35$ ppm with the sp^3 linkage site [111] and the ability of REDOR experiments to distinguish between similar sites according to their proximity to the caesium ion [112]. Experimental Knight shifts obtained in this fashion were compared with the results of Density Functional Theory (DFT) calculations [112] of the hyperfine couplings based on the three-dimensional semi-metal band structure. The results of these calculations are shown in Figure 4.6.3. The calculations suggest that the electron density resides equatorially on the fullerene and avoids the linkage sites. The excellent correspondence between calculations and the experimental assignment of the sites with large hyperfine coupling proved that the semi-metal picture is

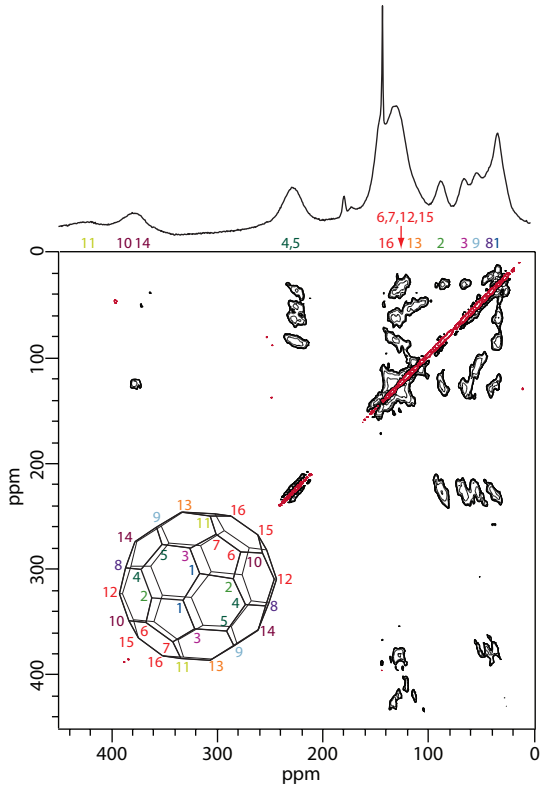

Figure 4.6.4: SAR-COSY spectrum of 50%-U-^{13}C CsC_{60}. The acquisition parameters are given in the text. Black contours have positive intensity and red contours have negative intensity. A fullerene monomer unit from polymer CsC_{60} is also shown, viewed along a direction which is approximately parallel to the crystallographic *c*-axis. The 16 inequivalent carbon sites are labelled and the assignment of the carbon-13 resonances to these sites on the basis of the SAR-COSY cross peaks is given on the one-dimensional MAS spectrum (above).

more appropriate than the one-dimensional metallic structure proposed earlier.

Figure 4.6.4 shows a SAR-COSY spectrum of the polymer phase of caesium fulleride. The pulse sequence of Figure 4.1.1 was used without the cross polarization step due to the absence of protons in the sample. A *Varian* 3.2 mm double-resonance MAS probe was employed at a carbon-13 Larmor frequency of 75.47

MHz and a MAS rate of 17.4 kHz. 160 scans were recorded for each of 256 t_1 increments with a recycle delay of 5 s. A dwell time of 20.0 μs was combined with a direct acquisition time of 20.48 ms in t_2 whilst a dwell time of 10.0 μs was used in t_1 resulting in a total indirect acquisition time of 2.6 ms. The refocusing delay, 2τ, was 5.0 ms and no heteronuclear decoupling was necessary. In the processing of the two-dimensional data, 100 Hz of Gaussian line-broadening was applied in the direct dimension and a Hann function was applied in the indirect dimension. Also shown in the figure is a single fullerene monomer unit from polymer CsC_{60} viewed along a direction which is approximately parallel to the crystallographic *c*-axis. The 16 inequivalent sites are labelled, with site (1) corresponding to the sp^3 linkage between adjacent fullerene units in the polymer chain. The apparent linewidths $1/\pi T_2^*$ observed in the carbon-13 MAS spectrum are greater than 500 Hz, with the broadening arising from shift distributions caused by chain end effects, defects in packing or incomplete polymerization. The carbon-13 MAS spectrum can be assigned using the cross peaks observed in the SAR-COSY spectrum and the result is in overall agreement with that obtained previously [115]. In particular, resonances which appear at $\delta > 200$ ppm, and hence have substantial positive Knight shifts, correspond to sites (4), (5), (10), (11) and (14). This is consistent with the large hyperfine couplings obtained for these sites from the DFT calculations as shown in Figure 4.6.3. However, the good resolution obtained for crowded regions of the SAR-COSY spectrum allows the assignment

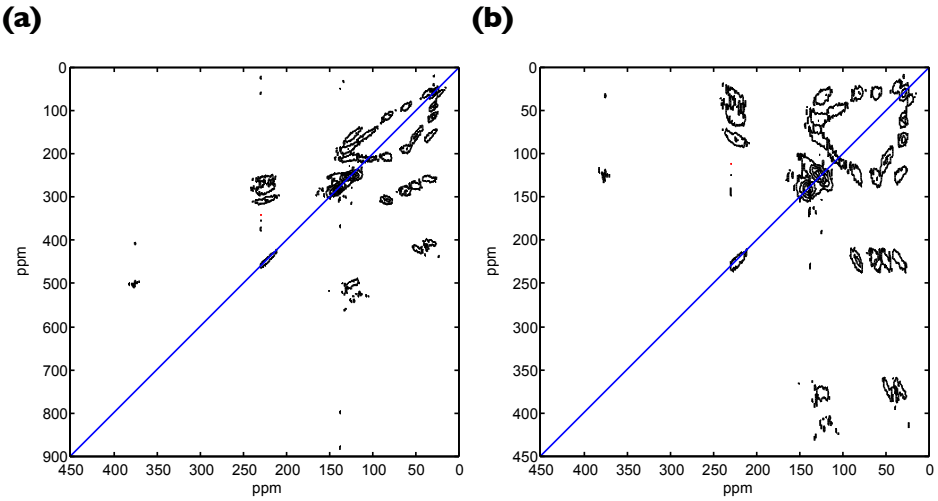

Figure 4.6.5: r-INADEQUATE spectrum of 50%-U-^{13}C CsC_{60} taken from Ref. [115] (a) and the effect of shearing this spectrum (b). Diagonals (blue) have been added for illustrative purposes.

made with r-INADEQUATE to be refined. In particular, site (16) can be resolved on the high δ side of the broad resonance due to sites (6), (7), (12) and (15) by virtue of its cross peaks to sites (11) and (15). It should be noted that the shapes of the SAR-COSY cross peaks indicate that the variations in the chemical shift arising from the disorder in polymer CsC_{60} are correlated between neighbouring sites. A straightforward SQ-SQ shift correlation format has been shown recently to be suitable for exploring two-dimensional shift and J coupling distributions in disordered solids [116, 117]. However, to date these distributions have been generated by *shearing* the DQ-SQ correlation spectra produced by r-INADEQUATE experiments.

The carbon-13 r-INADEQUATE spectrum of 50%-U-^{13}C CsC_{60} from Ref. [115]

is reproduced in Figure 4.6.5(a). Figure 4.6.5(b) shows the result of performing a shearing transformation on this spectrum. The shearing of the DQ-SQ spectrum in (a) was performed by creating a new ω_1 value for each point of the contour plot by subtracting the corresponding ω_2 value from the original ω_1 value. Constructing a new contour plot using the revised ω_1 values gives the spectrum shown in (b). This is the type of transformation used in Ref. [116] to produce a SQ-SQ type spectrum from a DQ-SQ r-INADEQUATE spectrum in order to perform a further analysis. Note the likeness of Figure 4.6.5(b) to the SAR-COSY spectrum given in Figure 4.6.4.

The further analysis performed in Ref. [116] is a chemical shift conditional probability distribution analysis. A cross peak is selected from a SQ-SQ spectrum. This cross peak can be represented as a matrix of intensities. Each column of this matrix is normalized so that the sum of the absolute values of the intensities in the column is 1. This then yields an experimental conditional probability matrix detailing the probability that a site resonates at Ω_1 given that another site resonates at Ω_2. If the same normalization process is applied to the rows of the original cross peak matrix then an experimental conditional probability matrix will be formed detailing the probability that a site resonates at Ω_2 given that another site resonates at Ω_1. If the signal-to-noise ratio of the cross peak is low a filter can be applied that sets the conditional probability to zero for intensities that are below a certain threshold. This prevents a conditional probability being

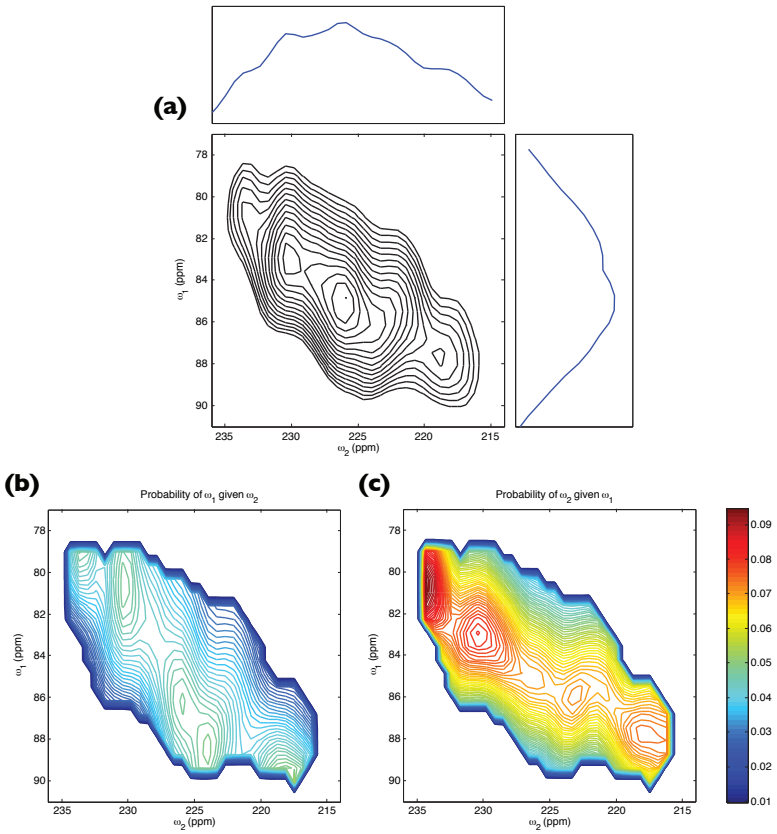

Figure 4.6.6: (a) SAR-COSY cross peak between sites 2 and 4 of CsC_{60} extracted from Figure 4.6.4 along with skyline projections of this peak (top and right). The resulting conditional probability distributions are shown in (b) and (c).

assigned to noise. Note, however, that applying this filter means that the sum of the intensities in a given column (or row) will now not be 1. The resulting conditional probability distributions can be used to probe the structural disorder of solids.

Conditional probability distributions are given in Figures 4.6.6 and 4.6.7 for two of the cross peaks from the SAR-COSY spectrum of CsC_{60} (Figure 4.6.4). Note that, unlike the r-INADEQUATE spectra of Ref. [116], a shearing transformation

does not have to be applied to the SAR-COSY data since a SQ-SQ type spectrum is obtained in the first instance. Figure 4.6.6(a) shows one of the SAR-COSY cross peaks resulting from the coupling between sites 2 and 4 of CsC_{60}. The skyline projections of this cross peak (top and right) illustrate that there is a distribution of chemical shifts for both sites. The conditional probability distributions for this cross peak, shown in (b) and (c), demonstrate the likelihood that one chemical shift from the distribution from site 2 will be correlated with a given chemical shift from the distribution from site 4 and vice versa, respectively. For instance, from Figure 4.6.6(b) it can be seen that if site 4 has $\delta = 225$ ppm then the most probable chemical shift for site 2 will be approximately $\delta = 89$ ppm.

Figure 4.6.7(a) shows one of the SAR-COSY cross peaks resulting from the coupling between sites 8 and 12 of CsC_{60} and the corresponding conditional probability distributions are given in (b) and (c). Similar to the previous cross peak, a distribution of chemical shifts is observed for both sites and the distributions appear to be correlated. However, this cross peak has a $y = kx$ chemical shift correlation structure (whereas the previous cross peak has a $y = -kx$ chemical shift correlation structure).

It was postulated earlier that the chemical shift distributions observed for this sample could arise from chain end effects, defects in packing or incomplete polymerization. Although the conditional probability distributions do not discrimi-

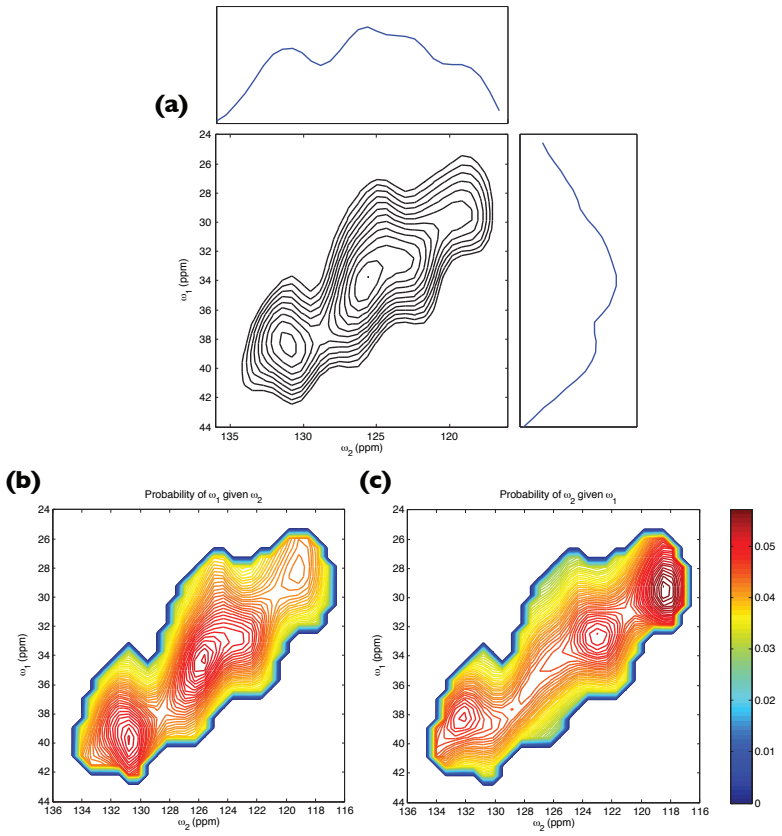

Figure 4.6.7: (a) SAR-COSY cross peak between sites 8 and 12 of CsC_{60} extracted from Figure 4.6.4 along with skyline projections of this peak (top and right). The resulting conditional probability distributions are shown in (b) and (c).

nate between these, it could be suggested that the polymeric phase of CsC_{60} is actually more oligomeric than polymeric. Variable length oligomers could result in the chemical shift distributions observed and the conditional probability plots, which show 3 or 4 maxima, could then elude to the presence of 3 or 4 different chain lengths.

4.7 Conclusions

The SAR-COSY experiment results in a two-fold gain in cross peak intensity relative to its antecedent UC2QF-COSY. Furthermore, for SAR-COSY the diagonal peaks are efficiently suppressed and of opposite sign, resulting in good resolution in crowded areas where cross peaks appear close to the diagonal. The sensitivity of SAR-COSY is equivalent to that of r-INADEQUATE, but the straightforward SQ-SQ shift correlation format is retained. These features make SAR-COSY particularly suitable for measuring homonuclear scalar correlation spectra for nuclei with low natural abundance, such as carbon-13, and of disordered solids. Chemical shift conditional probability distributions can be extracted straight from SAR-COSY cross peaks and can contribute additional information characteristic of disordered solids.

5 Outlook

In this thesis it has been shown that the resolution of proton resonances in solid-state NMR can be dramatically improved by the use of homonuclear decoupling sequences; in particular, the DUMBO-1 sequence. However, the achievable resolution is still a long way from that attainable with solution-state NMR. Improvements in solid-state rotor materials will allow higher MAS rates and thus improve resolution. MAS rates are restricted by the forces that the rotors can withstand. Additionally, faster MAS rates require smaller sample volumes and thus, to counter the sensitivity limitations of NMR, greater static magnetic field strengths are a necessity.

In conjunction with new developments in the mechanical aspects of NMR, advancements in NMR hardware, such as transmitter boards and probes, will allow for a more accurate representation of the pulse schemes of RF irradiation. Improvements in probe design need to mirror the advancements in transmitter board technology owing to the limitations due to *Q factors* of current probes; any upgrade would be nullified if the probe cannot emulate it. Further to this, advancements in computational hardware and software permit more complicated simulations to be completed within realistic time periods. Thus, new decoupling pulse schemes can, in theory, be designed that function according to the latest hardware specifications (phase-switching time etc.) in combination with state-of-

the-art ultra-fast MAS rates.

This cutting-edge research comes at a cost. For the acquisition of high-resolution proton NMR, the DUMBO-1 sequence has been shown to perform well on standard solid-state instrumentation. In fact, the DUMBO-1 sequence can be implemented on standard solid-state instrumentation to obtain a level of resolution that is comparable to the level that the latest hardware developments (850 MHz ^{1}H Larmor frequency and 55 kHz ultra-fast MAS rate) can achieve. Nevertheless, continual progress will contribute new pulse sequences and mechanical hardware that will surpass the efficacy of the DUMBO-1 sequence.

In this thesis the symmetry based sequence that was attempted to recouple the DQ homonuclear dipolar Hamiltonian proved successful. A slight modification of the DQ CRAMPS experiment involving the addition of $\pi/2$ pulses before and after the t_1 period and the shift of the DQ excitation block to immediately precede the reconversion block (c.f. Figure 2.5.2) could produce SQ-SQ dipolar correlation spectra. The DQ excitation and reconversion blocks will not only act as a method for magnetization transfer but also as a DQF. Nonetheless, the resulting spectrum will be equivalent in format to a spin diffusion CRAMPS spectrum and impaired with an uninformative diagonal. The DQ CRAMPS experiment would therefore be the experiment of choice.

An assumption made in Chapter 3 was that there was no self-condensation be-

tween glycerol-functionalized surface-modifying groups in the *Bindzil CC40* silica sol. The relatively small amount of surface-functionalizing groups compared to the rest of the sample, combined with the low natural abundance of the nuclei of interest (and the expense involved in isotopically labelling these systems), means that solid-state NMR is not realistically applicable to elucidate the extent of self-condensation of these surface-modifying groups. Recently, there has been tremendous progress towards the improvement of this sensitivity limitation. A microwave source (a gyrotron) can be used to irradiate unpaired electron spins (contained in optimized polarizing agents) in order to hyperpolarize surrounding nuclear spins (^{1}H, ^{13}C, ^{15}N, ^{29}Si etc.) through a mechanism called *Dynamic Nuclear Polarization* (DNP). When combined with NMR this hyperpolarization of the nuclear spins results in substantial sensitivity enhancements of up to several orders of magnitude. Although DNP was primarily only considered for use at low magnetic fields, recent technological advances have made the use of DNP-enhanced NMR at high magnetic field possible. Consequently, the sensitivity gains associated with DNP-enhanced solid-state NMR should allow the use of two-dimensional scalar correlation experiments (such as SAR-COSY) to determine the extent of self-condensation of functionalizing groups on the surface of this silica sol.

DNP-enhanced solid-state NMR should also allow other previously unfeasible experiments to be performed. Overcoming the sensitivity limitations of scalar cor-

relation experiments, such as the MAS-J-HMQC experiment and SAR-COSY, would encourage the utilisation of these techniques to study low isotopic abundance nuclei in large, complicated systems. Furthermore, semi-conducting nanostructures such as caesium fulleride have become a very active research area since the crystalline growth of semi-conducting nanowires is now controllable. These unique objects exhibit original properties related to their dimensionality and surface and should offer very promising insights for photonics and nano-electronics. Notably it is believed that the nanowires' environment can influence their properties. One of the approaches to validate this idea consists of directly modifying the nanowires' surface by molecular grafting, which should induce an alteration, leading to a control, of the electrical conductivity and of the carrier mobility in the nanowires. Nevertheless, despite the growing interest in modifying nanometer surfaces, a very limited number of modified nanostructures have been characterised chemically or physically. Application of the two-dimensional hetero- and homonuclear correlation experiments described in this thesis, in combination with this sensitivity-enhanced solid-state NMR technique, could yield the aspired characterisation of such functionalized molecular wires along with other nanoscale materials.

References

[1] A. Abragam, *The Principles of Nuclear Magnetism*, Oxford University Press; pp. 97–132; First ed., 1961.

[2] N. Bloembergen and T. J. Rowland, *Phys. Rev.*, 1955, **97**(6), 1679–1698.

[3] O. W. Sorensen, G. W. Eich, M. H. Levitt, G. Bodenhausen, and R. R. Ernst, *Prog. Nucl. Magn. Reson. Spectrosc.*, 1983, **16**(Part 2), 163–192.

[4] M. H. Levitt, *Spin Dynamics*, John Wiley & Sons Ltd; pp. 573–574; First ed., 2001.

[5] J. Keeler, *Understanding NMR Spectroscopy*, John Wiley & Sons Ltd; pp. 370–375; First ed., 2005.

[6] G. Bodenhausen, K. H, and R. R. Ernst, *J. Magn. Reson.*, 1984, **58**(3), 370–388.

[7] S. P. Brown, *MPAGS Postgraduate NMR Course: Two-Dimensional NMR*, 2007.

[8] W. P. Aue, E. Bartholdi, and R. R. Ernst, *J. Chem. Phys.*, 1976, **64**(5), 2229–2246.

[9] S. Hiller, C. Wasmer, G. Wider, and K. Wüthrich, *J. Am. Chem. Soc.*, 2007, **129**(35), 10823–10828.

[10] D. J. States, R. A. Haberkorn, and D. J. Ruben, *J. Magn. Reson.*, 1982, **48**, 286–292.

[11] D. Marion and K. Wüthrich, *Biochem. Biophys. Res. Commun.*, 1983, **113**(3), 967–974.

[12] D. Marion, M. Ikura, R. Tschudin, and A. Bax, *J. Magn. Reson*, 1989, **85**(2), 393–399.

[13] A. Pines, M. G. Gibby, and J. S. Waugh, *J. Chem. Phys.*, 1973, **59**(2), 569–590.

[14] S. R. Hartmann and E. L. Hahn, *Phys. Rev.*, 1962, **128**(5), 2042–2053.

[15] O. B. Peersen, X. L. Wu, I. Kustanovich, and S. O. Smith, *J. Magn. Reson., Series A*, 1993, **104**(3), 334 – 339.

[16] E. R. Andrew, A. Bradbury, and R. Eades, *Nature*, 1958, **182**, 1659–1659.

[17] M. M. Maricq and J. S. Waugh, *J. Chem. Phys.*, 1979, **70**(7), 3300–3316.

[18] W. Magnus, *Commun. Pure Appl. Math.*, 1954, **7**(4), 649–673.

[19] A. Samoson, T. Tuherm, J. Past, A. Reinhold, T. Anupold, and N. Heinmaa, *New techniques in solid-state NMR*, 2005, **246**, 15–31.

[20] A. L. Bloom and J. N. Shoolery, *Phys. Rev.*, 1955, **97**(5), 1261–1265.

[21] A. E. Bennett, C. M. Rienstra, M. Auger, K. V. Lakshmi, and R. G. Griffin, *J. Chem. Phys.*, 1995, **103**(16), 6951–6958.

[22] A. Detken, E. H. Hardy, M. Ernst, and B. H. Meier, *Chem. Phys. Lett.*, 2002, **356**(3-4), 298–304.

[23] M. Ernst, *J. Magn. Reson.*, 2003, **162**(1), 1–34.

[24] M. Lee and W. I. Goldburg, *Phys. Rev.*, 1965, **140**(4A), 1261–1271.

[25] J. S. Waugh, L. M. Huber, and U. Haeberle, *Phys. Rev. Lett.*, 1968, **20**(5), 180–182.

[26] M. J. Duer, *Introduction to Solid-State NMR Spectroscopy*, Blackwell Publishing; pp. 86–96; First ed., 2004.

[27] P. Mansfield, M. J. Orchard, D. C. Stalker, and K. H. B. Richards, *Phys. Rev. B*, 1973, **7**(1), 90–105.

[28] W. Rhim, D. Elleman, and R. Vaughan, *J. Chem. Phys.*, 1973, **58**(4), 1772–1773.

[29] W. Rhim, D. Elleman, and R. Vaughan, *J. Chem. Phys.*, 1973, **59**(7), 3740–3749.

[30] D. Burum and W. Rhim, *J. Chem. Phys.*, 1979, **71**(2), 944–956.

[31] D. Burum, M. Linder, and R. Ernst, *J. Magn. Reson.*, 1981, **44**(1), 173–188.

[32] K. Takegoshi and C. McDowell, *Chem. Phys. Lett.*, 1985, **116**(2-3), 100–104.

[33] M. Hohwy, P. Bower, H. Jakobsen, and N. Nielsen, *Chem. Phys. Lett.*, 1997, **273**(5-6), 297–303.

[34] M. Carravetta, M. Eden, X. Zhao, A. Brinkmann, and M. Levitt, *Chem. Phys. Lett.*, 2000, **321**(3-4), 205–215.

[35] A. Bielecki, A. Kolbert, and M. Levitt, *Chem. Phys. Lett.*, 1989, **155**(4-5), 341–346.

[36] A. Bielecki, A. Kolbert, H. de Groot, R. Griffin, and M. Levitt, *Adv. Magn. Reson.*, 1990, **14**, 111–124.

[37] E. Vinogradov, P. Madhu, and S. Vega, *Chem. Phys. Lett.*, 1999, **314**(5-6), 443–450.

[38] E. Vinogradov, P. Madhu, and S. Vega, *Chem. Phys. Lett.*, 2000, **329**(3-4), 207–214.

[39] E. Vinogradov, P. Madhu, and S. Vega, *J. Chem. Phys.*, 2001, **115**(19), 8983–9000.

[40] E. Vinogradov, P. Madhu, and S. Vega, *Chem. Phys. Lett.*, 2002, **354**(3-4), 193–202.

[41] B. Gerstein, R. Pembleton, R. Wilson, and L. Ryan, *J. Chem. Phys.*, 1977, **66**(1), 361–362.

[42] A. Lesage, D. Sakellariou, S. Hediger, B. Elena, P. Charmont, S. Steuernagel, and L. Emsley, *J. Magn. Reson.*, 2003, **163**(1), 105–113.

[43] E. Salager, R. S. Stein, S. Steuernagel, A. Lesage, B. Elena, and L. Emsley, *Chem. Phys. Lett.*, 2009, **469**(4-6), 336–341.

[44] C. Filip and S. Hafner, *J. Magn. Reson.*, 2000, **147**(2), 250–260.

[45] B. Elena, G. de Paepe, and L. Emsley, *Chem. Phys. Lett.*, 2004, **398**(4-6), 532–538.

[46] V. E. Zorin, M. Ernst, S. P. Brown, and P. Hodgkinson, *J. Magn. Reson.*, 2008, **192**(2), 183–196.

[47] D. Sakellariou, A. Lesage, P. Hodgkinson, and L. Emsley, *Chem. Phys. Lett.*, 2000, **319**(3-4), 253–260.

[48] A. McDermott and C. F. Ridenour in *Encyclopedia of NMR*, ed. D. M. Grant and R. K. Harris; Wiley, London, 1997; pp. 3820–3821.

[49] A. Lesage, D. Sakellariou, S. Steuernagel, and L. Emsley, *J. Am. Chem. Soc.*, 1998, **120**(50), 13194–13201.

[50] M. Leskes and S. Vega, *J. Chem. Phys.*, 2009, **130**(12), 124506.

[51] M. Lera and C. J. Hayes, *Org. Lett.*, 2001, **3**(17), 2765–2768.

[52] W. E. Crowe and D. R. Goldberg, *J. Am. Chem. Soc.*, 1995, **117**(18), 5162–5163.

[53] W. E. Crowe and Z. J. Zhang, *J. Am. Chem. Soc.*, 1993, **115**(23), 10998–10999.

[54] S. Zhang, B. H. Meier, and R. R. Ernst, *Phys. Rev. Lett.*, 1992, **69**(14), 2149–2151.

[55] N. Bloembergen, *Physica*, 1949, **15**(3-4), 386–426.

[56] S. P. Brown, A. Lesage, B. Elena, and L. Emsley, *J. Am. Chem. Soc.*, 2004, **126**(41), 13230–13231.

[57] M. Hohwy, H. J. Jakobsen, M. Eden, M. H. Levitt, and N. C. Nielsen, *J. Chem. Phys.*, 1998, **108**(7), 2686–2694.

[58] Y. K. Lee, N. D. Kurur, M. Helmle, O. G. Johannessen, N. C. Nielsen, and M. H. Levitt, *Chem. Phys. Lett.*, 1995, **242**(3), 304–309.

[59] S. P. Brown, *Prog. Nucl. Magn. Reson. Spectrosc.*, 2007, **50**(4), 199–251.

[60] S. Macura and R. R. Ernst, *Mol. Phys.*, 1980, **41**(1), 95–117.

[61] E. W. Abel, T. P. J. Coston, K. G. Orrell, V. Sik, and D. Stephenson, *J. Magn. Reson.*, 1986, **70**(1), 34–53.

[62] A. Kubo and C. A. McDowell, *J. Chem. Soc. Farad. T. I*, 1988, **84**(11), 3713–3730.

[63] C. L. Perrin and T. J. Dwyer, *Chem. Rev.*, 1990, **90**(6), 935–967.

[64] P. Caravatti, L. Braunschweiler, and R. R. Ernst, *Chem. Phys. Lett.*, 1983, **100**(4), 305–310.

[65] G. R. Marshall, D. D. Beusen, K. Kociolek, A. S. Redlinski, M. T. Leplawy, Y. Pan, and J. Schaefer, *J. Am. Chem. Soc.*, 1990, **112**(3), 963–966.

[66] X. Zhao, M. Eden, and M. H. Levitt, *Chem. Phys. Lett.*, 2001, **342**(3-4), 353–361.

[67] A. Brinkmann and M. H. Levitt, *J. Chem. Phys.*, 2001, **115**(1), 357–384.

[68] A. Lesage and L. Emsley, *J. Magn. Reson.*, 2001, **148**(2), 449–454.

[69] L. Duma, S. Hediger, A. Lesage, D. Sakellariou, and L. Emsley, *J. Magn. Reson.*, 2003, **162**(1), 90–101.

[70] C. W. Chen, T. Serizawa, and M. Akashi, *Chem. Mat.*, 1999, **11**(5), 1381–1389.

[71] D. B. Mitzi, *Chem. Mat.*, 2001, **13**(10), 3283–3298.

[72] E. Manias, A. Touny, L. Wu, K. Strawhecker, B. Lu, and T. C. Chung, *Chem. Mat.*, 2001, **13**(10), 3516–3523.

[73] G. K. Agarwal, J. J. Titman, M. J. Percy, and S. P. Armes, *J. Phys. Chem. B*, 2003, **107**(45), 12497–12502.

[74] J. Leuninger, F. Tiarks, H. Wiese, and B. Schuler, *Farbe Lack*, 2004, **13**, 30.

[75] Z. Xue and H. Wiese, *Int. Patent WO 03000760*, 2003.

[76] P. Greenwood and H. Lagnemo, *Int. Patent WO2004/035474A1*, 2004.

[77] A. Schmid, J. Tonnar, and S. P. Armes, *Adv. Mater.*, 2008, **20**(17), 3331–3336.

[78] A. Schmid, S. P. Armes, C. A. P. Leite, and F. Galembeck, *Langmuir*, 2009, **25**(4), 2486–2494.

[79] A. Schmid, P. Scherl, S. P. Armes, C. A. P. Leite, and F. Galembeck, *Macromolecules*, 2009, **42**(11), 3721–3728.

[80] T. Bein, R. F. Carver, R. D. Farlee, and G. D. Stucky, *J. Am. Chem. Soc.*, 1988, **110**(14), 4546–4553.

[81] M. W. Daniels and L. F. Francis, *J. Colloid Interface Sci.*, 1998, **205**(1), 191–200.

[82] I. Klur, J. F. Jacquinot, F. Brunet, T. Charpentier, J. Virlet, C. Schneider, and P. Tekely, *J. Phys. Chem. B*, 2000, **104**, 10162–10167.

[83] B. J. van Rossum, C. P. de Groot, V. Ladizhansky, S. Vega, and H. J. M. de Groot, *J. Am. Chem. Soc.*, 2000, **122**(14), 3465–3472.

[84] D. Dupin, A. Schmid, J. A. Balmer, and A. S. P, *Langmuir*, 2007, **23**(23), 11812–11818.

[85] J. A. Balmer, S. P. Armes, P. W. Fowler, T. Tarnai, Z. Gaspar, K. A. Murray, and N. S. J. Williams, *Langmuir*, 2009, **25**(9), 5339–5347.

[86] T. Cosgrove, S. J. Mears, L. Thompson, and I. Howell In ed. Sharma, R, *Surfactant Adsorption and Surface Solubilization*, Vol. 615 of *ACS Symposium Series*, pp. 196–204, 1155 Sixteenth St NW, Washington, DC 20036, 1995. Amer Chem Soc.

[87] T. Cosgrove, P. C. Griffiths, and P. M. Lloyd, *Langmuir*, 1995, **11**(5), 1457–1463.

[88] T. Cosgrove, S. J. Mears, T. Obey, L. Thompson, and R. D. Wesley, *Colloid Surf. A-Physicochem. Eng. Asp.*, 1999, **149**(1-3), 329–338.

[89] C. Flood, T. Cosgrove, I. Howell, and P. Revell, *Langmuir*, 2006, **22**(16), 6923–6930.

[90] U. Piantini, O. W. Sorensen, and R. R. Ernst, *J. Am. Chem. Soc.*, 1982, **104**(24), 6800–6801.

[91] L. Braunschweiler and R. R. Ernst, *J. Magn. Reson.*, 1983, **53**(3), 521–528.

[92] A. S. D. Heindrichs, H. Geen, C. Giordani, and J. J. Titman, *Chem. Phys. Lett.*, 2001, **335**(1-2), 89–96.

[93] A. Lesage, M. Bardet, and L. Emsley, *J. Am. Chem. Soc.*, 1999, **121**(47), 10987–10993.

[94] L. J. Mueller, D. W. Elliott, G. M. Leskowitz, J. Struppe, R. A. Olsen, K. C. Kim, and C. A. Reed, *J. Magn. Reson.*, 2004, **168**(2), 327–335.

[95] A. Bax, R. Freeman, and T. A. Frenkiel, *J. Am. Chem. Soc.*, 1981, **103**(8), 2102–2104.

[96] G. P. Holland, J. E. Jenkins, M. S. Creager, R. V. Lewis, and J. L. Yarger, *Chem. Commun.*, 2008, (43), 5568–5570.

[97] F. Fayon, G. Le Saout, L. Emsley, and D. Massiot, *Chem. Commun.*, 2002, (16), 1702–1703.

[98] S. P. Brown, M. Perez-Torralba, D. Sanz, R. M. Claramunt, and L. Emsley, *J. Am. Chem. Soc.*, 2002, **124**(7), 1152–1153.

[99] R. Olsen, J. Struppe, D. Elliott, R. Thomas, and L. Mueller, *J. Am. Chem. Soc.*, 2003, **125**(39), 11784–11785.

[100] L. Chen, R. A. Olsen, D. W. Elliott, J. M. Boettcher, D. H. Zhou, C. M. Rienstra, and L. J. Mueller, *J. Am. Chem. Soc.*, 2006, **128**(31), 9992–9993.

[101] L. Chen, J. M. Kaiser, J. Lai, T. Polenova, J. Yang, C. M. Rienstra, and L. J. Mueller, *Magn. Reson. Chem.*, 2007, **45**(Suppl. S), S84–S92.

[102] S. Talluri and H. A. Scheraga, *J. Magn. Reson.*, 1990, **86**(1), 1–10.

[103] M. Veshtort and R. G. Griffin, *J. Magn. Reson.*, 2006, **178**(2), 248–282.

[104] S. Cadars, J. Sein, L. Duma, A. Lesage, T. N. Pham, J. H. Baltisberger, S. P. Brown, and L. Emsley, *J. Magn. Reson.*, 2007, **188**(1), 24–34.

[105] P. H. Bolton, *J. Magn. Reson.*, 1982, **48**(2), 336–340.

[106] B. M. Fung, A. K. Khitrin, and K. Ermolaev, *J. Magn. Reson.*, 2000, **142**(1), 97–101.

[107] J. Winter and H. Kuzmany, *Solid State Commun.*, 1992, **84**(10), 935–938.

[108] A. Jánossy, O. Chauvet, S. Pekker, J. R. Cooper, and L. Forró, *Phys. Rev. Lett.*, 1993, **71**(7), 1091–1094.

[109] O. Chauvet, G. Oszlànyi, L. Forró, P. W. Stephens, M. Tegze, G. Faigel, and A. Jánossy, *Phys. Rev. Lett.*, 1994, **72**(17), 2721–2724.

[110] P. W. Stephens, G. Bortel, G. Faigel, M. Tegze, A. Jánossy, S. Pekker, G. Oszlànyi, and L. Forró, *Nature*, 1994, **370**(6491), 636–639.

[111] K. F. Thier, G. Zimmer, M. Mehring, and F. Rachdi, *Phys. Rev. B*, 1996, **53**(2), R496–R499.

[112] T. M. de Swiet, J. L. Yarger, T. Wagberg, J. Hone, B. J. Gross, M. Tomaselli, J. J. Titman, A. Zettl, and M. Mehring, *Phys. Rev. Lett.*, 2000, **84**(4), 717–720.

[113] F. Bommeli, L. Degiorgi, P. Wachter, Ö. Legeza, A. Jánossy, G. Oszlànyi, O. Chauvet, and L. Forró, *Phys. Rev. B*, 1995, **51**(20), 14794–14797.

[114] S. C. Erwin, G. V. Krishna, and E. J. Mele, *Phys. Rev. B*, 1995, **51**(11), 7345–7348.

[115] G. Grasso, T. M. de Swiet, and J. J. Titman, *J. Phys. Chem. B*, 2002, **106**(34), 8676–8680.

[116] S. Cadars, A. Lesage, and L. Emsley, *J. Am. Chem. Soc.*, 2005, **127**(12), 4466–4476.

[117] S. Cadars, A. Lesage, M. Trierweiler, L. Heux, and L. Emsley, *Phys. Chem. Chem. Phys.*, 2007, **9**(1), 92–103.

Appendix I

```
*****************************************************
**   SAR-COSY in ABX system, hypercomplex detection   **
****** The System ***********************************
spectrometer(MHz)   300.07
spinning_freq(kHz)  *
channels          C13
nuclei            C13 C13 C13
atomic_coords     *
cs_isotropic      177 53 19 ppm
csa_parameters    *
j_coupling        1 2 54
j_coupling        2 3 34
j_coupling        1 3 0
quadrupole        *
dip_switchboard   *
csa_switchboard   *
exchange_nuclei   *
bond_len_nuclei   *
bond_ang_nuclei   *
tors_ang_nuclei   *
groups_nuclei     *
******* Pulse Sequence ******************************
CHN 1
timing(usec)      2.5  (2000)  5.0  (2000)  2.5  (2.5)     (20)256D1  2.5          (2000)  5.0          (2000)  2.5          (3)   2.5       (20)256D2
power(kHz)        100   0      100   0      100  100          0       100            0     100            0     100            0    100            0
phase(deg)          0   0        0   0        0    0          0         0            0       0            0       0            0      0            0
freq_offs(kHz)      0   0        0   0        0    0          0         0            0       0            0       0            0      0            0
phase_cycling       *   *        *   *        *  c:\spinev\i2.pc *   c:\spinev\i3.pc *   c:\spinev\i4.pc * c:\spinev\i4.pc * c:\spinev\i6.pc * c:\spinev\ir.pc(RCV)
******* Variables ***********************************
variable          ppm_ref_offs_1=0
******* Options **************************************
rho0              F1z
observables       F1p
EulerAngles       *
n_gamma           *
line_broaden(Hz)  100 100
zerofill          *
FFT_dimensions    *
options           *

* ppm_ref_offs is the offset, in kHz, of the reference (0 ppm) with respect
  to the reference frequency (0 kHz, at the center of the spectrum)
```